Black Holes and Galaxy Environment in Cosmological Simulations

Stuart I. Muldrew

The University of Nottingham

UNITED KINGDOM · CHINA · MALAYSIA

Thesis submitted to the University of Nottingham
for the degree of Doctor of Philosophy

May 2013

Supervisor: Dr. Frazer R. Pearce

Examiners: Dr. James S. Bolton
University of Nottingham

Prof. Richard G. Bower
University of Durham

Submitted: Thursday 18th April 2013

Examined: Tuesday 21st May 2013

Final version: Tuesday 28th May 2013

Abstract

Understanding the formation and evolution of galaxies is one of the primary research goals of astronomy today. Galaxies are observed to have a range of masses, colours and morphologies, and various processes, including feedback, have been proposed to explain these differences. Some of these processes are related to the environment in which a galaxy resides. In this Thesis I present the results of three projects I have undertaken to help increase our understanding of galaxy formation. The first was to investigate the different methods of structure detection used in simulations. Placing an identical subhalo at different radii inside a larger halo demonstrated that subhalo mass recovery is radially dependent. Subhaloes closer to the centre of a halo are recovered smaller than haloes near the edge, but their peak circular velocity is less affected. The second project set about investigating different ways of measuring galaxy environment. Observationally galaxy environment is most commonly measured through nearest neighbours or fixed apertures, and these have different relationships to the underlying dark matter haloes. Fixed aperture measures are sensitive to halo mass and best probe the 'large-scale environment' external to a halo. Meanwhile nearest neighbour measures are insensitive to halo mass and best probe the 'local environment' internal to a halo. The final project involved implementing the Accretion Disc Particle (ADP) model of black hole growth within a cosmological, large volume simulation, including cooling, star formation and feedback. Comparing this method with a modified Bondi-Hoyle model allows for the investigation of how accretion rates affect feedback and galaxy properties. ADP suffers from the limited resolution of large-scale simulations and produces unphysically large accretion discs. Both models can reproduce the local black hole scaling relations, but produce black hole mass functions that do not agree with observations.

Acknowledgements

The first and most important acknowledgement has to go to Frazer Pearce for his great guidance throughout my time in Nottingham. His door has always been open to me, no matter how stupid the question I might want to ask. My thanks also extends to our research group, past and present, who have seen every plot of this Thesis slowly develop: Hanni Lux, Julian Onions, Thomas Yue, Lyndsay Old, Pascal Elahi, Jamie Bolton and Elena Tundo. I would also like to thank my close collaborators Chris Power, Alexander Knebe, Darren Croton and Ramin Skibba for their assistance and insight throughout this Thesis, as well as all the coauthors of my papers who have supplied me with code or data to make this work possible. I would also like to thank the Virgo and CosmoComp consortiums for giving me the opportunities to travel and present my research.

Working in Nottingham for these last four years has been a very enjoyable experience, even more so because of the very friendly environment. Sharing an office with Sophie Morris, Jamie Ownsworth and Nathan Bourne has created a lively atmosphere, as have my fellow ‘year of 2013’ astronomers Alice Mortlock and Kate Rowlands. I feel I should single out Caterina Lani for a special mention, as she has tolerated my moaning without complaint and been inflicted with far too much proof reading. She is also not afraid to criticise, which is often needed. I am sure there are others who I have missed out, for that I am sorry.

Finally I owe an enormous gratitude to the NHS Diabetes care in Nottingham, Stoke-on-Trent and Burton-on-Trent, without whose swift response and continued care this Thesis would not have been finished.

Published Work

This Thesis is a piece of original reseach performed by myself, unless otherwise stated, with sections having previously been published in the journal *Monthly Notices of the Royal Astronomical Society*. During this Thesis I have led or contributed to the following work:

1. *The Accuracy of Subhalo Detection*
   Muldrew S.I., Pearce F.R., Power C., 2011, MNRAS, 410, 2617

2. *Haloes gone MAD: The Halo-Finder Comparison Project*
   Knebe A., Knollmann S.R., **Muldrew S.I.**, Pearce F.R., Aragon-Calvo M.A., Ascasibar Y., Behroozi P.S., Ceverino D., Colombi S., Diemand J., Dolag K., Falck B.L., Fasel P., Gardner J., Gottlöber S., Hsu C.-H., Iannuzzi F., Klypin A., Lukić Z., Maciejewski M., McBride C., Neyrinck M.C., Planelles S., Potter D., Quilis V., Rasera Y., Read J.I., Ricker P.M., Roy F., Springel V., Stadel J., Stinson G., Sutter P.M., Turchaninov V., Tweed D., Yepes G., Zemp M., 2011, MNRAS, 415, 2293

3. *Measures of Galaxy Environment - I. What is 'Environment'?*
   Muldrew S.I., Croton D.J., Skibba R.A., Pearce F.R., Ann H.B., Baldry I.K., Brough S., Choi Y.-Y., Conselice C.J., Cowan N.B., Gallazzi A., Gray M.E., Grützbauch R., Li I.-H., Park C., Pilipenko S.V., Podgorzec B.J., Robotham A.S.G., Wilman D.J., Yang X., Zhang Y., Zibetti S., 2012, MNRAS, 419, 2670

4. *Subhaloes going Notts: The Subhalo-Finder Comparison Project*
   Onions J., Knebe A., Pearce F.R., **Muldrew S.I.**, Lux H., Knollmann S.R., Ascasibar Y., Behroozi P., Elahi P., Han J., Maciejewski M., Merchán M.E., Neyrinck M., Ruiz A.N., Sgró M.A., Springel V., Tweed D., 2012, MNRAS, 423, 1200

5. *Galaxies going MAD: The Galaxy-Finder Comparison Project*
   Knebe A., Libeskind N.I., Pearce F., Behroozi P., Casado J., Dolag K., Dominguez-Tenreiro R., Elahi P., Lux H., **Muldrew S.I.**, Onions J., 2013, MNRAS, 428, 2039

6. *Measures of Galaxy Environment - II. Rank-Ordered Mark Correlations*
   Skibba R.A., Sheth R.K., Croton D.J., **Muldrew S.I.**, Abbas U., Pearce F.R., Shattow G., 2013, MNRAS, 429, 458

7. *Subhaloes gone Notts: Spin Across Subhaloes and Finders*
   Onions J., Ascasibar Y., Behroozi P., Casado J., Elahi P., Han J., Knebe A., Lux

H., Merchán M.E., **Muldrew S.I.**, Neyrinck M., Old L., Pearce F.R., Potter D., Ruiz A.N., Sgró M.A., Tweed D., Yue T., 2013, MNRAS, 429, 2739

8. *Streams Going Notts: The Tidal Debris Finder Comparison Project*
   Elahi P.J., Han J., Lux H., Ascasibar Y., Behroozi P., Knebe A., **Muldrew S.I.**, Onions J., Pearce F., 2013, MNRAS, accepted (astro-ph/1305.2448)

9. *Measures of Galaxy Environment - III. Difficulties in Identifying Proto-Clusters at* $z = 2$
   Shattow G.M., Croton D.J., Skibba R.A., **Muldrew S.I.**, Pearce F.R., Abbas U., 2013, MNRAS, submitted

10. *Structure Finding in Cosmological Simulations: The State of Affairs*
    Knebe A., Pearce F.R., Lux H., Ascasibar Y., Casado J., Elahi P., Behroozi P., Diemand J., Dolag K., Dominguez-Tenreiro R., Falck B.L., Gottlöber S., Han J., Klypin A., Lukić Z., Maciejewski M., McBride C., Merchán M.E., Corbett-Moran C., **Muldrew S.I.**, Neyrinck M., Onions J., Quilis V., Planelles S., Potter D., Rasera Y., Ricker P.M., Ruiz A.N., Roy F., Sgró M.A., Springel V., Stadel J., Sutter P.M., Tweed D., Zemp M., 2013, MNRAS, submitted (astro-ph/1304.0585)

11. *Modelling the Growth of Supermassive Black Holes in Cosmological Simulations*
    Muldrew S.I., Pearce F.R., Booth C.M., Power C., *In Preparation*

More specifically, Chapter 2 was published in [1], Chapter 3 was published in [3] and Chapter 4 will be published in [11]. Other papers listed here contain follow up work to these projects, to which I have contributed, but has not been presented in this Thesis.

Contents

List of Figures

List of Tables

Black Holes and Galaxy Environment in Cosmological Simulations

Chapter 1

Introduction

Astronomy started as an observational science and still is predominately today. When one mentions astronomy, the first thing people think of is the beautiful Hubble Space Telescope images that give us intricate details of galaxies far away from our own. One of the often forgotten beauties of these galaxies is that their formation and evolution can be fully described using our knowledge of physics and cosmology. It is this great desire to understand these structures that has led to a second methodology in astronomy, that of modelling. The idea of modelling is a simple one; if all structures in the Universe follow the laws of physics then applying these laws should allow us to recreate them. Obviously building a galaxy in the laboratory is an impossible task, but building one on a computer is not and hence the birth of computational cosmology.

Modelling astrophysical problems has come a long way in a comparatively short time. This evolution can be excellently shown by considering two examples for the study of galaxy interactions. Holmberg (1941) investigated the formation of tidal features in interacting galaxies in one of the first modelling papers. He represented a galaxy with 37 light bulbs, with the luminosity of each bulb representing the mass in that part of the body. He then used the measured light to represent the gravitational field and calculated the motion in a timestep. Each bulb was then picked up and placed in its new position by hand. This can be contrasted with Di Matteo, Springel & Hernquist (2005) 64 years later. In the age of supercomputers, they represented each galaxy with 80,000 particles, including dark matter, gas and stars. They simulated the merger of two galaxies using N-body/Smooth Particle Hydrodynamics including radiative cool-

ing, star formation, supernovae feedback and black hole growth and feedback. Today, the size of simulations are ever increasing with the largest, astrophysically useful, N-body simulation being the 'Dark Energy Universe Simulation: Full Universe Run' (DEUS FUR; Alimi *et al.*, 2012) following the evolution of 8192^3 ($\sim 550\,\mathrm{billion}$) dark matter particles in a cube of side length $21\,h^{-1}\mathrm{Gpc}$.

The increasing complexity of these models has allowed us to drastically increase our understanding of galaxy formation. From N-body simulations we have been able to constrain our cosmological model and through hydrodynamics and semi-analytics we understand how galaxies relate to the underlying dark matter field. Although there have been many successes, there are still many unanswered questions. In this Thesis I will focus on addressing three areas of astronomy that require research: structure finding in simulations, measuring galaxy environment and the growth of supermassive black holes.

Running a simulation can be broken down into a three stage process. Firstly, the initial conditions (ICs) are generated for the type of simulation you wish to run. These are then read into a code to evolve them towards the present day. Finally a structure finder is run to extract the haloes and subhaloes from which analysis can be performed. A lot of focus has been placed on comparing how different codes evolve the ICs and some work has also looked at the ICs generation as well (Frenk *et al.*, 1999; Scannapieco *et al.*, 2012; Reed *et al.*, 2013). So far very little work has been performed comparing the results of the structure finding process and this could have important consequences. If the haloes found by one code do not agree with another this could lead to the conclusion that different science is happening in different simulations when in fact the difference is numerical. For example, two halo finders that recover mass differently could produce different mass functions for the same simulation, which would imply different cosmological parameters were used. This could be even further complicatied if the difference in recovery is environment dependent with subhaloes near the centre of haloes being truncated more than subhaloes near the edge. This would have a profound effect on studies of tidal stripping. While these examples are extremes, without a study into structure recovery it cannot be said for sure that all halo finders are finding the same thing. To try and constrain the differences, in this Thesis I take two commonly

used halo finders that use different techniques and apply them to a well constrained set of test cases. This will help answer if there are any differences between the structures recovered and help constrain the differences for future analysis.

A galaxy's environment is known to be correlated with a number of its properties. One of the earliest examples of this was that morphology and environment are linked, with the fraction of early-type galaxies being higher in denser environments (Oemler, 1974; Dressler, 1980). This work has been extended to show that galaxies in dense environments tend to be more massive, brighter, redder and passive, while in less dense environments galaxies tend to have lower mass, are fainter, bluer and star forming (e.g. Norberg *et al.*, 2002; Zehavi *et al.*, 2005; Sheth *et al.*, 2006; Li *et al.*, 2006; Tinker *et al.*, 2008; Ellison *et al.*, 2009; Skibba & Sheth, 2009; Skibba *et al.*, 2009; de la Torre *et al.*, 2011). The effect of environment is often posed as a question of 'nature versus nurture'. This revolves around whether galaxies have undergone rapid evolution by being in dense environments and we are seeing the hastening of internal processes (nature) or are processes only associated with dense environments, such as tidal stripping and increased merger, causing the evolution (nurture). To characterise a galaxy's environment its galaxy density is calculated on some predefined scale. The most common techniques used to calculate the density tend to be either n-th nearest neighbour, where the distance to a fixed nearest neighbour is used, or fixed aperture, where the number of galaxies are counted within a fixed radius. Similar to the structure finding project, having two methods of calculating the same property does not guarantee they are both giving the same result. Depending on scale, different methods might measure different things as fixed apertures tend to smooth the distribution while nearest neighbour is highly adaptive to scale. There is also the question of how each environment measure relates to the underlying dark matter haloes. Disentangling environment in terms of galaxy density and halo mass might give new solutions to the question of 'nature versus nurture'. To investigate the biases in measuring galaxy environment, in this Thesis I apply twenty published environment measures to a well constrained mock galaxy catalogue with the aim of understanding what physical properties each measure corresponds to. This will allow for a better understanding of what is actually being measured by current galaxy environment estimators.

Supermassive black holes reside at the centre of all galaxies with a stellar spheroid (Kormendy & Richstone, 1995; Ferrarese & Merritt, 2000) and their mass shows strong correlations with the galaxies bulge stellar mass and velocity dispersion (e.g. Magorrian *et al.*, 1998; Gebhardt *et al.*, 2000; McLure & Dunlop, 2002; Tremaine *et al.*, 2002; Marleau *et al.*, 2012). It has also been shown that feedback from black holes is essential in shaping the high mass end of the galaxy mass function (Bower *et al.*, 2006; Croton *et al.*, 2006). With so many properties related to the black hole it is essential that they are modelled accurately in simulations in order to produce realistic galaxies. Black hole feedback is the release of energy caused by material accreting onto the black hole. This means that the key to implementing black holes in simulations is the accretion rate. To investigate the growth of black holes in this Thesis I implement the Accretion Disc Particle method (ADP; Power, Nayakshin & King, 2011) and compare it to a modified Bondi-Hoyle model (Booth & Schaye, 2009). The aim is to see how accreting baryonic material onto black holes in different ways affects the accretion rates and in turn the galaxies that form.

In the rest of this Chapter I will begin in Section 1.1 by outlining our current understanding of how structure forms in the Universe. This will be a summary of how a Universe dominated by cold dark matter and a cosmological constant (ΛCDM) produces galaxies and structure, but will also touch on some of the limitations of the theory. I will then outline in Section 1.2 the different methods used to simulate structure formation in general and highlight where they are applied in this Thesis. Finally in Section 1.3 I will give an overview of the different topics in this Thesis and how they are structured.

1.1 Overview of Structure Formation

Galaxy formation is very complex and is the result of a combination of many processes, some of which will be summarised here. A basic outline of our current understanding from Mo, van den Bosch & White (2010) is shown in Figure 1.1. In this Section I aim to only give a brief description relevant to this Thesis and those interested should refer to Mo, van den Bosch & White (2010). A basic summary of Figure 1.1 is that

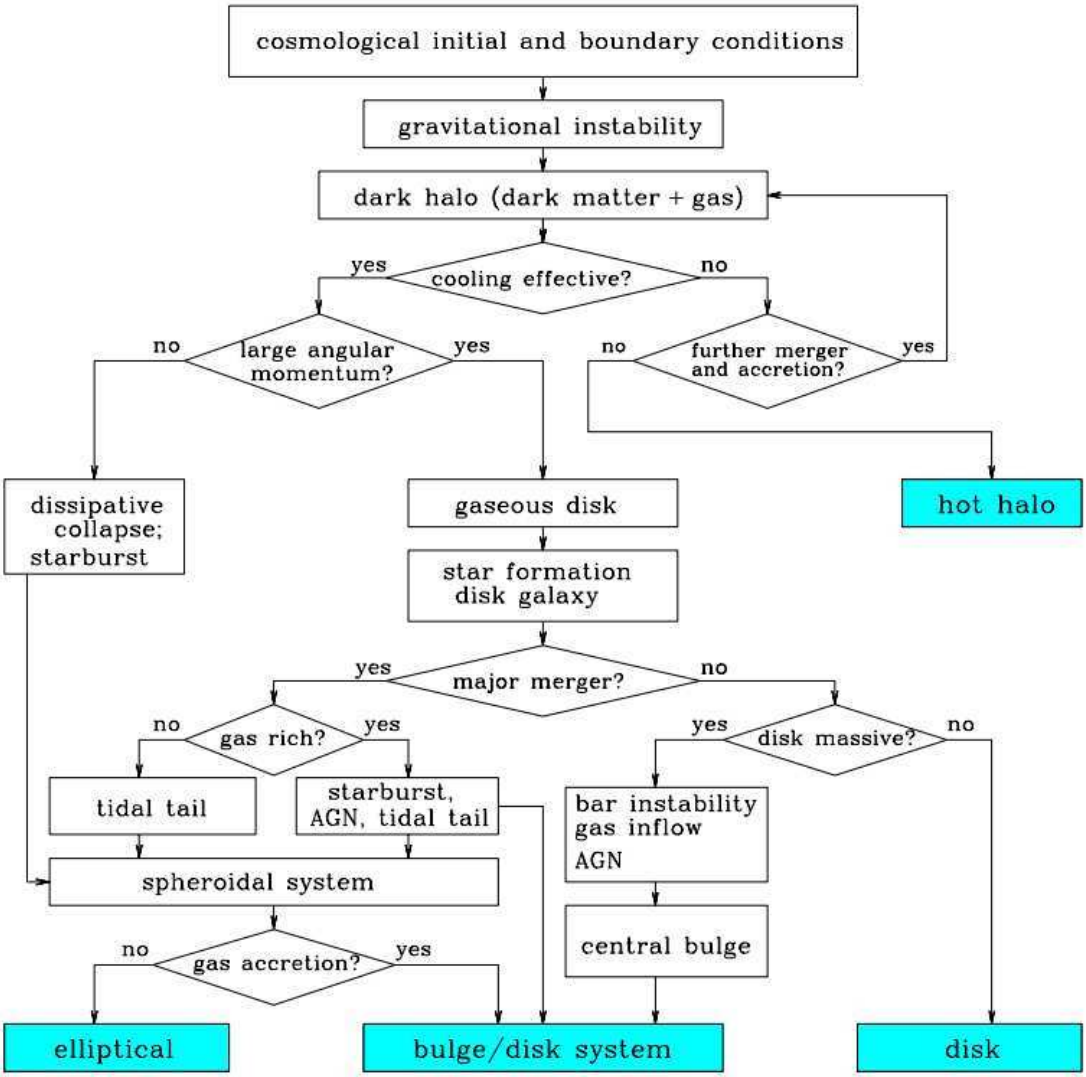

Figure 1.1: A schematic overview of hierarchical galaxy formation from Mo, van den Bosch & White (2010) (see also Cole *et al.*, 2000; Baugh, 2006).

cosmology sets the initial conditions from which dark matter haloes form and trap gas. This gas then cools to form stars and mergers, accretion and feedback dictate the properties of the galaxy that then forms.

Modern Cosmology is built upon two principles, the Cosmological principle and Copernican principle. These state that the Universe is homogeneous, isotropic and that there exists no special observers. Putting this another way, the Universe on large-scales is the same everywhere and in every direction. Hubble (1929) observed that the Universe was expanding and more recently this expansion was observed to be accelerating (Riess *et al.*, 1998; Schmidt *et al.*, 1998; Perlmutter *et al.*, 1999). This expansion can be described by Friedmann's equations:

$$H^2 \equiv \left(\frac{\dot{a}}{a}\right)^2 = \frac{8\pi G}{3}\rho - \frac{kc^2}{a^2} + \frac{\Lambda}{3} \tag{1.1}$$

$$\frac{\ddot{a}}{a} = \frac{4\pi G}{3}(\rho + 3p) + \frac{\Lambda}{3} \tag{1.2}$$

where H is the Hubble constant (which is not constant), a is the expansion factor, G is the gravitational constant, ρ is the density, p the pressure, k the curvature, c the speed of light and Λ is the cosmological constant. Assuming $\Lambda = 0$, there exists a critical density for the Universe, $\rho_{\rm c}$:

$$\rho_{\rm c} = \frac{3H^2}{8\pi G} \tag{1.3}$$

For $\rho < \rho_{\rm c}$ the Universe will be unbound and expand for ever, while for $\rho > \rho_{\rm c}$ the Universe will be bound and eventually collapse back in on itself. It is easier to compare the density to the critical density:

$$\Omega_x = \frac{\rho_x}{\rho_{\rm c}} \tag{1.4}$$

where x represents the different constituents of the Universe such that the overall density is given by:

$$\Omega_0 = \Omega_{\rm m} + \Omega_\gamma + \Omega_\Lambda \tag{1.5}$$

where $\Omega_{\rm m}$ is the matter density, Ω_γ is the radiation density and Ω_Λ is the dark energy density. Dark energy is a poorly understood vacuum energy that drives the acceleration of the expansion of the Universe. In the current epoch $\Omega_\gamma \simeq 0$, but would have been higher at very early times, dominating immediately after the Big Bang.

The matter density can be split into two dominant groups, baryonic and dark matter. The baryonic matter represents all the visible 'ordinary' matter in the Universe. Observational evidence from galaxy clusters suggested this was not the entire mass content. Applying the Virial Theorem to clusters shows that they are much more massive than just the visible component (Zwicky, 1933, 1937). Further evidence for dark matter came from the rotation curves of galaxies which are flat, a result that cannot be explained with the visible matter alone (Rubin & Ford, 1970; Ostriker, Peebles & Yahil, 1974). It was suggested that the dark matter could be either Massive Compact Halo Objects (MACHOs) or Weakly Interacting Massive Particles (WIMPs). MACHOs cannot account for the all the missing mass. WIMPs are the favoured candidate for dark matter, but these particles have yet to be detected. Depending on the mass of the particle, dark matter can be classed as hot, warm or cold. Hot dark matter predicts the largest clusters form first and fragment to form smaller objects, in disagreement with observations, and so has been ruled out (White, Frenk & Davis, 1983). Cold dark matter is the favoured model and reproduces the large-scale structure (Davis *et al.*, 1985; Springel *et al.*, 2005), although recently it has been suggested that warm dark matter would better match the Milky Way satellite population while producing the same large-scale structure (Lovell *et al.*, 2012).

Strong evidence for the hot Big Bang Theory came from the observation of the Cosmic Microwave Background (CMB; Penzias & Wilson, 1965). The CMB is a remnant of the Big Bang and corresponds to the point where the Universe was cool enough for protons and electrons to combine to form neutral hydrogen, known as recombination. The CMB is inhomogeneous and displays small fluctuations in temperature of the order $\sim 10^{-5}\,\mathrm{K}$. Although the Big Bang theory was successful in explaining a number of observables, there were still some things it could not explain alone. The Universe is observed to be flat, $k = 0$ and $\Omega_0 = 1$. This is an unstable solution and any slight deviation would lead to either the Universe collapsing or expanding too fast to form

stars. The smoothness of the CMB is also a problem. For the CMB to be smooth, it must have been in causal contact which is not the case for the Big Bang Theory alone. Finally, Grand Unified Theories (GUT) predict the existence of magnetic monopoles which are not observed. To solve these problems, Guth (1981) proposed Inflation, a period at early times where the Universe expands at an exponential rate due to a quantum scalar field becoming trapped in a false vacuum. This solved the outstanding issues by expanding the Universe fast enough that it used to be in causal contact and diluting the number of magnetic monopoles so they are not observed. It smooths the Universe to keep it flat, and small quantum fluctuations are blown up to become the temperature fluctuations in the CMB.

These small fluctuations become the foundations for the galaxies that form later. As the Universe expands these overdensities collapse, one dimension at a time, forming sheets, filaments and then haloes. The haloes start off with low mass and merge to form larger structures, this is referred to as hierarchical growth. Gas becomes trapped within these haloes and condenses to form stars (White & Rees, 1978). The cosmology outlined here is referred to as cold dark matter with a cosmological constant or ΛCDM. ΛCDM has proven highly successful in explaining the growth of structure in the Universe as shown by Figure 1.2. The predicted power spectrum matches the observed values from Planck Collaboration (2013) to an excellent degree. The latest cosmological parameters needed for ΛCDM simulations are shown in Table 1.1. These have evolved from those measured by Planck's predecessor, the Wilkinson Microwave Anisotropy Probe (WMAP). As the Planck results were only released at the end of this Thesis, and to stay consistent with previous work, older values for these parameters are used in this Thesis. The values adopted for the work in each Chapter are specified there.

As gas is accreted into dark matter haloes, it is shock heated to the virial temperature and must cool to form stars. The time taken to cool is:

$$t_{\rm cool} = \frac{3/2\ nk_{\rm B}T}{\Lambda(n,T,Z,z)} \tag{1.6}$$

where n is the density, $k_{\rm B}$ the Boltzmann constant, T the temperature and $\Lambda(n,T,Z,z)$ is the cooling function. Depending on the value of the cooling time, galaxies will or

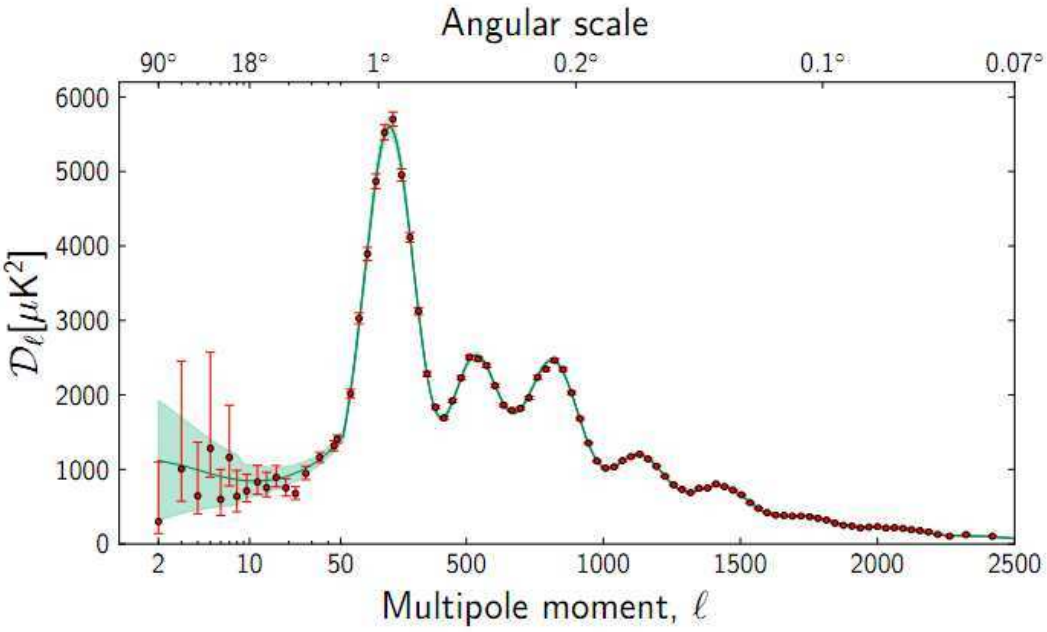

Figure 1.2: The temperature angular power spectrum of the primary CMB from Planck (points) and the prediction from ΛCDM (green line). The shaded region represents cosmic variance. (Figure from Planck Collaboration, 2013). ΛCDM is in excellent agreement with the observed points.

Parameter	Definition	Planck+WP+highL+BAO
$\Omega_{\rm CDM}h^2$	Cold Dark Matter Density	0.1187 ± 0.0017
$\Omega_{\rm b}h^2$	Baryon Density	0.02214 ± 0.00024
Ω_Λ	Dark Energy Density	0.692 ± 0.010
σ_8	RMS Matter Fluctuations on $8\,{\rm Mpc}$ Scales	0.826 ± 0.012
n_s	Scalar Spectrum Power-Law Index	0.9608 ± 0.0054
h	Hubble Parameter	0.6780 ± 0.0077

Table 1.1: The latest cosmological parameter values for ΛCDM from Planck temperature data and lensing, WMAP polarisation at low multipoles, high-ℓ experiments and BAO (Planck Collaboration, 2013).

will not form. For $t_{\rm cool} > t_H$ ($t_H = 1/H$; Hubble time) the gas will not have long enough to cool so will remain hot and galaxies will not form. This is typical for clusters. For $t_{\rm cool} < t_H$ it depends on the dynamical time ($t_{\rm dyn} = 1/\sqrt{G\rho}$) to whether cooling is effective. If $t_{\rm cool} > t_{\rm dyn}$ the gas will cool, but readjust its density distribution quasistatically. Only for $t_{\rm cool} < t_{\rm dyn}$ will the gas cloud fragment which will lead to star formation.

The cooling function, Λ, is dependent on density, n, temperature, T, metallicity, Z, and redshift, z. A typical cooling function, with the contribution from different elements, as a function of temperature is shown in Figure 1.3. Although the cooling function is complex and features contributions from many elements, it can be split into three regimes. For $T > 10^6\,{\rm K}$, cooling is dominated through energy lost by thermal Bremsstrahlung, the process of free electrons scattering off atomic nuclei. Below $10^8\,{\rm K}$ there are also contributions from metals, most notably Iron. At intermediate temperatures, $10^4 < T < 10^6\,{\rm K}$, cooling is dominated by recombination lines and then for low temperatures, $T < 10^4\,{\rm K}$, the cooling function drops away drastically. This is caused by the gas being neutral and so only collisional excitation of molecules dominates cooling.

In numerical simulations, allowing gas to cool in haloes leads to overcooling, causing large amounts of star formation resulting in overly massive galaxies and too many galaxies forming. This is known as the cooling catastrophe. To prevent this, feedback processes warm the gas or ejects it from the system to halt star formation. For low mass galaxies supernova feedback releases energy and is effective in reducing the number of small galaxies (Larson, 1974; White & Rees, 1978; White & Frenk, 1991). For high mass galaxies energy from the active galactic nuclei, powered by black hole accretion, acts to prevent overly massive galaxies forming (Bower *et al.*, 2006; Croton *et al.*, 2006). These feedback processes have been very effective in producing galaxy mass functions in agreement with those observed.

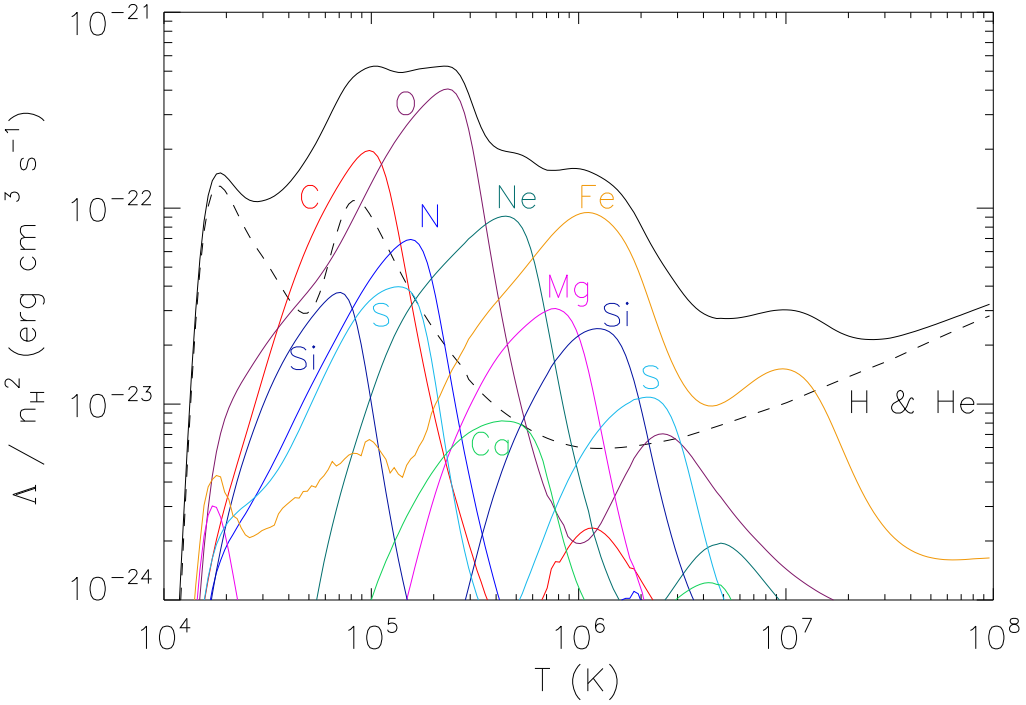

Figure 1.3: Normalised cooling rates as a function of temperature for solar abundances assuming collisional ionisation equilibrium. (Figure from Wiersma, Schaye & Smith, 2009)

1.2 Modelling Structure Formation

On large-scales, linear theory can be used to calculate properties such as the halo mass function. At small-scales however processes are non-linear and so simulations are needed to solve the problem. N-body simulations have been highly successful in predicting the dark matter distribution, but simulating gas and stars is much harder. A variety of techniques exist to put galaxies into simulations, some of which are summarised here.

1.2.1 N-body

Dark matter can be modelled as a collisionless fluid which is discretised into particles. These particles do not represent elementary or particle physics particles but are resolution elements of the field. The only force that then acts on the dark matter is gravity and the potential can be found through Poisson's equation:

$$\nabla^2\phi(\mathbf{x}) = 4\pi G[\rho(\mathbf{x}) - \bar{\rho}] \tag{1.7}$$

The gradient on the potential can then be used to find the acceleration on the particles. There are various ways of determining the gravitational force with the most simple being the Particle-Particle method (PP; Aarseth, 1963; Hénon, 1964). This involves summing the gravitational force over all particles with:

$$\mathbf{F} = \frac{GMm}{(r^2+\epsilon^2)^{3/2}}\mathbf{r} \tag{1.8}$$

where ϵ is the gravitational softening added to prevent $\mathrm{F} \rightarrow \infty$ when $r \rightarrow 0$. PP scales with N^2 making it slow and so is not suitable for large N.

An alternative to PP is the Particle-Mesh method (PM; Efstathiou & Eastwood, 1981; Klypin & Shandarin, 1983). The discrete particle masses are smoothed onto a uniform grid. Equation 1.7 is then solved for the potential on the grid using Fast Fourier Transforms (FFT) and this is used to calculate the force on the particles. This method is much quicker than PP, but is inaccurate on small scales due to the resolution of the grid.

Another method, that doesn't involve using FFT, is the tree method (Barnes & Hut, 1986; Jernigan & Porter, 1989). Particles are arranged in a hierarchy of groups. By calculating the gravitational force using groups this method is quicker than PP. There are various ways of constructing the tree, with the most common being the Barnes-Hut. In this scheme the volume is split up recursively with every cell that contains a particle being split into 8 equally sized smaller volumes. The gravitational force is then calculated by considering the largest node and applying the criterion:

$$r > \frac{l}{\theta} \tag{1.9}$$

where l is the size of the node, θ is the opening angle and r is the distance between the particle under consideration and the node. If the inequality is satisfied then the node is used to calculate the force using Equation 1.8, otherwise it is opened and the criterion is applied to the next level. This method scales as $N\log(N)$ making it quicker than PP, but slower than PM. However it is more accurate at small scales than PM.

Most codes use a hybrid of these methods relying on PM at large-scales for speed and either PP or Trees at small-scales for accuracy. Particle-Particle Particle-Mesh (P^3M) and Tree-PM are the most common of these. The work in this Thesis was conducted using GADGET (Springel, 2005) which is a Tree-PM code. Other methods exist for performing N-body simulations and more details can be found in Hockney & Eastwood (1981) and Dehnen & Read (2011).

1.2.2 Hydrodynamics

One possible way of adding galaxies to N-body simulations is to add the gas at the start of the simulation and follow its evolution, including some subgrid density and temperature requirements for star formation. Star formation is a poorly understood process and often the resolution is not high enough to attempt to simulate it directly. The fluid equations can be derived in two different reference frames, moving with the fluid (Lagrangian) or fixed with respect to the fluid (Eulerian). For simulations using the Lagrangian derivation the fluid is discretised into particles and their properties followed using Smooth Particle Hydrodynamics (SPH). Some commonly used exam-

ples include GADGET (Springel, 2005), HYDRA (Couchman, Thomas & Pearce, 1995) and GASOLINE (Wadsley, Stadel & Quinn, 2004). For the Eulerian formulation, the volume is split up into a grid and the properties are calculated for each cell. Using Adaptive Mesh Refinement (AMR) each cell can be broken down into smaller cells to gain more resolution and increase the speed of the code. Some commonly used examples include RAMSES (Teyssier, 2002), ENZO (O'Shea *et al.*, 2004) and FLASH (Fryxell *et al.*, 2000). A further method is the recently developed Lagrangian hybrid code AREPO (Springel, 2010a). AREPO solves the fluid equations on a moving mesh to take the advantages of both methods. Using a mesh instead of SPH gives better treatment of shocks, while having it move gives Galilean invariance. For the remainder of this section I will focus on SPH, as grid codes are not used in this Thesis. I aim to outline the key concepts of SPH, but for a more detailed description see the review Springel (2010b) or the code paper for GADGET (Springel, 2005), the code used in this Thesis.

SPH works by smoothing out properties amongst the particles. Any field, $F(\mathbf{r})$, can be smoothly interpolated, $F_s(\mathbf{r})$, using a smoothing kernel, $W(r,h)$:

$$F_s(\mathbf{r}) = \int F(\mathbf{r}) W(\mathbf{r}-\mathbf{r}', h) \mathrm{d}\mathbf{r}' \tag{1.10}$$

The smoothing kernel is normalised such that:

$$\int W(\mathbf{r}-\mathbf{r}', h) \mathrm{d}\mathbf{r}' = 1 \tag{1.11}$$

Early work used a Gaussian for the kernel (Gingold & Monaghan, 1977), but currently the most commonly used is a cubic spline kernel:

$$W(r,h) = \frac{8}{\pi} \begin{cases} 1 - 6\left(\frac{r}{2h}\right)^2 + 6\left(\frac{r}{2h}\right)^3 & 0 \leq \frac{r}{2h} \leq \frac{1}{2} \\ 2\left(1 - \frac{r}{2h}\right)^3 & \frac{1}{2} < \frac{r}{2h} \leq 1 \\ 0 & \frac{r}{2h} > 1 \end{cases}, \tag{1.12}$$

where h is the smoothing length defined by the distance to a constant number of neighbouring particles or a constant mass under the kernel. A value of the initial mass of 48 neighbouring particles is often used to maximise the smoothing, but prevent small

scale clumping. Discretising Equation 1.10 gives:

$$F_s(\mathbf{r}) \simeq \sum_j \frac{m_j}{\rho_j} F_j W(\mathbf{r} - \mathbf{r}_j, h) \tag{1.13}$$

from which the density, perhaps the most important quantity, can also be determined:

$$\rho_i = \sum_{j=1}^{N} m_j W(\mathbf{r}_i - \mathbf{r}_j, h_i) \tag{1.14}$$

Starting from the Euler equations in Lagrangian form for an inviscid gas, the equation of motion can be derived as:

$$\frac{\mathrm{d}\mathbf{v}_i}{\mathrm{d}t} = -\sum_{j=1}^{N} m_j \left[f_i \frac{P_i}{\rho_i^2} \nabla_i W_{ij}(h_i) + f_j \frac{P_j}{\rho_j^2} \nabla_i W_{ij}(h_j) \right] \tag{1.15}$$

where,

$$f_i = \left[1 + \frac{h_i}{3\rho_i} \frac{\partial \rho_i}{\partial h_i} \right]^{-1} \tag{1.16}$$

This gives the acceleration of the particles. The change in thermal energy can be calculated by first considering the pressure P:

$$P_i = A_i \rho_i^{\gamma} = (\gamma - 1)\rho_i u_i \tag{1.17}$$

where u is the thermal energy per unit mass and γ is the adiabatic index. This leads to a change in thermal energy of:

$$\frac{\mathrm{d}u_i}{\mathrm{d}t} = f_i \frac{P_i}{\rho_i} \sum_j m_j (\mathbf{v}_i - \mathbf{v}_j) \cdot \nabla W_{ij}(h_i) \tag{1.18}$$

Simulating the gas alone is not sufficient enough to study galaxy formation. Cooling is required to form stars and is therefore added in addition to the above. As discussed in Section 1.1 this leads to overcooling in haloes, so feedback processes need to also be added. Although simulating the gas directly has many advantages, adding many sub-grid models to describe the different processes can lead to varying results in the final

output (Scannapieco *et al.*, 2012). Furthermore, the resulting model is computationally expensive and so attempts have been made to come up with more simplified methods of adding galaxies to dark matter simulations.

1.2.3 Semi-Analytics

Perhaps the most commonly used method of adding galaxies to N-body simulations is the semi-analytic approach. Using the outline of galaxy formation from White & Rees (1978), White & Frenk (1991) proposed the first semi-analytic model. Today there are many different implementations built with an increasing number of physical processes (e.g. Cole *et al.*, 2000; Bower *et al.*, 2006; Croton *et al.*, 2006; De Lucia & Blaizot, 2007; Font *et al.*, 2008; Guo *et al.*, 2011). The foundation of the semi-analytic approach is the merger tree from a N-body simulation. This determines the history of the $z = 0$ dark matter haloes, with branches representing the progenitors that built that halo. Starting from halo masses and gas cooling, cause and effect are then related to each other through a series of equations. These equations are formulated as proportionality relations between variables and are equated through a series of free parameters. The free parameters are then fitted by constraining the model to reproduce certain $z = 0$ properties, such as the luminosity function and clustering (see Bower *et al.*, 2010, for more details on fitting parameters). The result of this is that a full galaxy catalogue, containing an array of different properties, is produced across all redshifts. This is very useful for studying how galaxies evolve.

One of the main criticisms of semi-analytic models is the large number of free parameters required to reproduce observables. This viewpoint is excellently summarised in the review by Baugh (2006), stating that "some in the community have clearly taken to imply some half-baked witches' brew of ingredients, from which any result can be coaxed with a suitable incantation." Although there are many free parameters, this is an unfair criticism. There are many poorly understood processes that go into galaxy formation and the number of parameters is a consequence of that. All the parameters have physical meaning, often relating efficiencies of processes, we just need to further understand the process to understand the parameter. The great advantage of semi-analytics is the power to test cause and effect. By introducing a new model or

changing the efficiency of a process gives an immediate indication of what effect it will have on the galaxy population and properties. Semi-analytic models are also very quick to run giving a solution much faster than their hydrodynamic counterparts. No semi-analytic modelling was used in this Thesis, but some of the environment measures in Chapter 3 were tested on the Bower *et al.* (2006) model, although that has not been included.

1.2.4 Halo Occupation Distribution

The Halo Occupation Distribution (HOD) is a statistical method for adding galaxies to the haloes of dark matter N-body simulations. The model is built for a single redshift and is constrained to match the luminosity function and clustering. Using the masses of the dark matter haloes, a statistical relation gives the number of galaxies above a certain magnitude that would be expected to be found in that halo. This number of galaxies is then added following the density of the halo and luminosities are assigned to reproduce the observed luminosity function. Various HOD models constrained to fit different magnitude limits and bands exist (e.g. Jing, Mo & Boerner, 1998; Benson *et al.*, 2000; Berlind & Weinberg, 2002; Zehavi *et al.*, 2005; Skibba & Sheth, 2009). While HOD models give better matches than semi-analytics to the observations, their main disadvantage is that they give no information on the evolution of the galaxies or why they have those properties. HOD modelling was used in Chapter 3 of this Thesis and a description of the Skibba & Sheth (2009) model can be found in Section 3.2.2.

1.2.5 Subhalo Abundance Matching

Subhalo Abundance Matching (SHAM) has become an increasingly popular method of adding galaxies to dark matter N-body simulations due to the increased resolution allowing subhaloes to be found (e.g. Vale & Ostriker, 2004; Conroy, Wechsler & Kravtsov, 2006; Guo *et al.*, 2010; Guo & White, 2013). SHAM works by finding the subhaloes within a halo and assuming a monotonic relationship between the stellar mass of galaxies and the maximum mass attained by a subhalo in its lifetime. Galaxies are then added to the subhaloes, constrained by the observed luminosity function, with

the minimum galaxy luminosity being related to the smallest subhalo detected. Like HOD modelling the main disadvantage of these models is that they give no evolution information as they are built at a single redshift, although use subhalo properties from higher redshifts. In addition, it is not clear that the basic assumption of a monotonic relationship is accurate (Guo & White, 2013). SHAM modelling is not used in this Thesis.

1.3 Thesis Structure

This Thesis is structured around three projects:

- **The Accuracy of Subhalo Detection**: Before investigating physical processes in simulations it is essential to understand how structure is recovered. In Chapter 2 I present a study investigating the differences between subhaloes found using SUBFIND and AHF.

- **Measures of Galaxy Environment**: A galaxy's environment is known to affect its properties. Many different methods are used to recover environment, or galaxy density, and it is not immediately apparent if they all recover the same property. In Chapter 3 I apply twenty published environment measures to a well constrained mock galaxy catalogue to investigate the variation in the methods of measuring environment.

- **Growth of Supermassive Black Holes:** Supermassive black holes are present in all galaxies with a stellar bulge and through feedback play an important role in shaping the high mass end of the galaxy mass function. In Chapter 4 I implement the accretion disc particle method of black hole growth in a large cosmological volume simulation including cooling, star formation and feedback and compare it with a modified Bondi-Hoyle model. This allows for the investigation of how accretion rates onto the black hole effects the growth and galaxy properties.

Finally in Chapter 5 I bring together the summary and conclusions of this Thesis and how they relate to galaxy formation and evolution in general.

Chapter 2

The Accuracy of Subhalo Detection

With the ever increasing resolution of N-body simulations, accurate subhalo detection is becoming essential in the study of the formation of structure, the production of merger trees and the seeding of semi-analytic models. To investigate the state of halo finders, in this Chapter we compare two different approaches to detecting subhaloes; the first based on overdensities in a halo and the second being adaptive mesh refinement. A set of stable mock NFW dark matter haloes were produced and a subhalo was placed at different radii within a larger halo. SUBFIND (a Friends-of-Friends plus overdensity based finder) and AHF (an adaptive mesh based finder) were employed to recover the subhalo. As expected, we found that the mass of the subhalo recovered by SUBFIND has a strong dependence on the radial position and that neither halo finder can accurately recover the subhalo when it is very near the centre of the halo. This radial dependence is shown to be related to the subhalo being truncated by the background density of the halo and originates due to the subhalo being defined as an overdensity. If the subhalo size is instead determined using the peak of the circular velocity profile, a much more stable value is recovered. The downside to this is that the maximum circular velocity is a poor measure of stripping and is affected by resolution. For future halo finders to recover all the particles in a subhalo, a search of phase space will need to be introduced. The entirety of this Chapter was published in Muldrew, Pearce & Power (2011).

2.1 Introduction

It has long been understood that dark matter plays an essential role in galaxy formation. White & Rees (1978) demonstrated that dark matter haloes act as potential wells within which infalling material can be captured and condense to form galaxies. As the Universe ages, these haloes merge to form larger structures and this continued process produces the framework of the Universe that we see today. This so called hierarchical model of galaxy formation has been put to many tests including those generated by N-body simulation. One of the most widely used of these simulations is the Millennium Simulation (Springel *et al.*, 2005) which accurately reproduced the large-scale structure of a $500\,h^{-1}\mathrm{Mpc}$ cube region of the Universe.

One of the challenges of studying the results of N-body simulations has been finding a consistent way of identifying the structures and substructures within them. Detailed studies of haloes and subhaloes require halo finders, codes that scan the simulation outputs and identify structures. Many different halo finders are available and each uses different techniques and definitions of the haloes they find. Broadly, halo finders fall into two general categories; those based on the Friends-of-Friends (FoF) technique and those based on grids.

FoF was first proposed by Davis *et al.* (1985) and locates haloes based on a predetermined linking length for particles. This is usually a fraction of the mean inter-particle separation and any two particles closer than this distance are linked together. Isolated sets of linked particles are then identified as the haloes. Commonly a value of 0.2 times the mean inter-particle separation is chosen motivated by Standard Cold Dark Matter (SCDM; $\Omega_0 = 1.0$ & $\Omega_\Lambda = 0.0$) (Davis *et al.*, 1985) and a slightly lower value of 0.16 is sometimes adopted for Λ-Cold Dark Matter (ΛCDM; $\Omega_0 = 0.3$ & $\Omega_\Lambda = 0.7$) (Lacey & Cole, 1993; Eke, Cole & Frenk, 1996). Despite the difference, convergence between cosmologies in the halo mass function can be found using 0.2 (see Jenkins *et al.*, 2001) making this the most widely used. The FoF method was implemented in, for example, SUBFIND (Springel *et al.*, 2001) and HFOF (Klypin *et al.*, 1999), with different techniques being used to find subhaloes. HFOF uses hierarchical FoF to locate the subhaloes by using a shorter linking length inside the halo, while SUBFIND searches the haloes for overdensities in the density profile.

The grids method of halo finding works by placing a grid across the simulation and smoothing the discrete particle data onto that grid and then locating the densest cells. Refinement can be built onto the grid to obtain improved resolution and to increase the speed of the code. The density peaks that are located on the grid can then be used as the seeds for potential structures. This technique was used by, for example, AHF (Knollmann & Knebe, 2009) and ASOHF (Planelles & Quilis, 2010). The variations between these codes comes in the definition of haloes. AHF uses isodensity contours on the grid, while ASOHF uses spherical overdensities.

FoF and grid based methods are the two main ways for locating structure, but there are alternatives. More recent finders, such as HSF (Maciejewski *et al.*, 2009), have tried using phase space to identify subhaloes. This extends the search based on position and density to incorporate the velocity of the particles. Bulk velocities can then also be used to help identify structures. Other finders that have tried different techniques include VOBOZ (Neyrinck, Gnedin & Hamilton, 2005), which replaced the uniform grid with a Voronoi diagram, and SURV (Tormen, Moscardini & Yoshida, 2004; Giocoli *et al.*, 2010), which uses knowledge of the structures from one snapshot to help find structure in the next. While this summary of halo finders is by no means exhaustive, it does give a flavour for the different techniques employed. A thorough review of the different types of halo finders available and their effectiveness can be found in Knebe *et al.* (2011).

The importance of accurate subhalo detection has increased in recent years with the advances in high resolution simulations. Various simulations of Milky Way sized haloes have been produced including via Lactea (Diemand, Kuhlen & Madau, 2007; Diemand *et al.*, 2008), Aquarius (Springel *et al.*, 2008) and GHALO (Stadel *et al.*, 2009). As expected, these haloes contain a wealth of substructure (see Gao *et al.*, 2004). However, it is important to ask how robust the recovered properties of subhaloes are to the choice of subhalo finder. For example, subhaloes are identified initially as overdensities in their host haloes. We expect picking out such overdensities to be more difficult in the innermost parts of the host haloes where the background density is the greatest. If one halo finder is less able to pick out these overdensities than another halo finder, we would expect this halo finder to systematically underpredict the numbers of subhaloes

in the inner parts of haloes, which would have important implications for how we interpret the results of, for example, the radial distribution of subhaloes and subhalo mass loss.

In this Chapter we set out to quantify the extent to which our choice of halo finder impacts on the radial distribution of subhaloes that we recover. Specifically we focus on SUBFIND (Springel *et al.*, 2001) and AHF (Knollmann & Knebe, 2009) and ask how well these halo finders can recover the properties of a NFW subhalo (Navarro, Frenk & White, 1996, 1997) embedded in a more massive host NFW halo. The advantage of this approach is that, unlike using haloes and subhaloes drawn from cosmological simulations, we know exactly which particles belong to the host and to the subhalo at initial time and we can track their positions and velocities at all subsequent times. This provides a clean test of the halo finders because any discrepancies found can be identified easily.

The rest of this Chapter is setout as follows. In Section 2.2 we outline the methods used, including summaries of the halo finders and the process of constructing a mock 6D (x, y, z, v_x, v_y, v_z) NFW halo by reproducing the density and velocity profiles. We then use this construction, in Section 2.3, to model an infalling subhalo. This is undertaken in two ways, first by considering how well the halo finders recover the subhalo when simply placed at different radii within the main halo. The second method is to let the subhalo fall into the main halo under gravity and compare how the different halo finders recover the subhalo. Having established the accuracy of the halo finders, in Section 2.4 we investigate the effect the trajectory of the subhalo has on stripping as it passes through the halo. In Section 2.5 we test the reliability of recovering the peak in the circular velocity profile. Finally we summarise our results. Throughout this Chapter, a standard Λ-Cold Dark Matter (ΛCDM) cosmology has been adopted, taking $\Omega_0 = 0.3$, $\Omega_\Lambda = 0.7$ and $h = 0.73$, where appropriate, consistent with observations from the Wilkinson Microwave Anisotropy Probe first year results (WMAP; Spergel *et al.*, 2003).

2.2 Methods

2.2.1 Halo Finders

For the purpose of this Chapter we focus on two halo finders that rely on different methods to detect haloes and subhaloes.

2.2.1.1 AHF

AHF[1](Knollmann & Knebe, 2009) is an updated version of MHF (Gill, Knebe & Gibson, 2004) and works using an adaptive mesh refinement method. It begins by placing a user-defined grid across the box and calculates the particle density in each cell. If this is greater than a user-specified value, then the cell is refined with a smaller grid. The particle density is then recalculated on this finer grid and, if required, further refinement is carried out. Once all the refinements are carried out, a hierarchical grid tree of the density distribution has been produced and this can be used to find structure. Throughout this Chapter, we used a grid of 128 cells with refinement being carried out in cells that contain more than 3 particles.

The most refined and isolated cells are used as potential halo centres and these are linked to the coarser grids to build the structure. If two isolated centres join up on a coarser grid then these are combined into one structure. By considering these separate, isolated points in one structure, substructure can be defined. Once the structures are identified, starting on the lowest level of substructure, they are tested for boundness in isolation. This is conducted by comparing the particles velocity to the local escape velocity obtained using a spherical potential approximation. If a particle is found to be unbound it is assigned to the next highest level of structure until it is dispensed with if not bound to the halo. The haloes are then truncated at the virial radius (see Section 2.2.2) to define their size. For the subhaloes, not all have a low enough overdensity to satisfy the virial radius due to the background density of the halo. If this is the case then they are truncated by a sharp spherical boundary at the outer radius at which their density profile first shows an upturn and starts to rise with increasing distance.

[1]Available from http://popia.ft.uam.es/AMIGA

2.2.1.2 SUBFIND

SUBFIND (Springel *et al.*, 2001) begins by conducting a standard Friends-of-Friends (FoF) search of the simulation volume to identify haloes. At each particle the local density is then calculated using a local SPH-like smoothing kernel interpolation over the nearest neighbours. Any locally overdense region is then considered as a subhalo candidate with its shape being defined by an isodensity contour that traverses the saddle point in the density profile of the halo. This is found by lowering the global density threshold and selecting out the overdense regions. At this stage particles can be members of more than one structure allowing different levels of substructure to be determined. For this Chapter, we used a FoF linking length of 0.2 and 10 particles for the SPH density calculation allowing SUBFIND to recover all subhaloes with 10 or more particles. Tests were also carried out using higher values for the SPH density calculation, but the number of particles recovered was found to be relatively insensitive to this parameter for the size of the subhalo we used.

Once subhalo candidates have been identified, an unbinding procedure is used to determine iteratively which particles are not gravitationally bound. This is achieved by defining the centre of the subhalo as the position of the most bound particle and the bulk velocity as the mean velocity of the particles in the group. The kinetic and potential energies of the particles are then compared and unbound particles are removed. The gravitational potential energy is obtained using a tree algorithm. The final step is to assign particles that are listed in multiple structures to just one. To solve this, the particles are assigned to the smallest structure they are found in. The remaining FoF particles that have not been assigned to substructure are then tested for boundness and assigned to the background halo. Any particles that are not bound to anything are then classified as FoF 'fuzz'.

2.2.2 Constructing a Mock Halo

The following outlines the process of constructing a mock dark matter halo. For simplicity we have limited ourselves to the case of a spherical halo that follows a radial NFW density profile,

$$\rho(r) = \frac{\rho_{\rm crit}\delta_{\rm c}}{r/r_{\rm s}(1+r/r_{\rm s})^2}, \tag{2.1}$$

where $\rho_{\rm crit}$ is the critical density of the universe, $r_{\rm s}$ is the scale radius and $\delta_{\rm c}$ is the characteristic density. Dark matter haloes are characterised by their virial mass,

$$M_{\rm vir} = \frac{4\pi}{3} r_{\rm vir}^3 \Delta_{\rm vir} \rho_{\rm crit}, \tag{2.2}$$

where $r_{\rm vir}$ is the virial radius and $\Delta_{\rm vir}$ is the virial approximation given by Bryan & Norman (1998) as,

$$\Delta_{\rm vir} = 18\pi^2 + 82(\Omega(z) - 1) - 39(\Omega(z) - 1)^2, \tag{2.3}$$

where,

$$\Omega(z) = \frac{\Omega_0(1+z)^3}{\Omega_0(1+z)^3 + \Omega_\Lambda}. \tag{2.4}$$

For $\Omega_0 = 0.3$, $\Omega_\Lambda = 0.7$ and $z = 0.0$, $\Delta_{\rm vir} \approx 101$. Using the scale radius and the virial approximation, the characteristic density is given by,

$$\delta_{\rm c} = \frac{\Delta_{\rm vir}}{3} \frac{c^3}{\ln(1+c) - c/(1+c)}, \tag{2.5}$$

where $c = r_{\rm vir}/r_{\rm s}$ is the concentration.

Using these conditions, a Monte Carlo realisation can be constructed by defining the number of particles within $r_{\rm vir}$, $N_{\rm vir}$, and specifying the concentration of the halo required. The Monte Carlo realisation is produced by drawing a random enclosed mass and inverting to find a radius. This is then turned into a set of coordinates by specifying they produce a smooth distribution on the surface of a sphere. The mass of a NFW halo continues to increase with increasing radius and so in principle has infinite mass; we circumvent this by truncating the halo beyond a cut-off radius, $r_{\rm cut}$. This modifies the density profile so that $\rho(r < r_{\rm cut})$ follows the NFW profile and $\rho(r > r_{\rm cut}) = 0$. For this work we set $r_{\rm cut} = 2\,r_{\rm vir}$. A smoother truncation could be produced by using a exponential decay at the edge of the halo.

Once the halo is constructed, each particle needs to be given a velocity that reproduces the velocity dispersion, $\sigma(\mathrm{r})$, of a halo. Dark matter haloes are supported by the random motion of the particles and to get an accurate representation we need to reproduce this in the velocity of the particles. The velocity dispersion can be obtained by considering the Jeans equation,

$$\frac{1}{\rho}\frac{d}{dr}(\rho\sigma_{\mathrm{r}}^2) + 2\beta\frac{\sigma_{\mathrm{r}}^2}{r} = -\frac{d\Phi}{dr}, \tag{2.6}$$

where $\beta = 1 - \sigma_\theta^2(r)/\sigma_{\mathrm{r}}^2(r)$ and Φ is the gravitational potential. Assuming isotropy, $\sigma_\theta(r) = \sigma_{\mathrm{r}}(r)$, $\beta = 0$ and the velocity dispersion is given by,

$$\sigma_{\mathrm{r}}^2(r) = \frac{1}{\rho(r)}\int_r^\infty \rho(r')\frac{d\Phi}{dr'}dr'. \tag{2.7}$$

This integral was solved by Łokas & Mamon (2001), and confirmed here, to give,

$$\begin{aligned}\frac{\sigma_{\mathrm{r}}^2}{V_{\mathrm{vir}}^2} &= \frac{c^2 s(1+cs)^2}{2[\ln(1+c) - c/(1+c)]}\left[\pi^2 - \ln(cs) - \frac{1}{cs}\right.\\ &\quad - \frac{1}{(1+cs)^2} - \frac{6}{1+cs} + \left(1 + \frac{1}{c^2s^2} - \frac{4}{cs} - \frac{2}{1+cs}\right)\\ &\quad \left.\times \ln(1+cs) + 3\ln^2(1+cs) + 6\,\mathrm{Li}_2(-cs)\right],\end{aligned} \tag{2.8}$$

where $s = r/r_{\mathrm{vir}}$, V_{vir} is the circular velocity at the virial radius and $\mathrm{Li}_2(x)$ is the dilogarithm function given by, [2]

$$\mathrm{Li}_2(x) = \int_x^0 \frac{\ln(1-t)}{t}dt. \tag{2.9}$$

The 3D velocity dispersion is then given by the sum of the individual components. Since isotropy was assumed this gives $\sigma_{\mathrm{3D}}^2(r) = 3\sigma_{\mathrm{r}}^2(r)$. To generate a velocity distribution function for a given radius, a Maxwell-Boltzmann distribution can be assumed (cf. Hernquist, 1993),

$$F(v,r) = 4\pi\left(\frac{1}{2\pi\sigma_r^2}\right)^{3/2} v^2 \exp\left(\frac{-v^2}{2\sigma_r^2}\right). \tag{2.10}$$

[2]Note that the dilogarithm approximation given in Equation (17) of Łokas & Mamon (2001) is not accurate enough for this task.

The function $F(v, r)$ is normalised such that,

$$\int_0^\infty F(v, r)dv = 1. \tag{2.11}$$

The velocity of each particle can then be obtained using the probability distribution of Equation 2.10. Having obtained the density and velocity profiles of the halo, the only thing left is to assign a direction to each velocity. This is done by simply requiring that the directional velocity vectors produce a smooth distribution on the surface of a unit sphere.

To test the stability of this setup, an isolated halo with $M_{\rm vir} = 10^{14}\,{\rm M}_\odot$, $N_{\rm vir} = 10^6$ and $c = 5$ was left to evolve over $8\,{\rm Gyr}$ using GADGET-2 (Springel, 2005). The spline gravitational softening was set to $\epsilon = 3\,{\rm kpc}$ corresponding roughly to the radius of the 100th particle (see Power *et al.*, 2003). Figure 2.1 shows that the halo retains the overall shape of an NFW profile, except at the centre where the profile has flattened similar to that observed by Kazantzidis, Magorrian & Moore (2004). This flattening of the density profile is caused by approximating the distribution function with a Maxwell-Boltzmann. As demonstrated in Kazantzidis, Magorrian & Moore (2004), this will lead to an over estimate of any stripping that occurs. Despite this, it will have no effect on the ability of halo finders to recover the haloes. This was confirmed by using the method outlined in Read *et al.* (2006) to generate haloes with Plummer (1911) and Hernquist (1990) density profiles based on their 6D distribution functions. When the same tests were carried out on these haloes, the same patterns between the halo finders was found as for the NFW with the Maxwell-Boltzmann approximation.

2.3 Modelling an Infalling Subhalo

2.3.1 Static Infall

The first method of modelling the infall of a subhalo we adopted was to consider how well different halo finders recovered the subhalo at a given radius. This was achieved by placing the same sized subhalo *by hand* at different radii within the main halo and attempting to recover it with each halo finder. A halo was generated with $M_{\rm vir} =$

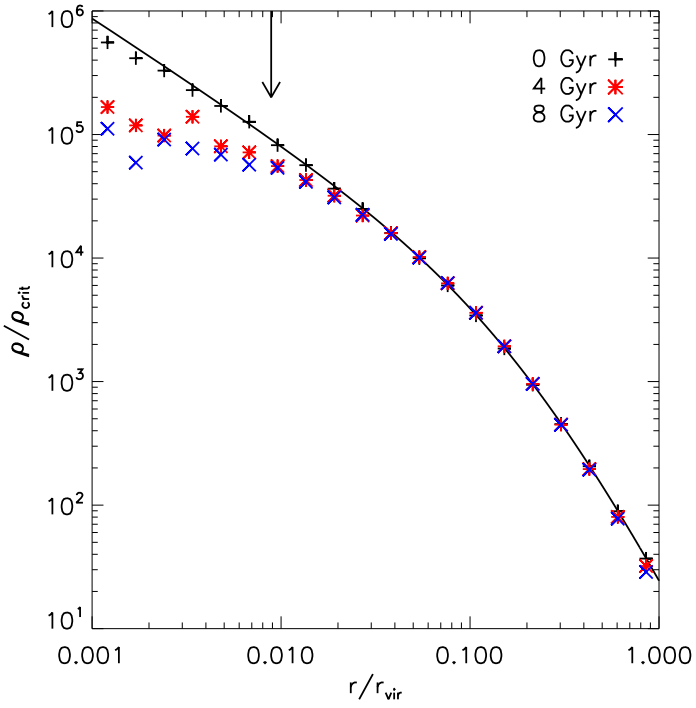

Figure 2.1: The density profile of a $M_{\rm vir} = 10^{14}\,{\rm M}_{\odot}$, $N_{\rm vir} = 10^6$ and $c = 5$ halo left to evolve over $8\,{\rm Gyr}$. The black line denotes the theoretical NFW profile, while the mock halo is shown initially (black pluses), after $4\,{\rm Gyr}$ (red asterisks) and $8\,{\rm Gyr}$ (blue crosses). The arrow represents the Plummer equivalent softening ($h = 2.8\epsilon = 8.4\,{\rm kpc}$).

$10^{14}\,\mathrm{M}_{\odot}$, $N_{\rm vir} = 10^6$ and $c = 5$ and a subhalo with $M_{\rm vir} = 10^{12}\,\mathrm{M}_{\odot}$, $N_{\rm vir} = 10^4$ and $c = 12$. The concentration of the subhalo was set to be higher than the halo in order to reflect the conditions found in cosmological simulations (see Bullock *et al.*, 2001; Eke, Navarro & Steinmetz, 2001). The subhalo was then placed at different distances away from the centre of the halo and given a velocity,

$$v = \sqrt{\frac{2GM_{\rm halo}}{r_{\rm sep}}}, \tag{2.12}$$

where $M_{\rm halo}$ is the mass of the halo and $r_{\rm sep}$ is the separation of the centres of the halo and subhalo, towards the centre of the halo. This velocity corresponds to the conversion of potential energy to kinetic, for two point masses, as the subhalo falls in from infinity. When the subhalo was placed at the centre of the halo, $r_{\rm sep} = 0.0$ so $v \to \infty$. To overcome this, the subhalo was given a velocity of the previous closest separation when it was at the centre of the halo. This set-up was produced 100 times for each separation using different random number seeds. Consistent realisations were found each time.

Figure 2.2 shows the fraction of particles recovered by each halo finder at different separations. Neither halo finder can recover the subhalo when it is near the centre of the halo. This corresponds to the densest region of the halo and leads to any overdensity from the subhalo being hidden. As the separation is increased AHF has a steep rise in the fraction of particles it recovers until it is finding the complete subhalo from $\sim 0.5\,r_{\rm vir}$ outwards. SUBFIND does not have such a drastic change and continues to underestimate the size of subhalo all the way out to $\sim 1.5\,r_{\rm vir}$.

We can gain some insight into the strong radial dependence in recovered particle number in SUBFIND by considering the following simple argument. SUBFIND identifies subhaloes as overdensities; it identifies when a subhalo's local density equals its host halo's local density. This equates to,

$$\frac{\delta_{c_{\rm sub}}}{\frac{r}{r_{s_{\rm sub}}}\left(1+\frac{r}{r_{s_{\rm sub}}}\right)^2} = \frac{\delta_{c_{\rm halo}}}{\frac{r_{\rm sep}-r}{r_{s_{\rm halo}}}\left(1+\frac{r_{\rm sep}-r}{r_{s_{\rm halo}}}\right)^2}, \tag{2.13}$$

where $\delta_{c_{\rm halo}}$ and $\delta_{c_{\rm sub}}$ are the characteristic densities of the halo and subhalo respec-

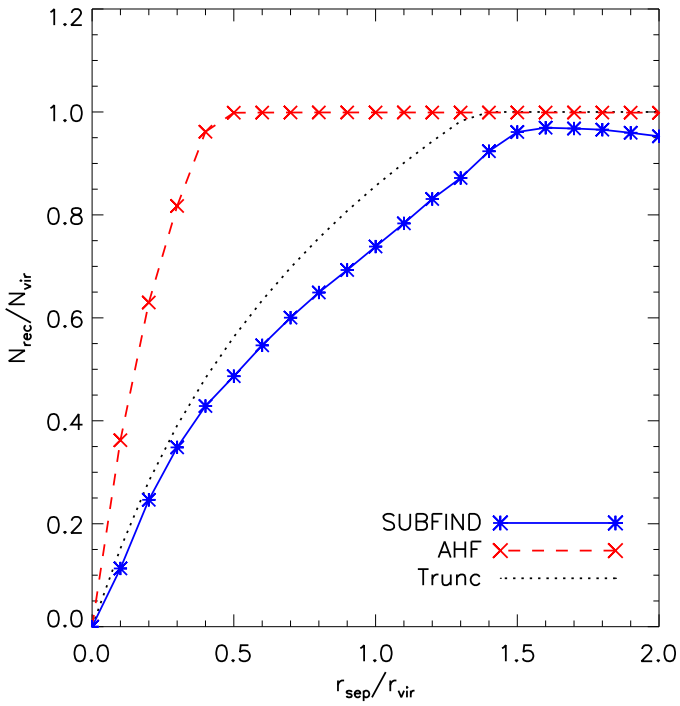

Figure 2.2: The fraction of particles recovered at a given separation as the subhalo is placed at different positions within the halo. Both halo finders recover consistent sizes across the multiple realisations, resulting in small error bars. The dotted line represents the fraction of particles recovered if the subhalo is truncated at the radius where its density is equal to the background density of the halo.

tively (Equation 2.5), $r_{s_{\rm halo}}$ and $r_{s_{\rm sub}}$ are the scale radii of the halo and subhalo respectively, $r_{\rm sep}$ is the separation of the centres of the halo and subhalo and r is the radius of the subhalo at which the densities are equal. The number of particles within r cannot exceed $N_{\rm vir}$ by construction. The shape of the theoretical curve (dotted line in Figure 2.2) implied by Equation 2.13 reasonably captures the shape of the curve recovered by SUBFIND. The agreement is not perfect, Equation 2.13 predicts more mass should be recovered at larger radii than is recovered in practise, but the differences can be easily understood. First, based on the random nature of the velocity assignment some of the particles will have large velocities and will therefore not be bound. The effect of this will be to cause the two curves to deviate systematically from each other with increasing radius. Second, SUBFIND identifies overdensities as saddle points in the mass density profile rather than by equating subhalo and halo mass profiles, as implied by Equation 2.13. Overall the curve shares the same shape as that found using SUBFIND, indicating that the background density is affecting the ability to recover the subhalo.

Implanting a NFW subhalo in a larger halo, defining the virial radius using Equation 2.3, is obviously a highly idealised situation. Realistically the subhalo would be expected to undergo stripping which would cause it to be stripped down to its tidal radius at different points within the halo. This tidal radius would roughly correspond to the radius at which there is a saddle point in the density profile (Tormen, Diaferio & Syer, 1998). This also corresponds to the size of the overdensity that SUBFIND is recovering. Therefore, if the edge of the subhalo is defined as the tidal radius, SUBFIND would give consistent recovery of the subhalo.

A different method of determining the size of the subhalo is to consider the peak in the circular velocity profile (see Ghigna *et al.*, 1998, 2000). This will be less affected by truncation of the subhalo, as the particle with the maximum circular velocity is closer to the centre. Figure 2.3 shows the recovered maximum circular velocity for the subhalo at different separations. This was obtained by calculating the circular velocity for each particle in the subhalo and taking the largest of these as the peak. As expected, both halo finders more accurately recover the subhalo size using this method. SUBFIND still displays a slight radial dependence, with a gradual decrease towards the centre of the halo. This is caused by high velocity particles near the centre of the subhalo being

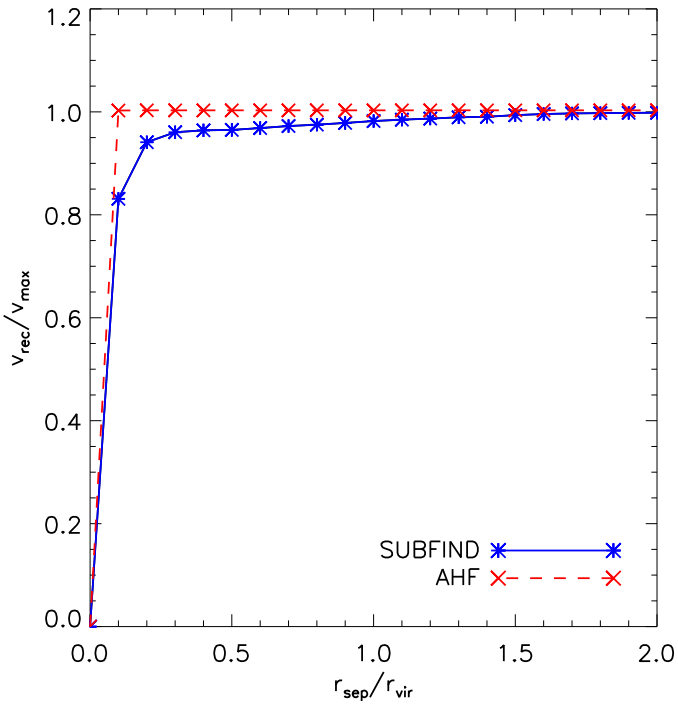

Figure 2.3: The maximum circular velocity of the recovered subhalo as it is placed at different separations. Both halo finders accurately recover the peak, with a small radial dependence displayed in SUBFIND.

unbound due to the truncation. As the subhalo was not detected at the centre of the halo, it is not possible to obtain a circular velocity there.

2.3.2 Dynamic Infall

The second method of investigating the infall of a subhalo was to allow the system to evolve under gravity. The same halo and subhalo properties were set up as in Section 2.3.1. The subhalo was then placed so that $r_{\rm sep} = 3\,r_{\rm vir}$ of the halo and it was given a velocity toward the centre of the halo from Equation 2.12. The subhalo was then left to free-fall through the halo for $6\,\mathrm{Gyr}$ using GADGET-2 with gravitational softening $\epsilon = 3\,\mathrm{kpc}$. Snapshots were taken every $0.05\,\mathrm{Gyr}$. During this run cosmological expansion was turned off so the haloes were only affected by gravity.

Figure 2.4 shows the fraction of particles recovered by SUBFIND and AHF as the subhalo passed through the halo. The subhalo undergoes a large amount of stripping, loosing around 75 percent of its mass. Most of this stripping occurs as the subhalo passes through the very centre of the halo. This corresponds to the greatest rate of change of the potential and so would be expected to have the largest effect. As predicted in Section 2.3.1 both halo finders fail to recover the subhalo as it passes through the centre of the halo and disagree about the size of the subhalo immediately either side of this region. The largest discrepancy occurs when the subhalo is within the virial radius of the halo. As expected due to its definition of a subhalo, SUBFIND recovers a smaller subhalo during the infall phase compared with AHF. After the subhalo has passed the centre of halo, AHF recovers a much larger number of particles due to its unbinding procedure being less efficient and this is discussed further in Section 2.4. As expected, the level of stripping observed is consistent with Hayashi *et al.* (2003) and higher than Kazantzidis, Magorrian & Moore (2004).

2.4 Subhalo Stripping

As seen in Section 2.3.2, an infalling subhalo only undergoes stripping as it passes through the very centre of the halo. This should mean that any subhalo that does not

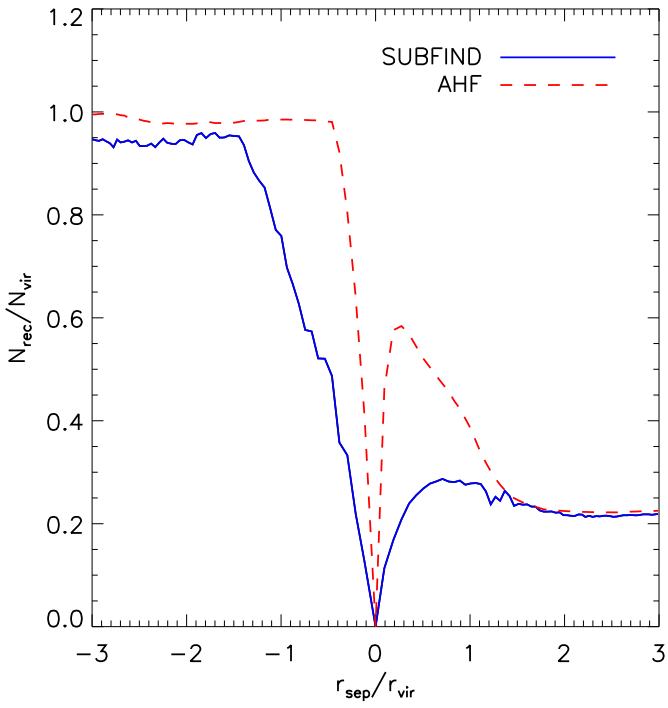

Figure 2.4: The fraction of particles recovered at a given radius as the subhalo is allowed to fall into a halo from infinity. The subhalo experiences the most stripping when it passes through the centre of the halo. Neither halo finder can detect the subhalo as it passes through the centre of the halo and they yield different sizes for the subhalo either side of this region.

pass through the centre of the halo and is merely deflected around it should undergo significantly less stripping. To test this hypothesis, the subhalo was placed at a separation of $3.0\,r_{\rm vir}$ in the x-axis and 0.0, $0.5\,r_{\rm vir}$ and $1.0\,r_{\rm vir}$ in the y-axis. In each case the subhalo was given the same velocity along the x-axis toward the halo as in Section 2.3.2. The subhalo that was on the x-axis followed the same path as the subhalo in Section 2.3.2 passing straight through the halo centre. The other two subhaloes were deflected around the halo centre with closest approaches of $0.2\,r_{\rm vir}$ and $0.5\,r_{\rm vir}$ respectively.

Figure 2.5 shows the fraction of particles recovered by each halo finder for the three scenarios outlined and also the value of the peak in the circular velocity profile. Both halo finders give consistent values for the the final sizes of the subhalo after stripping. For the two subhaloes that do not pass through the centre of the halo, the amount of stripping is noticeably less. The subhalo loses around 35 percent and 50 percent of its mass for closest approaches of $0.5\,r_{\rm vir}$ and $0.2\,r_{\rm vir}$ respectively compared with over 75 percent if it passes through the centre.

Comparing the halo finders as the subhalo passes through the central region of the halo, both show a characteristic dip in the number of particles recovered. It is also noticeable that as the subhalo leaves the centre of the halo, AHF always finds a larger subhalo than SUBFIND. This is also shown very clearly in Figure 2.4 where in the region $0 < r_{\rm sep}/r_{\rm vir} < 1$ AHF gives much higher recovery of particles compared with SUBFIND which has flattened off. The cause of this difference can be seen in the lower left panel of Figure 2.5 by considering the maximum circular velocity. After the subhalo has passed through the centre of the halo, the maximum circular velocity recovered by AHF spikes meaning that background halo particles are being included in the subhalo. There is no such spike in the SUBFIND value (lower right panel). This shows that the unbinding of particles is more efficient in SUBFIND than AHF. This discrepancy is caused by AHF assuming spherical symmetry for the unbinding when the subhalo becomes elongated in the centre of halo and is no longer a spherical shape.

For the subhalo with the closest approach of $0.5\,r_{\rm vir}$, AHF shows a smooth transition in the size of the subhalo, while SUBFIND shows the size to decrease and then increase again. During this transition the subhalo always has a finite size as the subhalo does not

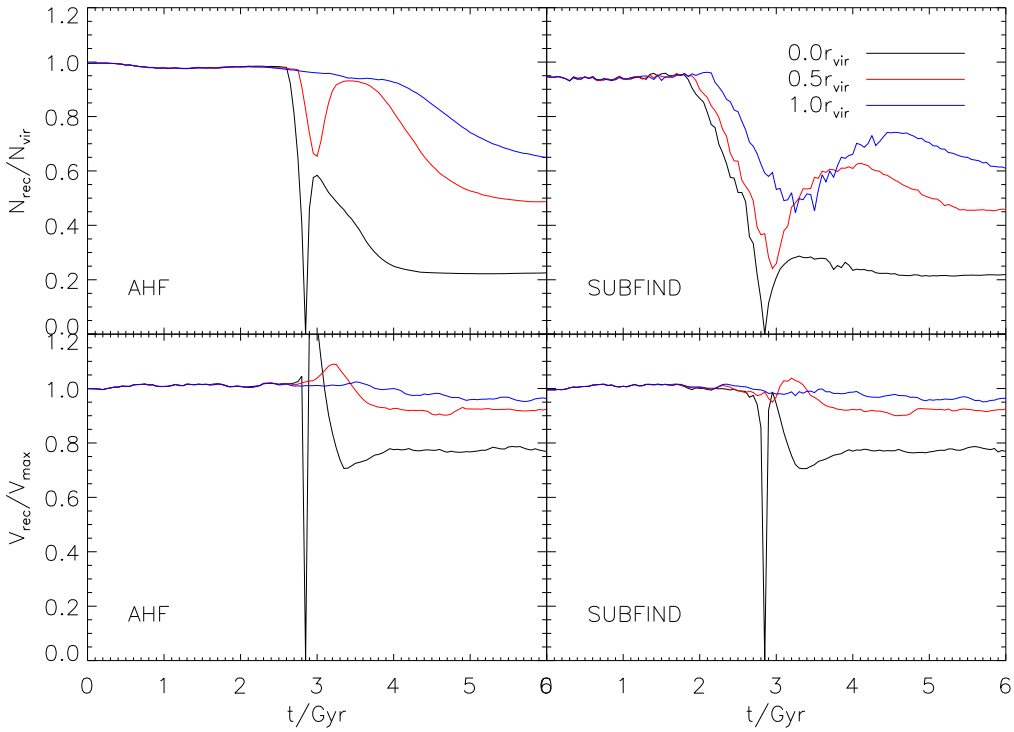

Figure 2.5: Fraction of particles recovered (upper panels) and maximum circular velocity (lower panels) for the subhalo as a function of time as the subhalo falls through the halo. For each case the subhalo is given a velocity along the x-axis toward the halo and starts offset by $3.0\,r_{\rm vir}$ in the x-axis and 0.0 (black line), $0.5\,r_{\rm vir}$ (red line) and $1.0\,r_{\rm vir}$ (blue line) in the y-axis. This corresponds to a closest radial approach to the centre of the halo of 0.0, $0.2\,r_{\rm vir}$ and $0.5\,r_{\rm vir}$ respectively.

pass close enough to the halo centre to completely vanish. The decrease and increase in the size of the subhalo demonstrates that it is being truncated at a radius smaller than its actual size. As the saddle point in the density profile corresponds to the tidal radius (Tormen, Diaferio & Syer, 1998), this in turn shows that a subhalo not passing through the centre of a halo will not be completely stripped down to its tidal radius. This is perhaps not that surprising as the subhalo has not spent a long enough time in the halo to undergo the full effects of tidal stripping.

The maximum circular velocity is shown in Figure 2.5 to be a much more stable quantity compared to particle number as expected from Section 2.3.1. The strong radial dependence of SUBFIND in particle number is not present in maximum circular velocity. While this is an advantage in recovering properties of the subhalo, Figure 2.5 also shows how this quantity can be misleading when considering stripping. For the case where the subhalo passes within $0.5\,r_{\rm vir}$, the subhalo was stripped of around 35 percent of its mass, but the maximum circular velocity changes by less than 5 percent. This is caused by the maximum circular velocity being located at a radius much closer to the centre of the subhalo and so is less affected by stripping which occurs primarily in the outer regions.

2.5 Circular Velocity

As seen in the previous Sections, the peak in the circular velocity profile of a subhalo is a more stable quantity to recover than the total subhalo mass. The origin of this stability is related to the fact that the radius at which the maximum circular velocity is reached is located much closer to the centre of the halo and so is unaffected by truncation. Figure 2.6 shows how the position of peak changes with the concentration of a halo. For a NFW halo this can be obtained numerically to give,

$$\frac{r_{\rm vmax}}{r_{\rm vir}} \simeq \frac{2.16}{c}. \tag{2.14}$$

The values determined by Equation 2.14 are based on an ideal NFW halo, but for low resolution haloes there will be deviations from this curve. For the subhalo used in this work ($c = 12$) $r_{\rm vmax} = 0.18\,r_{\rm vir}$ which corresponds to roughly r_{5000} (the radius at

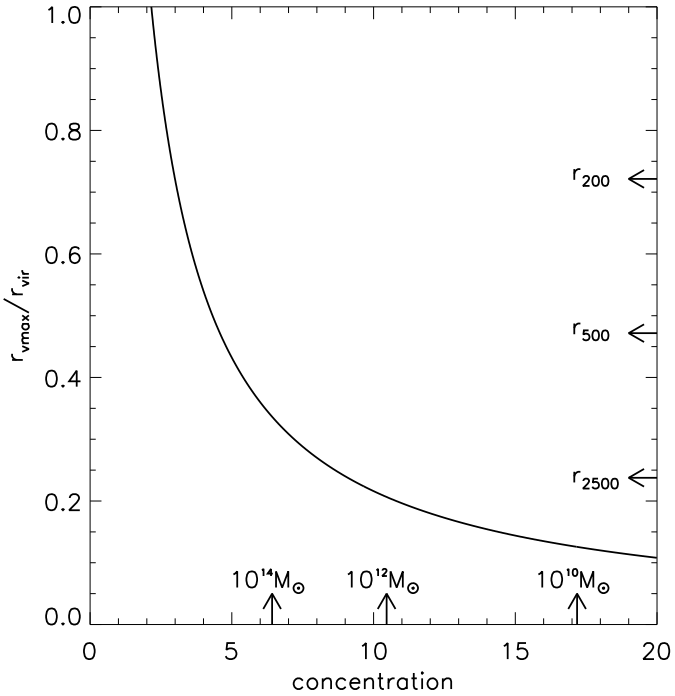

Figure 2.6: The position of the peak of the circular velocity profile in relation to the concentration of a halo. Typical halo concentrations from Neto *et al.* (2007) and radial densities are also labelled.

which the enclosed density is 5,000 times the critical density, $\rho_{\rm crit}$). Stripping occurs in the outer regions of the subhalo and so for it to affect this radius a large amount of material needs to be lost, consistent with Figure 2.5.

One of the main issues with using the maximum circular velocity of a halo is how its measurement depends upon resolution. To investigate this, we generated a halo with $M_{\rm vir} = 10^{12}\,{\rm M}_{\odot}$ and $c = 12$ in isolation using a different number of particles within the virial radius each time. For each number of particles within the virial radius, we constructed 1,000 realisations in order to constrain the variation. Figure 2.7 shows how the recovered maximum circular velocity varied with the total particle number. For the sparsely populated realisations the average maximum circular velocity was higher than the analytic value. As more particles were used, the two values converged. For the average value to be within 2.5 percent of the analytic value, in excess of 500 particles were required in the halo. The variation of the maximum circular velocity between different realisations of the same total virial particle number is strong for the sparsely populated haloes. At all points the curve is within 1 standard deviation of the analytic value, but the variation is clear where for 10 particles the standard deviation is 0.56 compared with 0.002 for 10,000. To obtain an accurate value for the maximum circular velocity of a recovered subhalo, its resolution has to be taken into account.

2.6 Summary and Conclusions

Halo finders are an important tool for the analysis of cosmological simulations. They are pivotal in the construction of merger trees, which underpin galaxy formation modelling, and their results allow us to characterise, for example, the abundance and spatial distribution of both dark matter haloes and subhaloes. There are as many techniques for identifying haloes and subhaloes in cosmological simulations as there are halo finders and so it is interesting to ask whether or not (sub-)halo properties recovered by different halo finders are consistent.

In this Chapter we have compared and contrasted the results of two halo finders, SUBFIND and AHF, that use fundamentally different approaches to identifying subhaloes. We have taken a simple test problem, the identification of a NFW subhalo embedded

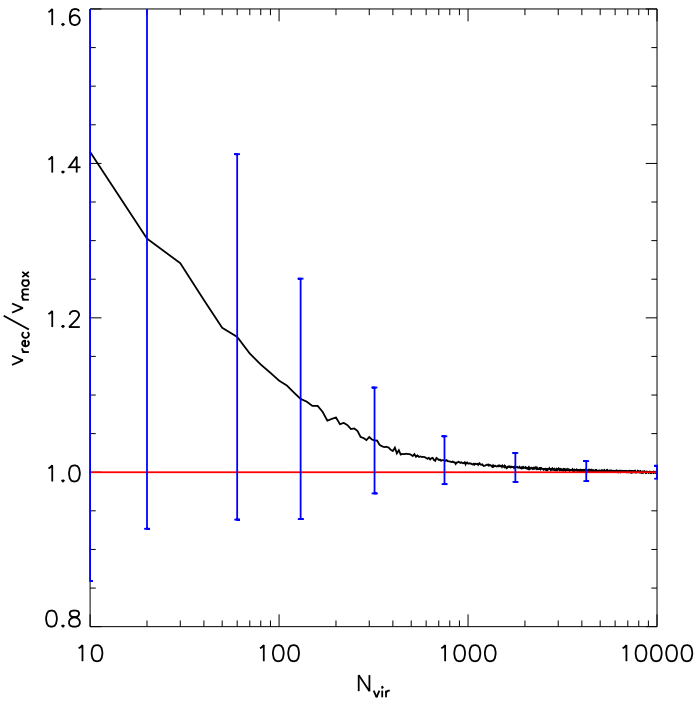

Figure 2.7: The recovered maximum circular velocity compared with number of particles used to generate a $M_{\rm vir} = 10^{12}\,{\rm M}_{\odot}$ and $c = 12$ halo. Error bars represent 1 standard deviation and are distributed symmetrically in log space. For the average to be within 2.5 percent of the maximum value, in excess of 500 particles are required.

in a more massive NFW halo, and compared the performance of SUBFIND and AHF in recovering the mass of the subhalo at different radii within its host. As shown using SUBFIND, halo finders that identify subhaloes as overdensities will have a strong dependence on the local density. This is demonstrated in the strong radial dependence in the fraction of a model subhalo SUBFIND recovers. As the subhalo gets closer to the centre of the halo, the background density from the halo is rising. With a higher background density and the same density for the subhalo, the overdensity will be less leading to a smaller subhalo being recovered. By the time the subhalo is in the centre of the halo, which corresponds to the densest point, the overdensity becomes negligible leading to no saddle point and the subhalo is no longer detected. While the size of the overdensity recovered roughly corresponds to the tidal radius of the subhalo, it has been shown that not all subhaloes are stripped down to this size when they pass through a halo. The authors of SUBFIND are aware of these issues (see Section 4.1 of Springel *et al.*, 2008) and post-process, but where this effect is not taken into account it could have profound consequences on substructure studies.

The radial dependence of locating subhaloes as overdensities will have a large effect on measures of tidal stripping. As a subhalo plunges into a halo, the halo finder will reduce the size of the subhalo due to the increase in density. If this is not considered, then it will appear the subhalo is undergoing a larger amount of stripping as it falls through the halo than it actually underwent. Stripping will be further complicated by the fact it occurs in the outer region of the subhalo, an area that is not included in the truncated subhalo that is recovered. This can lead to confusion when comparing the recovery of AHF and SUBFIND. AHF indicates that most of the stripping occurs as the subhalo passes through the centre of the halo and not during the infall, but AHF has been shown to have inefficient unbinding causing it to retain a larger fraction of particles. Meanwhile SUBFIND indicates a more gradual process, but the effects of truncation will cause the recovered subhaloes to always be lower estimates of the size. Further studies will need to be made to determine how dramatic the effect of stripping is on an infalling subhalo.

The radial dependence in recovery will also have important implications for the subhalo mass distribution. Two subhaloes that have identical mass can be recovered with

different sizes based on position. This will lead to large subhaloes being recovered as smaller ones, in turn, leading to subhalo mass distributions biased towards the low mass end. Whilst most subhaloes that reside in the inner region of the halo will have undergone a large amount of stripping and will be smaller anyway, the effect of truncation still needs to be considered alongside the underlying physics. These issues highlight that the recovered mass identified using the overdensity method is not a good property to consider when studying subhaloes. This is true even as far out as the virial radius of the halo, where the mass can be underestimated by around 25 percent.

A more stable quantity to consider is the peak in the circular velocity profile. This is located much closer to the centre of the subhalo and so will be less affected by truncation and the particular choice of the definition for an entire subhalo. Both AHF and SUBFIND recover consistent values for the maximum circular velocity at all radii within the halo, except at the very centre of the halo where no particles are recovered. This makes the circular velocity peak a useful quantity to track subhaloes and gives a good indication of initial mass. However, when considering stripping, the circular velocity peak is no longer useful. Being located so close to the centre of the subhalo, a substantial amount of the outer layers can be stripped before the peak in the circular velocity is affected.

Two methods of improving the accuracy of subhalo recovery would be halo tracking and phase space. Halo tracking involves identifying the subhalo before it falls into the halo so all the particles that were originally part of the structure are followed and at each time step they can be tested to see if they are still part of the substructure. The disadvantage of this technique is that it requires multiple snapshots to identify the subhalo, not a problem for the second method of phase space. Phase space takes into account not only the spatial position of the subhalo particles, but also links particles based on a common velocity. By considering haloes in phase space density, any subhaloes that are present will stand out as overdensities. These can then be isolated. For subhaloes in the centre of the halo, the difference in the bulk velocity of the particles would cause them to be separated in phase space. The only remaining problem would be if a subhalo was at rest in the centre of the halo. These structures could not be separated in phase space, but it is arguable whether such a structure would be a dynamically

independent entity.

2.7 Further Published Work

The mock haloes described in this Chapter were used in the 'Haloes going MAD', halo finder comparison project (Knebe *et al.*, 2011). This project led onto a subhalo finder comparison project, 'Subhaloes going Notts' (Onions *et al.*, 2012). Using the data from this workshop a number of additional projects were conducted on subhalo spin (Onions *et al.*, 2013), galaxy finding in simulations (Knebe *et al.*, 2013a) and tidal debris finding (Elahi *et al.*, 2013). A full review of halo finders, including results from this Chapter, is presented in Knebe *et al.* (2013b).

Chapter 3

Measuring Galaxy Environment

The influence of a galaxy's environment on its evolution has been studied and compared extensively in the literature, although differing techniques are often used to define environment. Most methods fall into two broad groups: those that use nearest neighbours to probe the underlying density field and those that use fixed apertures. The differences between the two inhibit a clean comparison between analyses and leave open the possibility that, even with the same data, different properties are actually being measured. In this Chapter we apply twenty published environment definitions to a common mock galaxy catalogue constrained to look like the local Universe. We find that nearest neighbour-based measures best probe the internal densities of high-mass haloes, while at low masses the inter-halo separation dominates and acts to smooth out local density variations. The resulting correlation also shows that nearest neighbour galaxy environment is largely independent of dark matter halo mass. Conversely, aperture-based methods that probe super-halo scales accurately identify high-density regions corresponding to high mass haloes. Both methods show how galaxies in dense environments tend to be redder, with the exception of the largest apertures, but these are the strongest at recovering the background dark matter environment. We also warn against using photometric redshifts to define environment in all but the densest regions. When considering environment there are two regimes: the 'local environment' internal to a halo best measured with nearest neighbour and 'large-scale environment' external to a halo best measured with apertures. This leads to the conclusion that there is no universal environment measure and the most suitable method depends on the scale being

probed. The entirety of this Chapter was published in Muldrew *et al.* (2012).

3.1 Introduction

In the paradigm of hierarchical structure formation, the evolution of the primordial density field acting under gravitational instability drives dark matter to cluster and collapse into virialised objects (haloes). Such haloes provide the potential wells into which baryons fall and galaxies subsequently form (White & Rees, 1978). Haloes, galaxies and their environments also interact and merge as structure formation unfolds with time. It therefore follows that the properties of a galaxy should be correlated with the properties of its host halo, and that a galaxy's environment, its host halo's environment, and the dark matter density field are all related in some measurable way.

Such galaxy/halo/dark matter correlations with environment have led to a variety of work examining the environmental dependence of the physics of galaxy formation, both theoretical and observational. Measurements of the galaxy two-point correlation function and halo occupation distribution function (HOD) have shown that more massive, brighter, redder, and passive early-type galaxies tend to be more strongly clustered and hence presumably located in denser environments, while the reverse is true for galaxies that have lower mass, are fainter, bluer and star forming (e.g. Norberg *et al.*, 2002; Zehavi *et al.*, 2005; Sheth *et al.*, 2006; Li *et al.*, 2006; Tinker *et al.*, 2008; Ellison *et al.*, 2009; Skibba & Sheth, 2009; Skibba *et al.*, 2009; de la Torre *et al.*, 2011).

A more direct probe of the influence of environment is the local density field of neighbouring galaxies around each galaxy (defined in various ways). These techniques are better suited to analysing targeted halo and galaxy environment correlations and have proven valuable in the current era of large galaxy survey data sets, where galaxy catalogues can be simultaneously 'sliced' in multiple orthogonal directions to isolate the dependence of specific galaxy properties on environment (e.g. Kauffmann *et al.*, 2004; Blanton *et al.*, 2005; Croton *et al.*, 2005; Cooper *et al.*, 2006; Baldry *et al.*, 2006; Park *et al.*, 2007; Elbaz *et al.*, 2007; Ball, Loveday & Brunner, 2008; Cowan & Ivezić, 2008; O'Mill, Padilla & García Lambas, 2008; Tasca *et al.*, 2009; Ellison *et al.*, 2009).

In undertaking any such analysis the choice of environmental indicator is important

and no one standard has yet emerged. Many of the above cited papers involve disparate selection criteria, research methods and goals, making direct comparisons between them difficult. The definition of environment can vary from two-point clustering and marked clustering statistics, to the number or luminosity density within a fixed spherical or cylindrical aperture, to the measured density enclosed by the n-th nearest neighbour. A further complication is that these methodologies can be performed in either two (projected) or three (redshift space) dimensions. As a consequence, some analyses have yielded irreconcilable results.

All methods that attempt to quantify the environment around a galaxy require some parameter choices. Those that involve a spherical or cylindrical aperture must first choose a fixed smoothing scale within which to measure the local galaxy over- or under-density. On the other hand, when environment measures involve the n-th nearest neighbour, the choice of n instead becomes important. Once n is fixed, this statistic adapts its scale to keep the signal-to-noise constant. But how should one interpret a statistic that combines the physical processes from widely disparate scales across one smoothly varying curve? And how should this be compared with statistics that instead fix the scale along the same curve?

Further complicating comparison are the selection criteria of a dataset itself, its geometry and volume, and the redshift and magnitude uncertainties of the galaxies in it. In short, the measurement of 'environment' used in various studies can be completely different, and environmental correlations should be interpreted and compared with caution. Some environment measures can have advantages and disadvantages for particular research goals. A number of authors have tested and compared a few environment measures (e.g. Cooper *et al.*, 2005; Wolf *et al.*, 2009; Gallazzi *et al.*, 2009; Kovač *et al.*, 2010; Wilman, Zibetti & Budavári, 2010; Haas, Schaye & Jeeson-Daniel, 2012). In general, while the environment measures are correlated, they often exhibit considerable scatter between them.

The primary goal of this Chapter is to compare a variety of published environment measures using a single well constrained data set. For this purpose, we take a dark matter halo catalogue and construct a mock galaxy catalogue designed to have approximately the same global statistical properties as the Sloan Digital Sky Survey (SDSS;

York *et al.*, 2000) main galaxy sample. We then are able to compare the galaxy environment measures to halo mass, dark matter density, and to each other. We also attempt to answer some important questions, such as: Do the different environment methodologies break nicely into different groups that optimally sample the underlying density field in particular ways? Do the statistics of various galaxy properties change dramatically in different environment bins measured in different ways? Can we find a more fundamental definition of environment that is measurable observationally?

This Chapter is organised as follows: In Section 3.2 we outline the mock galaxy catalogue that was generated, constrained by the SDSS, and used to study environment measures. In Section 3.3 we review the range of environment measures available in the literature that are used as part of this study. Having established the method, Section 3.4 explores how the different measures relate to the dark matter halo mass, galaxy colour and large-scale dark matter environment for each galaxy. We also explore how the measures relate to each other for an individual galaxy. Finally in Section 3.5 we discuss and summarise our findings.

3.2 Galaxy and Halo Catalogues

3.2.1 The Millennium Dark Matter Simulation

We begin with the Millennium Simulation (Springel *et al.*, 2005) which is a large N-body simulation of dark matter structure in a cosmological volume. The Millennium Simulation uses the GADGET-2 code (Springel, 2005) to trace the evolution of 10 billion dark matter particles across cosmic time in a cubic box of $500\,h^{-1}\mathrm{Mpc}$ on a side, with a halo mass resolution of $\sim 5 \times 10^{10}\,h^{-1}\mathrm{M}_{\odot}$. It adopts the concordance ΛCDM cosmological parameters, chosen to agree with a combined analysis of the Two-Degree Field Galaxy Redshift Survey (2dFGRS; Colless *et al.*, 2001) and the first-year Wilkinson Microwave Anisotropy Probe data (WMAP; Spergel *et al.*, 2003): $\Omega_0 = 0.25$, $\Omega_\Lambda = 0.75$, $h = 0.73$, $n = 1$, and $\sigma_8 = 0.9$.

The haloes are found by a two-step procedure. First, all collapsed haloes with at least 20 particles are identified using a standard Friends-of-Friends group-finder with

linking parameter $b = 0.2$. Then, post-processing with the substructure algorithm SUBFIND (Springel *et al.*, 2001) subdivides each Friends-of-Friends halo into a set of self-bound subhaloes. We note that comparable halo properties are found using other structure finders (see Chapter 2 and Knebe *et al.*, 2011).

3.2.2 Embedding Galaxies in Haloes

From the Millennium Simulation halo merger tree at $z = 0$, we construct a mock galaxy catalogue using the halo occupation method described in Skibba *et al.* (2006, hereafter S06) and Skibba & Sheth (2009, hereafter SS09); we refer the reader to these papers for details. Other halo-model descriptions of galaxy clustering—conditional luminosity functions (e.g. Yang, Mo & van den Bosch, 2003) and subhalo abundance matching (e.g. Kravtsov *et al.*, 2004)—would produce similar mock catalogues, although an advantage of the SS09 approach is that it includes a strongly constrained model of galaxy colours. S06 describes how the luminosities and real-space and redshift-space galaxy positions are modelled.

Our model distinguishes between the 'central' galaxy in a halo and all the other galaxies ('satellites'). We assume that central galaxies have the same positions and velocities as the haloes in the dark matter simulation. In other words, central galaxies are at the centre of the haloes, and the satellites are located around them. An important assumption in the model is that all galaxy properties—their numbers, spatial distributions, velocities, luminosities, and colours—are determined by halo mass alone. These galaxy properties are constrained by SDSS observations, including the luminosity function (Blanton *et al.*, 2003), luminosity-dependent two-point clustering (Zehavi *et al.*, 2005; Skibba *et al.*, 2006; Zheng, Coil & Zehavi, 2007), and the colour-magnitude distribution and colour-dependent clustering (Skibba, 2009). Note that the clustering constraints result in a mock catalogue that approximately reproduces the observed environmental dependence of luminosity and colour, on scales of $100\,h^{-1}\mathrm{kpc}$ to $30\,h^{-1}\mathrm{Mpc}$.

The number of satellite galaxies in the model follows a Poisson distribution with a mean value that increases with halo mass. The satellites are distributed around the halo centre so that they follow a Navarro, Frenk & White (1996, 1997) profile with the

mass-concentration relation from Macciò, Dutton & van den Bosch (2008). We assign redshift-space coordinates to the mock galaxies assuming that a galaxy's velocity is given by the sum of the velocity of its parent halo plus a virial motion contribution that is drawn from a Maxwell-Boltzmann distribution with dispersion that depends on halo mass (S06).

We specify a minimum r-band luminosity for the galaxies in the catalogue, $M_r - 5\log(h) = -19$, to stay well above the resolution limit of the Millennium Simulation, avoiding any issues of completeness that may bias our results. We generate luminosities for the central galaxies, while accounting for the stochasticity between their luminosities and host halo mass, and then we generate the satellite luminosities so that the observed luminosity distribution is reproduced for $M_r - 5\log(h) \leq -19$ (S06).

We model the observed $g-r$ colour distribution at a given luminosity as the sum of two Gaussian components, commonly referred to as the 'blue cloud' and 'red sequence'. Our colour model has five constraints as a function of luminosity: the mean and scatter of the red sequence, mean and scatter of the blue cloud, and the blue fraction. We assume that the colour distribution at fixed luminosity is approximately independent of halo mass, and that the satellite colour distribution varies such that its mean increases with luminosity (i.e., the satellite red fraction increases with luminosity in a particular way). These two assumptions are tested and verified with galaxy group catalogues in Skibba (2009).

This procedure produces a mock galaxy catalogue containing 1.84 million galaxies, of which 29 percent are satellites. Galaxies occupy haloes with masses ranging from 10^{11} to $10^{15.3}\,h^{-1}\mathrm{M}_{\odot}$. We also construct a mock light cone from the catalogue by selecting galaxies that are within a radial distance of $500\,h^{-1}\mathrm{Mpc}$ from one corner of the box. This gives an opening angle of 90×90 degrees and a depth of $500\,h^{-1}\mathrm{Mpc}$, for which right ascension and declinations are determined. The analysis in Section 3.4 is carried out using a sample of galaxies that are common to both the box and the cone and are chosen so not to be affected by edges. Figure 3.1 shows the mean number of galaxies as a function of halo mass, for two luminosity thresholds (L_{min}). By construction, the number of galaxies consists of the number of central galaxies plus the number of satellites, such that

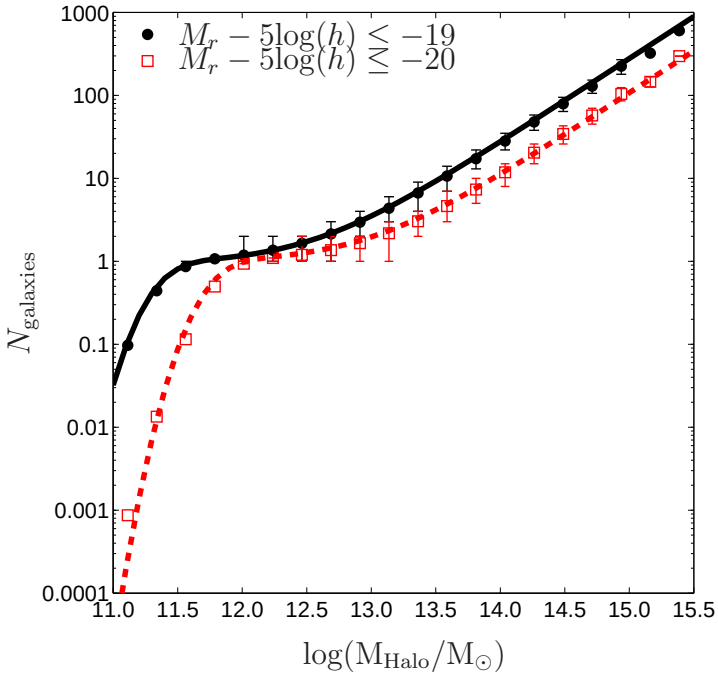

Figure 3.1: The mean number of galaxies above a given luminosity present in dark matter haloes of different mass. Error bars denote the 16th and 84th percentiles and are plotted for haloes that on average host at least 1 galaxy. Lines represent the input model and correspond to Equation 3.1.

$$\langle N_{\rm gal}|M, L_{\rm min}\rangle \;=\; \langle N_{\rm cen}|M, L_{\rm min}\rangle \left[1 + \langle N_{\rm sat}|M, L_{\rm min}\rangle\right] \tag{3.1}$$

where,

$$\langle N_{\rm cen}|M\rangle \;=\; \frac{1}{2}\left[1 \;+\; {\rm erf}\left(\frac{\log(M/M_{\rm min})}{\sigma_{\log M}}\right)\right] \tag{3.2}$$

and

$$\langle N_{\rm sat}|M\rangle = \left(\frac{M - M_0}{M_1^{'}}\right)^{\alpha}. \tag{3.3}$$

The luminosity of the central galaxy is related to the mass of the halo,

$$P(\log L_{\rm cen}|M) = \frac{1}{\sqrt{2\pi}\sigma_{\log L}} \exp\left[-\frac{[\log(L_{\rm cen}/\langle L_{\rm cen}|M\rangle)]^2}{2\sigma^2_{\log L}}\right]. \tag{3.4}$$

(See Appendix A2 of SS09 for details). All of the free parameters depend on luminosity. The slope of the power law, α, is nearly unity. One may define a parameter M_1, which is equal to or slightly larger than $M_1^{'}$ (Zheng, Coil & Zehavi, 2007), and is proportional to the minimum halo mass: $M_1 \approx 20\, M_{\rm min}$. This determines the mass above which haloes typically host at least one satellite galaxy. Therefore, since for $M_r \leq -19$ the minimum halo mass is $\approx 10^{11.5}\, h^{-1}{\rm M}_{\odot}$, the mean number of galaxies rises rapidly like a linear power law at masses larger than twenty times this value, or $\approx 10^{12.8}\, h^{-1} M_{\odot}$, as seen in Figure 3.1.

At the high halo mass end, galaxy number shows a near linear relationship with dark matter halo mass, which occurs by construction in the halo occupation model. This implies that the number of galaxies per unit dark matter mass is constant, or put another way, each galaxy contributes the same mass of dark matter to the cluster. This is in agreement with the findings of Poggianti *et al.* (2010) and to some degree is the natural consequence of a structure built hierarchically. This also agrees with Blanton & Berlind (2007) who find that galaxy distributions are only affected by the host dark matter halo, and not by the surrounding density field, for the SDSS galaxy group catalogue.

The $r-$band luminosity function of galaxies in the mock catalogue is shown in Figure 3.2 and is compared to both the observed SDSS luminosity function (Yang, Mo & van den Bosch, 2009) and a popular semi-analytic galaxy formation model (De Lucia & Blaizot, 2007). In Figure 3.3 we show the mock two-point correlation functions of all, red, and blue galaxies and compare them with the equivalent SDSS measurements of Zehavi *et al.* (2005). Note that the colour-dependent two-point function measured by Zehavi *et al.* (2011) is slightly different from that constrained in the mock, likely due to the presence of the Sloan Great Wall in the real data, an unusually massive supercluster at $z \sim 0.08$.

We have made the mock galaxy catalogue as realistic as possible, and although the catalogue reproduces the observed environmental dependence of luminosity and colour, there are nonetheless a few limitations to the model. For example, we have assumed virialised (dynamically relaxed) dark matter haloes even though some haloes are not, such as those having recently experienced a merger (e.g. Macciò *et al.*, 2007). We have also assumed that central galaxies are always the brightest galaxy in a halo and lie at the centre of their potential well, although in a nonzero fraction of haloes, especially massive haloes, this assumption is not valid (Skibba *et al.*, 2011). Finally, we force satellite galaxy properties to depend only on halo mass, not on halo-centric position, although there is evidence of such a dependence at fixed mass (e.g. van den Bosch *et al.*, 2008a; Hansen *et al.*, 2009). While our mock galaxy catalogue resembles a spectroscopic catalogue, some environment measures used in the literature are based on photometric data (e.g. Gallazzi *et al.*, 2009); for tests with such measures one can add scatter to the redshifted mock galaxy positions, for example.

3.3 Environmental Measures

There are many different methods of measuring galaxy environment available in the literature. Most of these can be categorised into two broad groups: those which use neighbour finding and those that use a fixed aperture. An overview of the methods used in this Chapter are presented in the following subsections and summarised in Table 3.1 along with the authors who implemented them.

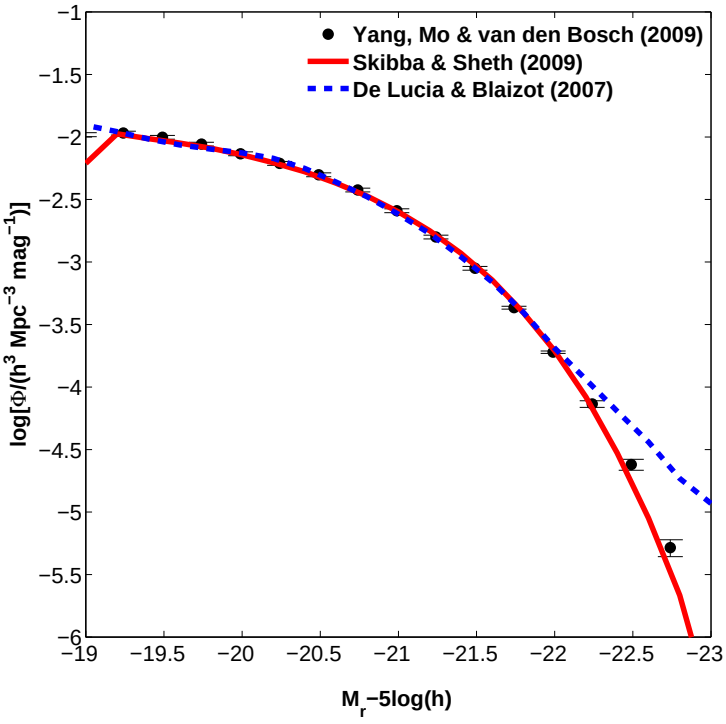

Figure 3.2: The r-band luminosity function for the mock galaxy catalogue created using the HOD of Skibba & Sheth (2009) (red line) compared with that of the semi-analytic De Lucia & Blaizot (2007) model (blue line) and the SDSS observed values (Yang, Mo & van den Bosch, 2009) (black points with errors).

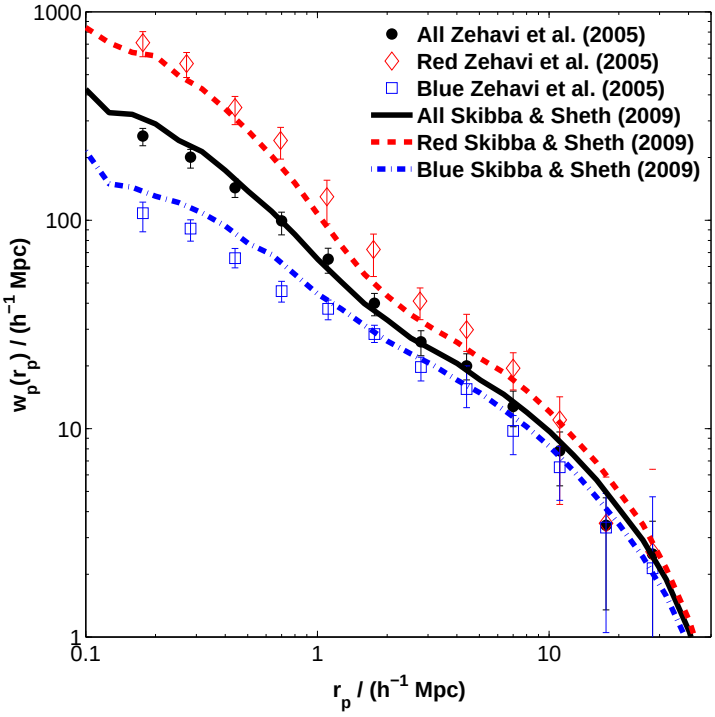

Figure 3.3: The two-point correlation function of all, red, and blue galaxies in the mock catalogue (lines), compared with the equivalent observed results in the SDSS from Zehavi *et al.* (2005) (points with errors).

Num.	Method	Author
	Neighbours	
1	3rd Nearest Neighbour	Muldrew
2	Projected Voronoi	Podgorzec & Gray
3	Mean 4th & 5th Nearest Neighbour	Baldry[1]
4	5 Neighbour Cylinder	Li[2]
5	7th Projected Nearest Neighbour	Ann
6	10 Neighbour Bayesian Metric	Cowan[3]
7	20 Neighbour Smooth Density	Choi & Park[4]
8	64 Neighbour Smooth Density	Pearce
	Aperture	
9	$1\,h^{-1}\mathrm{Mpc}$ ($\pm 1000\,\mathrm{km\,s^{-1}}$)	Grützbauch & Conselice[5]
10	$2\,h^{-1}\mathrm{Mpc}$ ($\pm 500\,\mathrm{km\,s^{-1}}$)	Gallazzi[6]
11	$2\,h^{-1}\mathrm{Mpc}$ ($\pm 1000\,\mathrm{km\,s^{-1}}$)	Grützbauch & Conselice
12	$2\,h^{-1}\mathrm{Mpc}$ ($\pm 6000\,\mathrm{km\,s^{-1}}$)	Gallazzi[6]
13	$5\,h^{-1}\mathrm{Mpc}$ ($\pm 1000\,\mathrm{km\,s^{-1}}$)	Grützbauch & Conselice
14	$8\,h^{-1}\mathrm{Mpc}$ Spherical	Croton[7]
	Annulus	
15	$0.5 - 1.0\,h^{-1}\mathrm{Mpc}$ ($\pm 1000\,\mathrm{km\,s^{-1}}$)	Wilman & Zibetti[8]
16	$0.5 - 2.0\,h^{-1}\mathrm{Mpc}$ ($\pm 1000\,\mathrm{km\,s^{-1}}$)	Wilman & Zibetti[8]
17	$0.5 - 3.0\,h^{-1}\mathrm{Mpc}$ ($\pm 1000\,\mathrm{km\,s^{-1}}$)	Wilman & Zibetti[8]
18	$1.0 - 2.0\,h^{-1}\mathrm{Mpc}$ ($\pm 1000\,\mathrm{km\,s^{-1}}$)	Wilman & Zibetti[8]
19	$1.0 - 3.0\,h^{-1}\mathrm{Mpc}$ ($\pm 1000\,\mathrm{km\,s^{-1}}$)	Wilman & Zibetti[8]
20	$2.0 - 3.0\,h^{-1}\mathrm{Mpc}$ ($\pm 1000\,\mathrm{km\,s^{-1}}$)	Wilman & Zibetti[8]

Table 3.1: List of environment measures used in this study and the authors who implemented them, including references where applicable. See Section 3.3 for further details. References: 1: Baldry *et al.* (2006), 2: Li *et al.* (2011), 3: Cowan & Ivezić (2008), 4: Park *et al.* (2007), 5: Grützbauch *et al.* (2011), 6: Gallazzi *et al.* (2009), 7: Croton *et al.* (2005) and 8: Wilman, Zibetti & Budavári (2010).

3.3.1 Nearest Neighbour Environment Measures

The principle of nearest neighbour finding is that galaxies with closer neighbours are in denser environments. To create a standard measure for this, a value of n is chosen that specifies the number of neighbours around the point of interest. In its simplest form, the projected surface density of galaxies, σ_n, can then be defined as

$$\sigma_n = \frac{n}{\pi r_n^2} \, , \tag{3.5}$$

where n is the number of neighbours within the projected distance r_n, the radius to the n-th nearest neighbour. One disadvantage of quantifying environment using projected statistics is that two galaxies can appear close together when they are in fact just a chance alignment and are actually separated by a larger distance in the third dimension. While there is no simple way to overcome this observationally, one can adopt a velocity cut about each galaxy, typically of order $\pm 1000\,\mathrm{km\,s^{-1}}$, to minimise the number of such alignments.

For data where a third dimension has been measured for each galaxy (e.g. redshift), the denominator of Equation 3.5 is replaced by the enclosed volume:

$$\Sigma_n = \frac{n}{(4/3)\pi r_n^3} \, . \tag{3.6}$$

When using three dimensions careful consideration of redshift distortions are needed and this often leads to two dimensional projected distances being used. The nearest neighbour estimator was recently applied to the Galaxy and Mass Assembly catalogue (GAMA; Driver *et al.*, 2011) by Brough *et al.* (2011) using the distance to the first nearest neighbour above a given luminosity, although typically 3-10 neighbours are used.

Variations on the n-th nearest neighbour approach have been proposed in an attempt to improve the robustness of statistic as a measure of local density. One such method used by Baldry *et al.* (2006) was to take the average of two different neighbour densities, in their case the 4th and 5th nearest neighbour projected surface densities. An alternative proposed by Cowan & Ivezić (2008) was to use the distance to every neighbour up to

the tenth instead of just the distance to the tenth to calculate the density. They adopted a Bayesian metric such that

$$\phi = C\frac{1}{\sum_{i=1}^{10} d_i^3}\ , \tag{3.7}$$

where $C = 11.48$ is empirically determined so that the mean of ϕ matches the number density when the density is estimated on a regular grid for a uniform field, and d_i is the distance to neighbour i.

One can also use numerical simulations to guide the nearest neighbour calibration. Calculating densities using neighbours has long been used in Smooth Particle Hydrodynamics (SPH) and this technique can be applied to galaxies in simulations. SPH calculates the density around a point by weighting each neighbour based on its distance from the point, with the smoothed galaxy density defined as

$$\rho = \sum_{i=1}^{n} W(|r_i|, h)\ . \tag{3.8}$$

Here, n is the number of neighbours used and $W(|r_i|, h)$ is the weighting given by

$$W(r,h) = \frac{8}{\pi h^3}\begin{cases} 1 - 6\left(\frac{r}{h}\right)^2 + 6\left(\frac{r}{h}\right)^3 & 0 \leq \frac{r}{h} \leq \frac{1}{2} \\ 2\left(1 - \frac{r}{h}\right)^3 & \frac{1}{2} < \frac{r}{h} \leq 1\ , \\ 0 & \frac{r}{h} > 1 \end{cases} \tag{3.9}$$

where r is the distance to each neighbour and h is the distance to the n-th nearest neighbour. This weighting corresponds to the spline kernel of Monaghan & Lattanzio (1985) and is the standard kernel of SPH[1]. This method was used with 20 neighbours in Park *et al.* (2007), but values of 32 and 64 are more common in SPH.

Another way to constrain local galaxy density using neighbours was proposed by Li *et al.* (2011) for the Redshift One LDSS-3 Emission line Survey (ROLES; Gilbank *et al.*, 2010). Li *et al.* (2011) considered the volume element of the nearest neighbour found by constructing a three dimensional cylinder using the five nearest neighbours to define its radius and depth. In other words, this technique encloses the five nearest

[1]We have adopted the notation of h corresponding to the point at which the kernel equals zero as opposed to $2h$ as is used in traditional SPH literature. This is just a notational change.

neighbours in a cylinder that no longer has to be centred on the galaxy being sampled, and leads to a better estimate of the relevant volume when compared with simply using a sphere of radius the fifth nearest neighbour.

Further consideration of the volume can be made by calculating the Voronoi volumes around each galaxy as a measure of the environment (e.g. Marinoni *et al.*, 2002; Cooper *et al.*, 2005). Voronoi volumes are polyhedrons constructed by bisecting the distance vectors to the nearest neighbours. Each galaxy will have a volume around it, for which it does not have to be at the centre, defining the points in space that are closer to it than any other galaxy. This gives an estimate of the local density. Unlike the other neighbour-based methods, the number of neighbours used to define the shape of the volume probed is not fixed, which makes the technique fully adaptive. For this study a projected Voronoi measurement is made by collapsing galaxies into two dimensional slices of $50\,h^{-1}\mathrm{Mpc}$ in depth. The Voronoi shapes are then constructed on these surfaces to calculate the surface density of each galaxy.

In Section 3.4 we apply a number of the above nearest neighbour methods to the mock galaxy catalogue described in Section 3.2 and quantify their relative strengths, weaknesses and optimal applications.

3.3.2 Fixed Aperture Environment Measures

In contrast to nearest neighbour methods, which define environment using a varying scale around each galaxy set by the distance to a pre-determined number of galaxy neighbours, fixed aperture methods instead probe a fixed area or volume around each galaxy, within which the number of neighbours are counted. The more galaxies inside this area or volume, the denser the environment is assumed to be, and vice versa.

Fixed aperture measures are often expressed as a density contrast, δ, instead of a density, ρ. Density contrast rescales the aperture count with respect to the mean and is typically defined as

$$\delta \equiv \frac{\delta\rho}{\rho} = \frac{N_g - \bar{N}_g}{\bar{N}_g}\,, \tag{3.10}$$

where N_g is the number of galaxies found in the aperture, and $\bar{N}_g$ is the mean number

of galaxies that would be expected in the aperture if galaxies were instead distributed randomly throughout the entire volume.

The fixed aperture technique was used by Croton *et al.* (2005) to investigate the environments around galaxies in the 2dF Galaxy Redshift Survey (Colless *et al.*, 2003). Croton *et al.* (2005) used spherical apertures of radius $8\,h^{-1}\mathrm{Mpc}$, having investigated a range of sizes from of $4\,h^{-1}\mathrm{Mpc}$ to $12\,h^{-1}\mathrm{Mpc}$ (see also Abbas & Sheth, 2006).

When distance information is not of sufficient accuracy (or absent), apertures in this methodology are instead projected on to the sky. Where possible, authors will then impose a velocity cut of order $\pm 1000\,\mathrm{km\,s^{-1}}$ to minimise interlopers (e.g. Grützbauch *et al.*, 2011), for the same reasons discussed in Section 3.3.1. The magnitude of this velocity cut can vary depending on distance uncertainties. This was investigated by Gallazzi *et al.* (2009) who found velocity cuts of $\pm 6000\,\mathrm{km\,s^{-1}}$ ($dz = 0.02$) represent the typical photometric redshift uncertainty and $\pm 500\,\mathrm{km\,s^{-1}}$ ($dz = 0.0015$) represent the typical spectroscopic redshift uncertainty. Such errors can often have a detrimental effect on the measured density if not appropriately accounted for. Note that when a velocity cut is imposed, an otherwise spherical aperture elongates into a cylinder in three dimensional space, within which galaxy counts are then taken. Whether this distortion is important for the environment measure depends on the focus of the analysis. Typical scales for the radius of an aperture range from $1\,h^{-1}\mathrm{Mpc}$ to $10\,h^{-1}\mathrm{Mpc}$, probing environments spanning individual haloes to large super-structures and voids in the cosmic web.

A variation on the fixed aperture method was proposed in Wilman, Zibetti & Budavári (2010), where counts were taken in annuli of increasing inner and outer radius, rather than within a single fixed aperture volume. This technique enables the larger scale environment to be probed and the influence of local regions around individual galaxies to be removed. In its optimal form different sized annuli are applied in combination with apertures to better constrain the halo size and changes of environment with distance from the galaxy.

Finally, in addition to environment being defined by galaxy positions within the volume, we also measure environment as inferred from the background dark matter distribution. To obtain the neighbourhood dark matter environment in the Millennium

Simulation the full volume is broken into a three dimensional grid with side-length $2\,h^{-1}\mathrm{Mpc}$. At the centre of each grid element a three dimensional Gaussian density is calculated using the local dark matter particles, smoothed over three different scales: 2.5, 5, and $10\,h^{-1}\mathrm{Mpc}$. This Gaussian smoothed density is similar to the kernel smoothed density of Equation 3.8, but with a dark matter particle mass term in the sum.

In Section 3.4 we apply a number of fixed aperture methods to the mock galaxy catalogue and measure local density around each galaxy. This allows us to quantify the properties that aperture measured densities best probe, and compare with the previously described nearest neighbour estimators.

3.4 Results

To investigate the different properties of each galaxy environment measure, in this section we consider how they correlate with (1) the host dark matter halo mass, (2) the underlying dark matter environment, and (3) the colour of the galaxies.

To facilitate this we have converted the output of each to a 'percentage rank' for each galaxy. This is computed by listing the galaxies in order of increasing density, then assigning them a percentage based on where they appear in that list, with zero percent being the least dense and one hundred percent the most dense. Therefore, a galaxy with a percentage rank of ninety-five has five percent of the galaxies in the sample denser than it and ninety-five percent less dense than it. This normalisation provides a fairer comparison between environment estimators and probes their relative rather than absolute distributions across the environment spectrum, which would otherwise be definition dependent.

Throughout this Section we present results using a selection of environment measures that illustrate general trends. For completeness, in Appendix A we repeat all the Figures presented here using the complete set of environment measures listed in Table 3.1.

3.4.1 Dark Matter Halo Mass

By design, the most fundamental property for a galaxy within our model is its dark matter halo mass. Halo mass determines both the spatial distribution of the galaxy population and the individual galaxy properties. Therefore, each environment measure should reveal some underlying correlation. Typically halo masses of $\sim 10^{12}\,h^{-1}\mathrm{M}_{\odot}$ correspond to the field, $\sim 10^{13.5}\,h^{-1}\mathrm{M}_{\odot}$ to groups and $\sim 10^{15}\,h^{-1}\mathrm{M}_{\odot}$ to clusters.

3.4.1.1 Nearest neighbour results

Figure 3.4 shows contours of the abundance of galaxies that have environments of a given percentage rank plotted against the host halo mass, for four different nearest neighbour-based techniques, with the number of neighbours increasing from left to right. These are: the 3rd nearest neighbour density in three dimensions, the surface density for the projected 7th nearest neighbour, the three dimensional density using a 10 neighbour Bayesian metric, and the smooth kernel three dimensional density using 64 neighbours.

The most noticeable feature of all panels in Figure 3.4 is that galaxies divide into two distinct groups, with the top ~ 20 percent dense environments occupied by galaxies in haloes more massive than $\sim 10^{12.5}\,h^{-1}\mathrm{M}_{\odot}$, and the remaining ~ 80 percent of environments occupied by galaxies in haloes with masses lower than $\sim 10^{12.5}\,h^{-1}\mathrm{M}_{\odot}$. This bimodality arises from the assumed association between galaxies and dark matter haloes required to fit the observed luminosity function and clustering observations, and is explored further below.

Looking in more detail, the lower 80 percent of rank-ordered densities in Figure 3.4 shows no trend with halo mass, and as such, the term ‘local environment’ no longer applies. In terms of a characteristic halo mass for a given environment, this result leaves individual galaxies near clusters indistinguishable from isolated galaxies in voids.

In contrast, the behaviour of the high density–halo mass correlation depends on the neighbour method employed. In the highest 20 percent environments, low n neighbour searches smooth away any density dependence with halo mass. This can be seen by comparing the far left panel in Figure 3.4 (low n) with the far right panel (high n). As

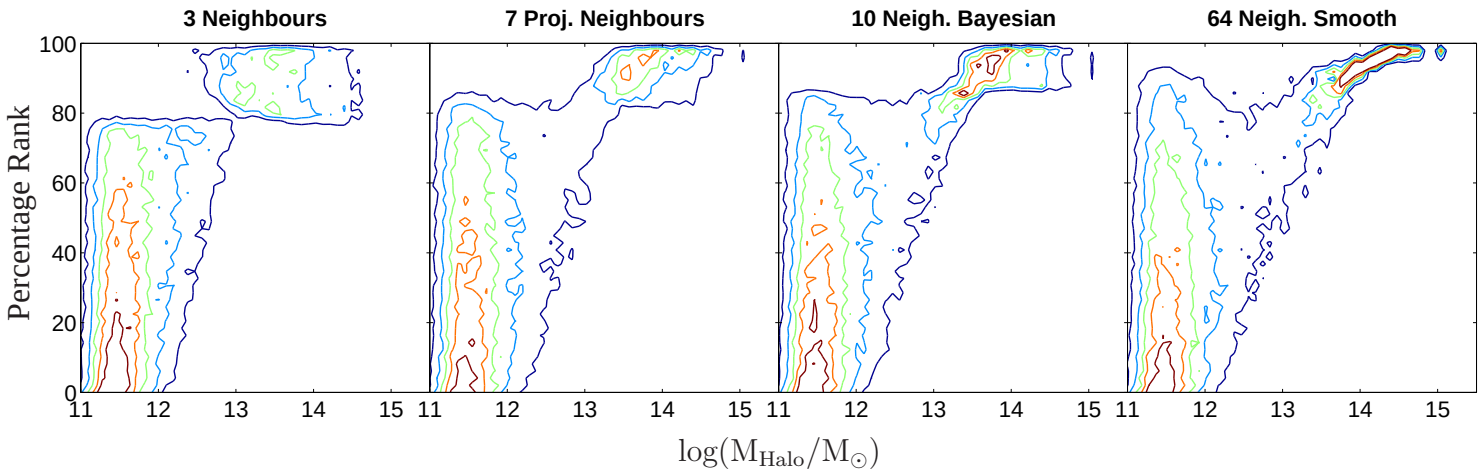

Figure 3.4: The abundance of galaxies that have environments of a given percentage rank plotted against host halo mass, where environment is defined by the (from left to right) 3rd nearest neighbour, 7th projected nearest neighbour, 10 neighbour Bayesian metric and 64 neighbour kernel smoothed (SPH style). Contours are linearly spaced showing regions of constant galaxy number. The bimodal distribution is caused by the neighbour search remaining in or leaving the halo to find the next nearest neighbour.

the number of neighbours used to define environment is increased, galaxies belonging to increasingly massive haloes (which host an increasing number of satellites) will be labelled as increasingly dense. Thus, to more precisely draw out the high density–halo mass environment correlations using nearest neighbour methods, a high n is desirable.

The first two panels of Figure 3.4 provide an additional test of the importance of projection effects. Here, the 3rd nearest neighbour count is performed using three dimensional redshift space distances while the 7th nearest neighbour is performed with projected galaxy positions on the two dimensional sky. Both methods show the same overall trend with halo mass. We find that, in general, projecting the galaxy positions simply blurs the edges of the two clouds with the overall shape preserved.

Another popular neighbour-based method used for measuring environment is Voronoi volumes, as discussed in Section 3.3.1. Figure 3.5 shows how a Voronoi defined environment estimator also correlates with dark matter halo mass. We see a similar trend to that of the other neighbour-based methods, with the overall result close to the 7th nearest projected neighbour method shown in the second panel of Figure 3.4.

A comparison of Figure 3.1 with Figures 3.4 and 3.5 reveals the origin of the bimodality. Galaxies identified to be in the upper 20 percent dense environments tend to be those whose neighbour search stays within the dark matter halo due to a large satellite population. Such haloes are almost always more massive than $\sim 10^{12.5}\,h^{-1}\mathrm{M}_{\odot}$. In contrast, the lower 80 percent density environments are identified by neighbour searches that extend beyond the halo due to a low or zero satellite population of significance. In general, haloes with few satellites almost always have masses smaller than $\sim 10^{12.5}\,h^{-1}\mathrm{M}_{\odot}$, and neighbour searches will then tend to probe the inter-halo rather than inter-galaxy separations.

3.4.1.2 Fixed aperture results

Many authors have employed fixed apertures to probe the local density around galaxies, as described in Section 3.3.2. In a similar vein to Figure 3.4, Figure 3.6 shows how various aperture sizes correlate with host dark matter halo mass when a projected fixed aperture is employed with a cut in velocity space around each galaxy. In addi-

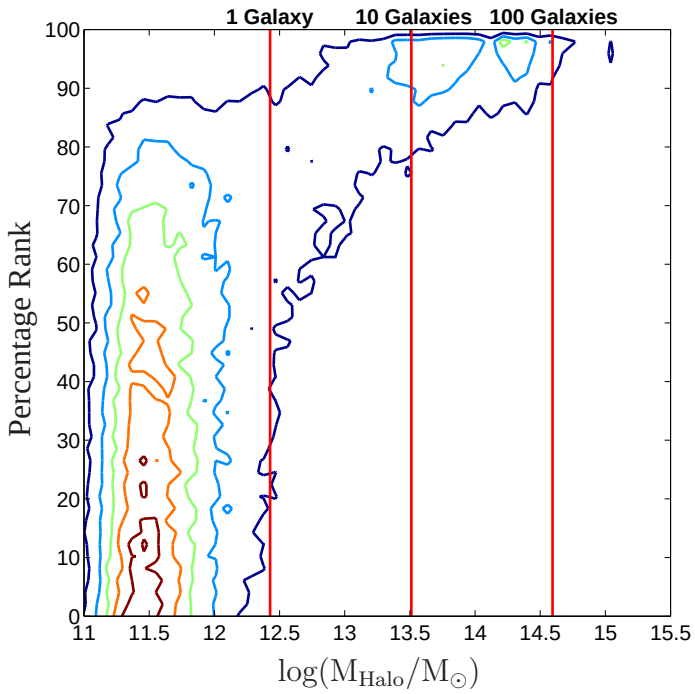

Figure 3.5: The percentage rank of galaxy environments plotted against dark matter halo mass, as in Figure 3.4, this time for the Voronoi method. Contours are linearly spaced showing regions of constant galaxy number. Vertical lines represent typical dark matter halo masses that host 1, 10 and 100 galaxies with $M_r - 5\log(h) \leq -19$ (see Figure 3.1)

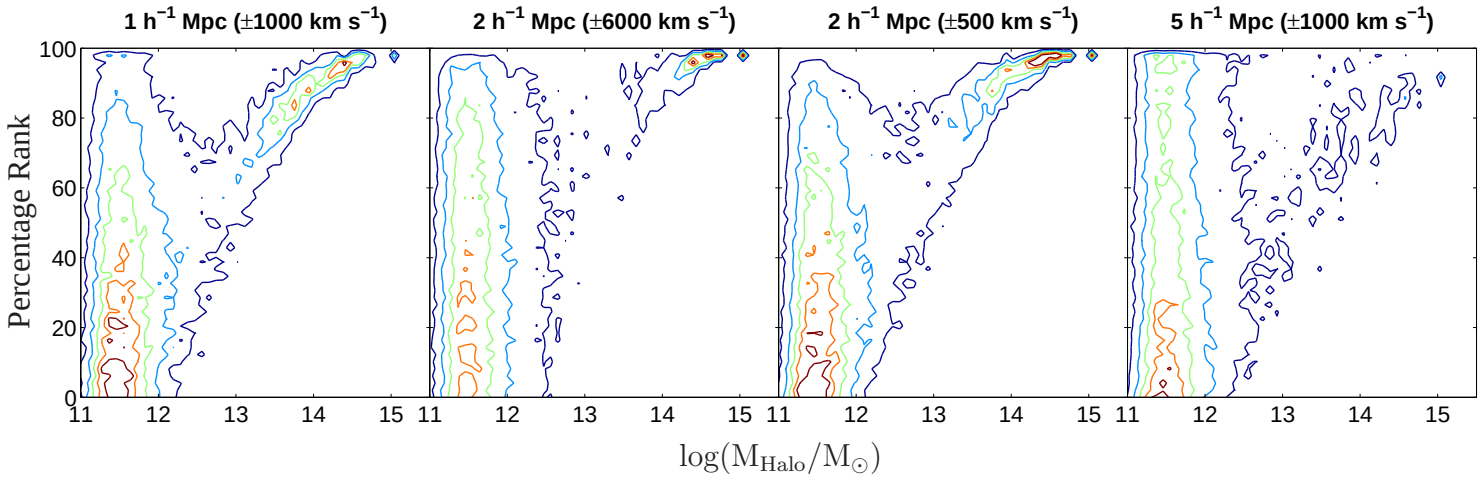

Figure 3.6: The percentage rank of galaxy environment against dark matter halo mass, as in Figure 3.4, for (from left to right) a $1\,h^{-1}\mathrm{Mpc}$ aperture with a velocity cut of $\pm 1000\,\mathrm{km\,s^{-1}}$, a $2\,h^{-1}\mathrm{Mpc}$ aperture with a velocity cut of $\pm 6000\,\mathrm{km\,s^{-1}}$, a $2\,h^{-1}\mathrm{Mpc}$ aperture with a velocity cut of $\pm 500\,\mathrm{km\,s^{-1}}$ and a $5\,h^{-1}\mathrm{Mpc}$ aperture with a velocity cut of $\pm 1000\,\mathrm{km\,s^{-1}}$. Contours are linearly spaced showing regions of constant galaxy number.

tion, the central two panels show how the density–halo mass correlation changes if the velocity cut is increased for the same sized aperture. This roughly corresponds to the difference one would expect with data having photometric vs. spectroscopic redshifts, as discussed in Gallazzi *et al.* (2009).

The projected fixed aperture technique yields both similar and different trends when compared with the nearest neighbour technique shown in Figure 3.4. The overall shape is the same, with galaxies in haloes of mass less than $\sim 10^{12.5}\,h^{-1}\mathrm{M}_{\odot}$ showing little correlation of halo mass with environment. At the high mass end there is a plume of increasing density that is much better defined than found with the nearest neighbour method (especially when compared to choices of low n). This suggests that the fixed aperture methodology is a better probe of halo mass, especially for small apertures and velocity cuts. There is however contamination at a fixed density from low mass haloes due to their close proximity to the high mass halo.

In particular, when there are enough galaxies to define the local large-scale structure, a fixed-scale environment probe is much more sensitive to the power-law nature of the two-point correlation function, where the abundance of close pairs falls off rapidly beyond the halo radius. This leads to the galaxy count in the fixed aperture also falling off rapidly. In contrast, nearest neighbour environment methods adapt the scale probed to keep signal-to-noise fixed. Hence, the division between a halo's interior and exterior becomes much less prominent.

At intermediate to low masses there is no relation between fixed aperture measured density and halo mass, and so the environment parameter breaks down, as is also the case for nearest neighbour environment parameters. From an environment point-of-view, such haloes, which usually host galaxy groups, may be difficult to distinguish from cluster outskirts and from unassociated lower-mass haloes.

As the aperture is increased in size, the trend with halo mass fades when the aperture becomes much larger than the structures present. For example, a super-cluster with a collective mass of $10^{16}\,h^{-1}\mathrm{M}_{\odot}$ would have a radius[2] of $\sim 3.5\,h^{-1}\mathrm{Mpc}$, smaller than the $5\,h^{-1}\mathrm{Mpc}$ aperture shown in the far right panel of Figure 3.6. When an aperture

[2]Radius here is determined by finding the scale at which the enclosed density is 200 times the critical density of the Universe.

becomes large enough the contribution of individual haloes and structures blur and the environment–halo mass trend weakens or disappears. Hence, aperture size should be chosen carefully from the outset and be appropriate for the science questions of interest.

Finally, the two central panels of Figure 3.6 illustrate the importance of velocity (or equivalently distance) uncertainties on the environment measure. Large velocity cuts, as is typically required with photometric data, make measuring environment with a fixed aperture ineffective. This occurs for the same reason as using large apertures. There, the aperture was wider than the structures of interest which smoothed out the signal, while here, the depth of the aperture scatters in superfluous counts from foreground and background objects, diluting any correlation. This does not apply to the highest mass clusters as they dominate the depth reducing the effect of interlopers. Furthermore, any use of the angular correlation function as a probe of environment must first consider the redshift distribution of the galaxies and the uncertainties must be well understood (e.g. Coil *et al.*, 2004; Quadri *et al.*, 2008).

3.4.2 Galaxy Colour

Galaxy colour has been shown to correlate with local galaxy density, with galaxies in over-dense environments being redder compared with those in under-dense environments (cf. cluster and field) (e.g. Lewis *et al.*, 2002; Kauffmann *et al.*, 2004; Cooper *et al.*, 2006; Gallazzi *et al.*, 2009). The model we employ in this paper has a constrained global $g-r$ colour distribution that mimics that of local galaxies in the SDSS (Skibba & Sheth, 2009). Hence, the degree to which different environment metrics can recover this relation can be tested.

Figure 3.7 shows histograms of the $g-r$ colour distribution for the 20 percent most dense and 20 percent least dense galaxies defined with the same four nearest neighbour methods used in Figure 3.4: the 3rd nearest neighbour density in three dimensions, the projected 7th nearest neighbour, density defined from a 10 neighbour Bayesian metric, and the smooth kernel density using 64 neighbours. In the 20 percent most dense environments, all nearest neighbour-based environment measures show a clear red peak and a more weakly populated blue cloud. In contrast, in the lowest 20 percent

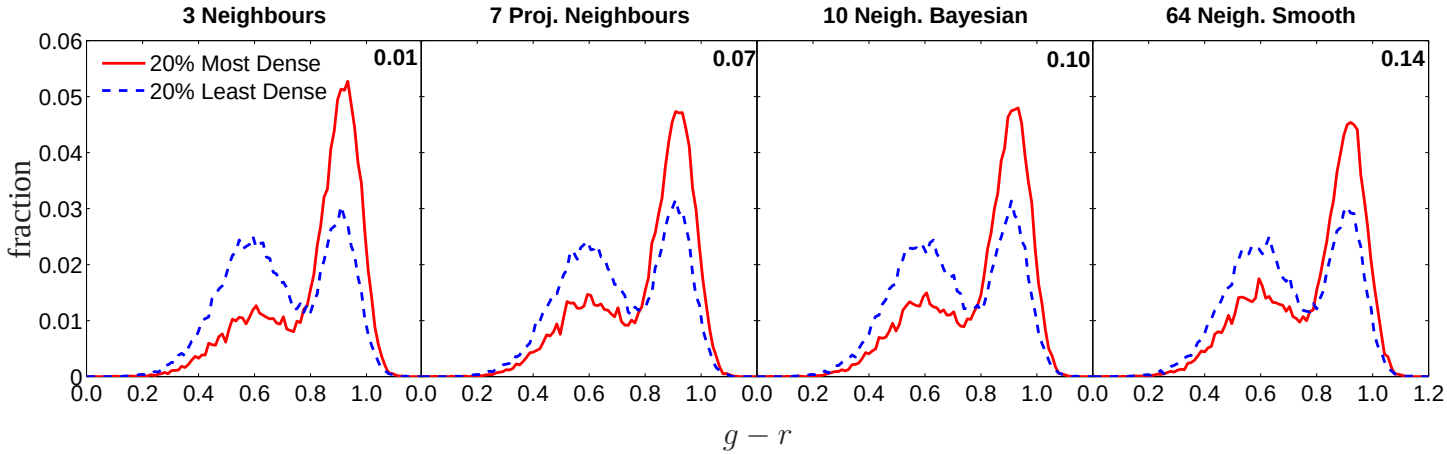

Figure 3.7: Histograms of galaxy colour for the 20 percent most dense (red solid) and 20 percent least dense (blue dashed) galaxies, measured using n-th nearest neighbour statistics, defined by the (from left to right) 3rd nearest neighbour, 7th projected nearest neighbour, 10 neighbour Bayesian metric and 64 neighbour kernel smoothed (SPH style). The number in the upper right of each panel is the Kolmogorov-Smirnov probability that both samples are drawn from the same distribution.

of environments galaxies are split more evenly between the red and blue populations. As the neighbour number is increased (from left to right), there are only small changes in the relative colour distributions in environment extremes. The Kolmogorov-Smirnov probability (Kolmogorov, 1933; Smirnov, 1948) that both samples are drawn from the same distribution is shown in the upper right of each panel.

Figure 3.8 shows histograms of colour for the 20 percent most dense and 20 percent least dense galaxies as probed by fixed apertures of various size, as used previously in Figure 3.6. The central two panels show how these distributions change if the velocity cut is increased or decreased for the same sized aperture. This roughly corresponds to the difference between photometric and spectroscopic redshift uncertainties (Gallazzi *et al.*, 2009) (see Section 3.3.2). For small apertures, the colour distributions of both density extremes look remarkably similar to that found for the nearest neighbour methods shown in Figure 3.7. However, as the volume of the fixed aperture is increased similar trends to that found in the previous Section emerge. In particular, as the aperture becomes larger (either in radius or depth), the differences between the colour distributions of galaxies in environment extremes lessen. Here, the individual properties of galaxies are smoothed over due to the large variety of local environments falling within the aperture. For apertures probing scales much larger than the typical cluster the distinction between environments vanishes. This suggests that environment questions relating to galaxy colour (or properties that correlate with colour) should avoid fixed aperture methods with large smoothing radii or depth (e.g. Croton *et al.*, 2005). Furthermore, the Kolmogorov-Smirnov probabilities indicate that nearest neighbour-based methods detect stronger colour-environment relations than all the apertures tested here.

3.4.3 Dark Matter Environment

Dark matter haloes are known to be biased tracers of the underlying dark matter distribution, and it is interesting to compare how haloes and the smooth background mass field correlate with respect to their environment ranking, and how this relates to the galaxy distribution. To this end, the simulation volume has been divided using a three dimensional grid of side-length $2\,h^{-1}\mathrm{Mpc}$, and the neighbourhood dark matter den-

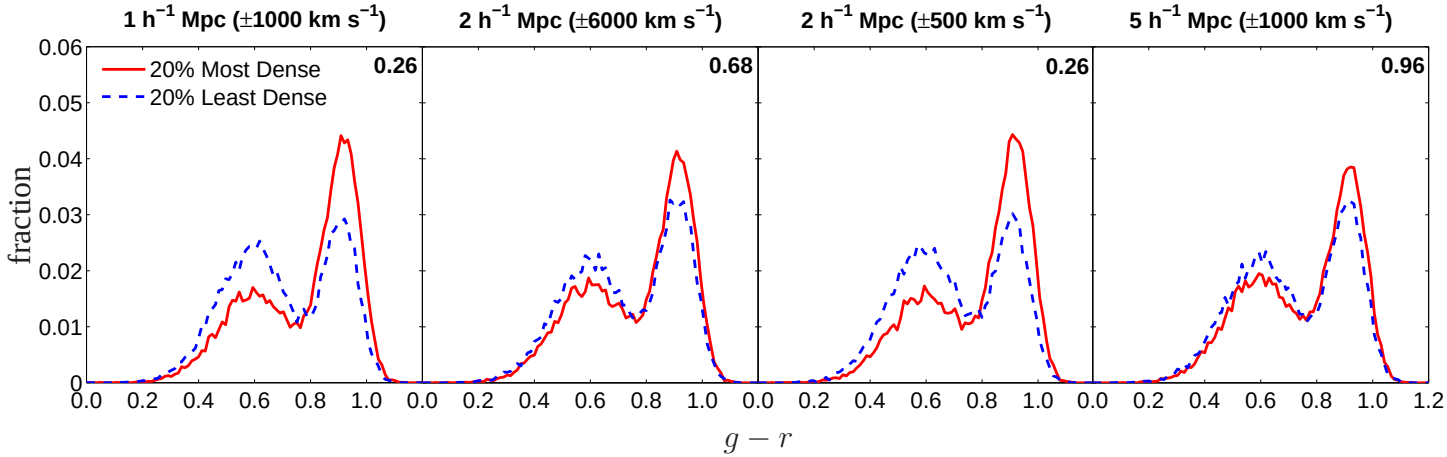

Figure 3.8: Histograms of galaxy colour, as in Figure 3.7, for the 20 percent most dense (red solid) and 20 percent least dense (blue dashed) galaxies, measured using (from left to right) a $1\,h^{-1}\mathrm{Mpc}$ aperture with a velocity cut of $\pm 1000\,\mathrm{km\,s^{-1}}$, a $2\,h^{-1}\mathrm{Mpc}$ aperture with a velocity cut of $\pm 6000\,\mathrm{km\,s^{-1}}$, a $2\,h^{-1}\mathrm{Mpc}$ aperture with a velocity cut of $\pm 500\,\mathrm{km\,s^{-1}}$ and a $5\,h^{-1}\mathrm{Mpc}$ aperture with a velocity cut of $\pm 1000\,\mathrm{km\,s^{-1}}$. The number in the upper right of each panel is the Kolmogorov-Smirnov probability that both samples are drawn from the same distribution.

sity field measured with a Gaussian filter placed at the centre of each grid element, smoothed on three different scales: 2.5, 5.0 and $10\,h^{-1}\mathrm{Mpc}$ (see Section 3.3.2). We compare this to the environment measured directly from central galaxy counts within a fixed spherical aperture of radius $8\,h^{-1}\mathrm{Mpc}$ (Croton *et al.*, 2005).

Figure 3.9 shows how the background dark matter density, Gaussian smoothed on various scales, correlates with the large-scale galaxy density, top-hat smoothed on an $8\,h^{-1}\mathrm{Mpc}$ scale. The correlation is weakest for the smallest Gaussian smoothing scale of $2.5\,h^{-1}\mathrm{Mpc}$, becomes tighter at a scale of $5\,h^{-1}\mathrm{Mpc}$, before becoming weaker again at $10\,h^{-1}\mathrm{Mpc}$. The point of tightest correlation between dark matter and galaxy measured density approximately corresponds to the same physical scale being probed by each in three–dimensional space. At fixed dark matter density the scatter in density measured by galaxies is approximately 40 percent. This indicates the degree of precision with which one can probe the smooth background density using galaxies as tracers of the mass distribution.

We have compared the other environment measures used in this Chapter to the background dark matter density and these can be found in Appendix A. In short, a similar trend to Figure 3.9 is found for the 64 neighbour smooth density environment measure, but with the tightest correlation at a radius of $2.5\,h^{-1}\mathrm{Mpc}$. For the other neighbour and small aperture methods, weak correlations are found when plotted against a dark matter density smoothing scale of $2.5\,h^{-1}\mathrm{Mpc}$ but which disappear on larger scales. Environments measured in annuli and projected aperture methods that impose a photometric-type redshift velocity cut show no correlation on any scale due to only the largest clusters dominating the depth cut, while the 10 neighbour Bayesian metric and 20 neighbour smooth density again show a similar correlations to the dark matter smoothing scale of $2.5\,h^{-1}\mathrm{Mpc}$.

3.4.4 Individual Galaxies

In the previous Sections we investigated how different environment parameters correlate with different galaxy properties in a statistical sense by considering the whole sample. As implied by Figures 3.4 and 3.6, when selecting the most and least dense environments different methods will potentially select different galaxy populations. An

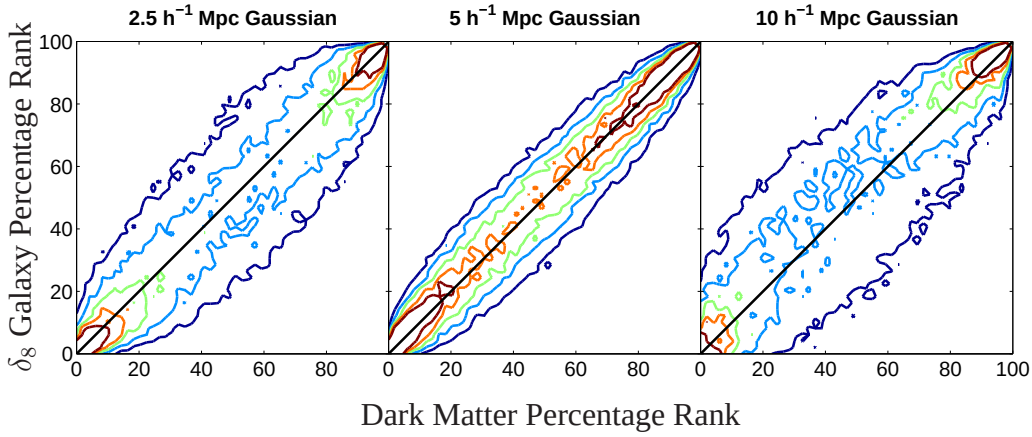

Figure 3.9: The percentage rank of central galaxy environment using an $8\,h^{-1}\mathrm{Mpc}$ spherical aperture plotted against the percentage rank of background dark matter environment measured using a smooth Gaussian filter of radius (from left to right) $2.5\,h^{-1}\mathrm{Mpc}$, $5\,h^{-1}\mathrm{Mpc}$ and $10\,h^{-1}\mathrm{Mpc}$. Contours are linearly spaced showing regions of constant galaxy number.

alternative and complementary way to compare the different environment methodologies is to consider individual galaxies in the mock catalogue and examine how each measure ranks them relative to the others. By considering individual galaxies a better understanding of why these galaxies were chosen can be obtained. This also highlights the consistency (or lack thereof) between different definitions of environment. Below we present one example that is representative of the general behaviour for high mass haloes.

The top panel of Figure 3.10 shows how the different environment measures listed in Table 3.1 compare when one focuses on the central galaxy occupying the fourth most massive halo in the simulation, with mass $10^{15.08}\,h^{-1}\mathrm{M}_{\odot}$. The environment measures are separated into three groups based on the technique they use: neighbours, aperture and annulus. All environment measures place this galaxy within the top 10 percent of rank ordered densities in the simulation volume, with the majority placing it within the top one percent. When considering annuli to define environment, the top panel of Figure 3.10 shows that the further one moves from the centre of the halo the lower the rank density measured. This simply highlights that the outer regions of a halo tend to be less dense than the core. When considering aperture methods there is less of a trend between different definitions. However, for a fixed depth, increasing the aperture size reduces the rank density measured, while for fixed aperture size, the density rank appears sensitive to the inclusion of both the halo core (smaller velocity cut) and full extent (larger velocity cut). As mentioned in previous sections, the larger velocity cut used to represent photometric redshift uncertainties has a smaller effect on large clusters as the cluster members dominate the galaxies within the depth cut. For neighbour-based methods there is a general increase in the rank density as the neighbour number increases. This is due to the increased neighbour count contributing from within the galaxy halo. Specifically, as the number of neighbours increases galaxies in smaller haloes are demoted down the rank list, and so the galaxies in large haloes are promoted.

The bottom panel of Figure 3.10 shows how the different density estimators rank the most distant satellite associated with the central galaxy of the same $10^{15.08}\mathrm{M}_{\odot}$ halo used in the top panel. This is a test of how satellites on the outskirts of cluster environ-

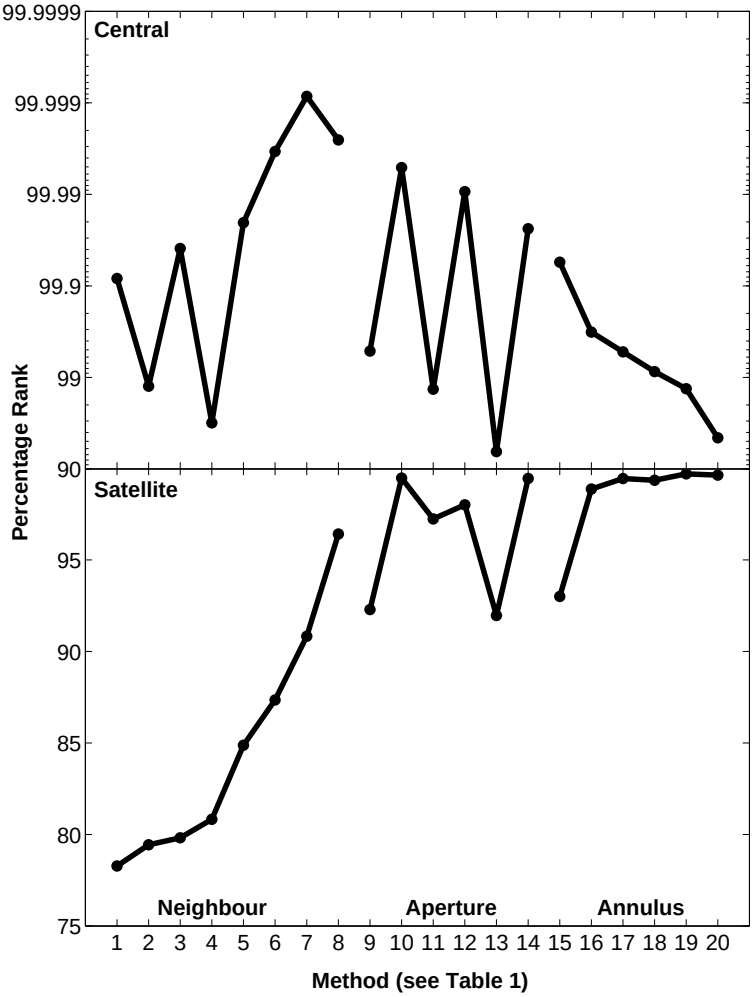

Figure 3.10: (top) The percentage rank of various density estimators (see Table 3.1) for a single central galaxy living in the fourth most massive halo in the simulation. The density methods are grouped by increasing neighbour number, increasing aperture and increasing inner radius of an annulus. (bottom) The same as the top panel, but this time the percentage density ranking of the outer most satellite galaxy in the same halo for each method.

ments would be classified in each density scheme. The range of environment ranking is much larger between the different measures, with the apertures and annuli mostly finding higher rank densities than the neighbour estimates. This again comes back to scale, with neighbour methods probing the internal properties of the outer halo, and aperture and annulus methods being sensitive to the larger structure of the halo and its surrounds. Additionally, the trend of increasing rank density with increasing neighbour number is again seen as the neighbour count reaches deeper into the halo core from the boundary.

3.5 Discussion and Summary

The phrase 'galaxy environment' is a very general concept that has been used in the literature in a variety of ways. Its definition – what it measures and how it is measured – can vary from author to author. This creates uncertainty when trying to compare results for environmental trends. In practise, galaxy environment is quantified in one of two ways: by the distance to the n-th nearest neighbour or by using a fixed aperture to probe the surrounds. Over the course of time these two methods have evolved in the literature. However, both methods and their variants provide a measure of the density field surrounding a galaxy and hence can be used to answer specific environment-related questions.

To fairly compare many different environment measures one would ideally like to use a common galaxy catalogue as a starting point. This was achieved in this Chapter by applying a halo occupation distribution model to the $z = 0$ output of the Millennium dark matter simulation. Our model is designed to accurately reproduce the luminosity, colour and spatial distribution of galaxies in the Sloan Digital Sky Survey. The resulting data cube was also used to generate a mock light cone so that the environment measures could be applied in a more realistic geometry.

Comparing neighbour and aperture based environment measures to the dark matter halo mass of a galaxy reveals how they measure different aspects of the halo. In particular, nearest neighbour methods that use a small enough neighbour number best probe the internal properties of the halo. For haloes that contain fewer galaxies than

the neighbour number, the inter-halo separation dominates the calculation and galaxy–environment correlations tend to wash out. In contrast, aperture measures tend to better probe the halo as a whole and so lead to larger density values corresponding to larger haloes, which more accurately reflect their larger masses. A smaller aperture than those studied here could be used to probe cluster environments on a scale similar to the nearest neighbour-based methods, but these would be unsuitable for the field due to the distance between neighbours being too large. This is in agreement with the findings of Haas, Schaye & Jeeson-Daniel (2012).

The galaxy density internal to a halo's boundary was found to be independent of its mass when probed using the neighbour method. While galaxies at the edge of a halo are always in less dense environments than those at the centre, the galaxy environment at the centre of intermediate mass haloes is approximately the same as that at the centre of very massive ones.[3] By fitting the number of galaxies for a given halo mass, we find that the number of galaxies per unit dark matter mass is constant and this is in agreement with the findings of Poggianti *et al.* (2010).

When comparing how the different environment measures distribute galaxy colour, almost all methods recover the observed correlation that galaxies are redder in denser environments compared to those in less dense environments. This relation only disappears for very large apertures, of order $> 5\,h^{-1}\mathrm{Mpc}$. On scales larger than this the most dense and least dense galaxies are found to have similar colour distributions. Here, the aperture is large enough to encompass a statistically representative number of different haloes, resulting in a smoothing out of the colour differences over such large volumes. This behaviour is also expected to extend to any property that correlates strongly with colour.

On the other hand, very large fixed apertures are the most accurate at recovering the large-scale dark matter environment. For example, an $8\,h^{-1}\mathrm{Mpc}$ spherical aperture used to calculate the galaxy density correlates well with the dark matter environment measured using Gaussian smoothing on $5\,h^{-1}\mathrm{Mpc}$ scales. Similar results are found

[3]The concentration and mass of dark matter haloes are anti-correlated, and since the number density distribution of galaxies follows that of the dark matter particles (Yang *et al.*, 2005), the central concentration of galaxies should also vary slightly with halo mass. In practice, however, the trend is difficult to detect observationally.

with high number n-th neighbour estimates. The important parameter here is scale, with larger probed scales better correlated than smaller scales.

In addition to the environment measures themselves, we also explored the general effects of photometric and spectroscopic redshift uncertainties by varying the velocity cut used to calculate projected environment. For a typical photometric redshift uncertainty most trends with environment disappear or become significantly weaker. This is caused by the depth of the aperture becoming much larger than the objects being probed, and the scattering of interlopers which contaminate the density probe. This effect decreases for the largest clusters as the members dominate the depth cut. We warn that photometric redshifts may be unsuitable for measuring certain properties when using a range of environmental scales, especially at high redshifts.

On a galaxy-by-galaxy basis, most environment methods agree on the relative environment rank of central galaxies in massive haloes (to within a few percent). There is less agreement with the satellite population in clusters, where the result becomes more sensitive to the method employed.

Dark matter haloes are often broadly categorised as residing in 'field', 'group' and 'cluster' environments based solely on their mass. In Figure 3.1, for example, haloes of mass $M \sim 10^{12}\,\mathrm{M}_{\odot}$, $10^{13.5}\,\mathrm{M}_{\odot}$, and $10^{15}\,\mathrm{M}_{\odot}$ approximately correspond to these environment bins, respectively. Many environment analyses use this categorisation, although as we have seen, the distinctions between them can often be blurred in detail. Some studies also attempt to explicitly identify galaxies that are isolated or in groups or rich clusters, for example using Friends-of-Friends group-finding algorithms (e.g. Berlind *et al.*, 2006; Yang *et al.*, 2007). Analyses using group catalogues are complementary to studies with nearest neighbour or fixed aperture measures, or with galaxy clustering (e.g. Weinmann *et al.*, 2006; Martínez & Muriel, 2006; Blanton & Berlind, 2007; van den Bosch *et al.*, 2008a; Balogh *et al.*, 2009; Skibba *et al.*, 2011). Work focused on galaxy clusters has also yielded complementary results (e.g. Poggianti *et al.*, 2008; Rudnick *et al.*, 2009; Bamford *et al.*, 2009; Wolf *et al.*, 2009; Gallazzi *et al.*, 2009).

Importantly, the way a galaxy forms and evolves is clearly related to its environment. Some galaxy properties, such as luminosity, colour, and stellar mass, are directly cor-

related with the large-scale environment through the host dark matter halo (e.g. Zehavi *et al.*, 2005; Li *et al.*, 2006). Other galaxy properties, such as structure, are to some extent only indirectly correlated with the environment (e.g. Kauffmann *et al.*, 2004; Blanton *et al.*, 2005; Cassata *et al.*, 2007). Indeed, a number of authors report that, for many aspects of the galaxy population, environmental dependence is often weak once stellar mass is fixed (van den Bosch *et al.*, 2008a,b; Scodeggio *et al.*, 2009; Bolzonella *et al.*, 2010; Vulcani *et al.*, 2011). In any case, these studies highlight the fact that it is important to carefully determine how a galaxy's environment is characterised, and to identify and navigate the potential aspects of the environment analysis that may bias the results.

The key consideration when picking an environment measure is the scale that is being probed. The term environment is very general but in fact breaks down into two main regions and we argue that the community should agree on a standard terminology for clarity and to avoid future confusion. The first region is the 'local environment' which corresponds to scales internal to a halo. These are best probed using nearest neighbour methods, but the value of n is important. When n is larger than the number of galaxies likely to reside within the halo the usefulness of this environment measure can weaken. The second region lies external to the halo, the 'large-scale environment'. The large-scale environment is best probed using aperture based methods. In general, there is no simple way to probe all environments with a single method, and one should consider carefully the best tool to answer the questions at hand.

This Chapter marks the first in a series of works exploring the meaning and methods of galaxy environment, as measured in the current literature. In the present work we have focused on using a clean sample of mock galaxies to quantify how selected properties of the galaxy population correlate with different environment methods, and how these methods themselves compare. Future work will include investigating the detrimental effects of survey geometry, edges and holes (such as those caused by stars) on environment and techniques that can be applied to successfully overcome them. Furthermore, the relationship between galaxy, halo and dark matter environment warrants additional exploration, as does the redshift dependence of a galaxy's environment (defined in various ways), what the different environment methods tell us about galaxy evolution, and

how these can best be applied to the noisy data of the high redshift Universe.

3.6 Further Published Work

The environment data from this Chapter was used by Skibba *et al.* (2013) to create rank-ordered marked correlation functions to investigate how environment measures relate to clustering. Applying the environment measures described in this Chapter to a semi-analytic catalogue also, allowed Shattow *et al.* (submitted) to investigate the difficulties in using them to identify proto-clusters at $z = 2$ and how these environments evolve to the present day.

Chapter 4

Growth of Supermassive Black Holes

There is strong evidence that supermassive black holes reside in all galaxies that contain a stellar spheroid and their mass is tightly correlated with properties such as stellar bulge mass and velocity dispersion. There are also strong theoretical arguments that feedback from supermassive black holes plays an important role in shaping the high mass end of the galaxy mass function, hence to accurately model galaxies we also need to model the black holes. We present a comparison of two black hole growth models implemented within a large-scale, cosmological SPH simulation including star formation and feedback. One model is a modified Bondi-Hoyle prescription that grows black holes based on the smooth density of local gas, while the other is the recently proposed Accretion Disc Particle (ADP) method. This model swallows baryonic particles that pass within an accretion radius of the black hole and adds them to a subgrid accretion disc. Black holes are then grown by material from this disc. We find that both models can reproduce local scaling relations, although the ADP model is offset from the observed relations at high black hole masses. The total black hole mass density agrees between models to within a factor of three, but both struggle to reproduce the black hole mass function. The simulated mass functions are too steep and underestimate the number of intermediate and high mass black holes. In addition, the ADP model swallows excessive amounts of material at the resolution of large-scale, cosmological simulations producing unrealistically large accretion discs. Future work needs to be performed to improve the black hole mass function within simulations. This should be done through the mass growth and feedback as they are strongly coupled and should

not be treated as separate entities. This Chapter will be published in Muldrew *et al.* (in preparation).

4.1 Introduction

Supermassive Black Holes (SMBHs) are hosted at the centre of all galaxies with a stellar spheroid (Kormendy & Richstone, 1995; Ferrarese & Merritt, 2000) and play an important role in galaxy evolution. Without the feedback they power through Active Galactic Nuclei (AGN) it is difficult to reconcile the observed high mass end of the galaxy mass function with that predicted by galaxy formation models (Bower *et al.*, 2006; Croton *et al.*, 2006). In addition there is mounting evidence for the coevolution of galaxies and SMBHs through the SMBH Mass–Spheroid Velocity Dispersion relation ($M_{\rm BH}-\sigma$: Gebhardt *et al.*, 2000; Tremaine *et al.*, 2002) and the SMBH Mass–Bulge Stellar Mass relation ($M_{\rm BH}-M_{\rm Bulge}$: Magorrian *et al.*, 1998; McLure & Dunlop, 2002).

The exact mechanism for the formation of SMBHs remains uncertain, but there are three main theories that predict different seed masses. The first is that massive Population III stars collapse giving black hole seeds of $10^2-10^3\,{\rm M}_\odot$ (Madau & Rees, 2001); alternatively the collapse of atomically cooling $\sim 10^4\,{\rm K}$ primordial gas in dark matter haloes may lead to seed masses of $10^4-10^6\,{\rm M}_\odot$ (Bromm & Loeb, 2003). The third mechanism is that they may form from the collapse of $\sim 10^3\,{\rm M}_\odot$ stars created in runaway collisions in dense stellar clusters (Devecchi & Volonteri, 2009). Johnson *et al.* (2012) suggest that the lower limit on SMBH seeds is $\sim 10^5\,{\rm M}_\odot$ which requires significant rapid growth to produce SMBH of $2\times10^9\,{\rm M}_\odot$ at $z\sim7$ (Mortlock *et al.*, 2011) and $1.7\times10^{10}\,{\rm M}_\odot$ by the present day (van den Bosch *et al.*, 2012).

In the context of cosmological simulations, SMBH are initially many times smaller than the typical resolution of hydrodynamic particles (Schaye *et al.*, 2010; Di Matteo *et al.*, 2012) and the exact details of their physics is too poorly understood to simulate directly. This results in the formation, growth and feedback of SMBHs being added in a subgrid manner. Sink particles are used to represent the SMBH with a subgrid accretion scheme implemented (Springel, Di Matteo & Hernquist, 2005). The most

common accretion model used in the literature is the Bondi-Hoyle (Bondi & Hoyle, 1944; Bondi, 1952) method (e.g. Springel, Di Matteo & Hernquist, 2005; Di Matteo, Springel & Hernquist, 2005; Sijacki *et al.*, 2007; Di Matteo *et al.*, 2008, 2012; Vogelsberger *et al.*, 2013). Bondi-Hoyle models the accretion of a spherically symmetric uniform flow of zero angular momentum material captured gravitationally by a point source. This results in an accretion rate onto the SMBH, $\dot{M}_{\rm BH}$, that is proportional to the mass of the SMBH squared, the local density of the gas, ρ, and inversely proportional to the sound speed, $c_{\rm s}$, cubed, i.e. $\dot{M}_{\rm BH} \propto \dot{M}_{\rm Bondi} \propto M_{\rm BH}^2 \rho / c_{\rm s}^3$.

Although commonly used in simulations, the Bondi-Hoyle method has a number of limitations, as discussed in Hobbs *et al.* (2012). The principle assumption is that gas is at rest at infinity, but SMBHs are embedded within stellar bulges and dark matter haloes that are many times larger. If the gas within the halo is as hot as the virial temperature, then it will be in hydrostatic equilibrium and the Bondi-Hoyle method will apply. However, during periods of rapid growth of the SMBH, the halo is gas rich and dense gas is likely to cool faster. This will lead to the gas collapsing to the centre triggering star formation and feeding the SMBH. In this case, there is a net radial inflow towards the SMBH and so gas cannot be assumed to be at rest at infinity and violates the Bondi-Hoyle assumption.

Another assumption of Bondi-Hoyle is that the gas accretes onto the SMBH with zero angular momentum, which is known to be not true. As gas collapses onto the SMBH it will settle into a circular orbit forming an accretion disc, whose radius is set by the angular momentum of the gas relative to the SMBH. This angular momentum forms a natural barrier to accretion and only low angular momentum gas will be accreted onto the SMBH (King, 2010; Hobbs *et al.*, 2011). The gas can only lose angular momentum through collisions, creating a delay before gas can be accreted by the SMBH.

Alternative models for SMBH growth have been proposed to try and overcome these problems. Debuhr, Quataert & Ma (2011) introduced an accretion rate that was dependent on the angular momentum of the gas, building on the previous work of Hopkins & Quataert (2010). They set the accretion rate proportional to the mean gas surface density, $\Sigma_{\rm gas}$, the local sound speed squared and inversely proportional to the rotational angular frequency of the gas, Ω, i.e. $\dot{M}_{\rm BH} \propto \Sigma_{\rm gas} c_{\rm s}^2 / \Omega$. While this model accounts for

the angular momentum of the gas, it is still accreted onto the SMBH without a delay, such as it would experience in the accretion disc.

In an attempt to account for both the angular momentum and the delayed accretion Power, Nayakshin & King (2011, hereafter PNK11) proposed a two stage accretion disc particle model for black hole accretion. As opposed to approximating the accretion rate based on local gas properties, they defined an accretion radius around the black hole particle and any baryonic material passing inside this is swallowed and added to a subgrid accretion disc. Material is then allowed to accrete onto the SMBH from the accretion disc over a viscous timescale.

Currently the accretion disc particle model has only been used in idealised disc and major merger simulations (PNK11; Wurster & Thacker, 2013; Newton & Kay, 2013). In this Chapter we present the first implementation of this model in a cosmological, large-scale simulation including cooling, star formation and feedback. In Section 4.2 we describe our simulation and give detailed descriptions of the two black hole growth models we have implemented. In Section 4.3 we find the optimal parameters for the accretion disc particle model to reproduce the local black hole density and then compare it to a modified Bondi-Hoyle prescription through mass functions and local scaling relations. Finally in Section 4.4 we summarise our findings from comparing the two growth models and state their suitability to cosmological, large-scale simulations.

4.2 Methods

The simulations performed in this Chapter were carried out using a modified version of the N-body/SPH code GADGET-3 (last described in Springel, 2005). The code was modified to include star formation, supernova feedback, radiative cooling, chemodynamics, black hole accretion and AGN feedback. These were implemented as part of the OverWhelmingly Large Simulation project (OWLS; Schaye *et al.*, 2010) and are described fully in Booth & Schaye (2009, hereafter BS09) and summarised in Section 4.2.1. We adopted a flat Λ-Cold Dark Matter (ΛCDM) cosmology with parameters: $\{\Omega_m, \Omega_b, \Omega_\Lambda, \sigma_8, n_s, h\} = \{0.238, 0.0418, 0.762, 0.74, 0.951, 0.73\}$ as determined from the Wilkinson Microwave Anisotropy Probe 3-year results (WMAP-3;

Spergel *et al.*, 2007) and identical to that used by BS09.

The analysis performed in this Chapter was conducted on a simulation of a cubical volume of the Universe of side length $50\,h^{-1}\mathrm{Mpc}$ comoving, realised using 256^3 dark matter particles and 256^3 gas particles giving a dark matter particle mass of $4.06 \times 10^8\,h^{-1}\mathrm{M}_\odot$ and a gas particle mass of $8.64 \times 10^7\,h^{-1}\mathrm{M}_\odot$. The gravitational softening was set to be 0.04 times the mean comoving inter-particle separation down to $z = 2.91$, below which a fixed proper scale of $2\,h^{-1}\mathrm{kpc}$ was used. Initial conditions were generated at $z = 127$ using the Zel'dovich approximation to linearly evolve positions from an initially glass-like state. Haloes were found using SUBFIND (Springel *et al.*, 2001) which produces similar overall results to other halo finders (Chapter 2; Knebe *et al.*, 2011).

4.2.1 Physics Models

In addition to the standard SPH treatment, a number of subgrid models were introduced to represent various physical processes. A full description of these models can be found in BS09 and references therein, but a summary is given here.

Star formation within the simulation is governed by the method described in Schaye & Dalla Vecchia (2008). Due to the lack of resolution and physical understanding to simulate star formation directly, an effective equation of state is applied for densities $n_\mathrm{H} > n_\mathrm{H}^*$ where n_H is the hydrogen number density and $n_\mathrm{H}^* = 0.1\,\mathrm{cm}^{-3}$. The gas is then considered star forming and follows $P \propto \rho^\gamma$ with $\gamma = 4/3$ and normalised to $P/k = 10^3\,\mathrm{cm}^{-3}\,\mathrm{K}$ where P is the pressure and ρ is the density. The gas is then allowed to form stars at a pressure-dependent rate that reproduces the Schmidt-Kennicutt law (Kennicutt, 1998) renormalised to a Chabrier (2003) stellar initial mass function (IMF).

Supernovae feedback is then modelled kinetically following Dalla Vecchia & Schaye (2008), a variation on the model previously described in Springel & Hernquist (2003). Energy is injected locally by kicking gas particles into winds and is described by two parameters. The first is the initial mass-loading, $\eta = \dot{M}_\mathrm{w}/\dot{M}_*$, which is the ratio of the initial amount of gas put into the wind, $\dot{M}_\mathrm{w}$, compared with the local star formation

rate, $\dot{M}_*$, and the second is the wind velocity, $v_{\rm wind}$. Values of $\eta = 2$ and $v_{\rm wind} = 600\,{\rm km\,s^{-1}}$ were used in this work which corresponds to 40 percent of the total amount of supernova energy.

Radiative cooling was implemented following Wiersma, Schaye & Smith (2009). The timed release of 11 different elements (hydrogen, helium, carbon, nitrogen, oxygen, neon, magnesium, silicon, sulphur, calcium and iron) from massive stars (Type II supernovae and stellar winds) and intermediate-mass stars (Type Ia supernovae and asymptotic giant branch stars), assuming a Chabrier (2003) IMF in the range 0.1 to $100\,{\rm M}_\odot$, were followed using the method described in Wiersma *et al.* (2009). The net cooling rates were calculated element-by-element in the presence of the cosmic microwave background and a Haardt & Madau (2001) model for the UV/X-ray background radiation from quasars and galaxies. The contributions of the 11 elements were interpolated as a function of density, temperature and redshift from tables precomputed by CLOUDY (last described in Ferland *et al.*, 1998), assuming the gas to be optically thin and in (photo-)ionisation equilibrium.

4.2.2 Black Hole Models

The modelling of black holes within the simulation can be categorised into three sections: seeding, growth and feedback. As part of this investigation we have looked at two different growth models, that of BS09 (Section 4.2.2.1) and that of PNK11 (Section 4.2.2.2). Beyond this, the rest of the model has stayed the same to allow for a fair comparison.

Black holes were seeded, following the method of Sijacki *et al.* (2007), using a recursive Friends-of-Friends algorithm (FoF; Davis *et al.*, 1985) on the dark matter particles. FoF was run evenly in log expansion factor, a, such that $\Delta a = 0.02\,a$, which corresponds to $\sim 250\,{\rm Myr}$ ($\sim 70\,{\rm Myr}$) at redshift zero (three). Dark matter haloes found containing at least 100 particles ($M_{\rm halo,min} = 4.06 \times 10^{10}\,h^{-1}{\rm M}_\odot$) were seeded with a black hole sink particle (Springel, Di Matteo & Hernquist, 2005) if they did not already contain one. The most gravitationally bound baryonic particle in the halo is converted into a black hole particle with seed mass $10^{-3} M_{\rm gas}$ ($M_{\rm seed} = 8.64 \times 10^4\,h^{-1}{\rm M}_\odot$).

Black holes were then left to grow through accretion and mergers following either the BS09 or PNK11 model. In both cases the accretion rate was Eddington limited:

$$\dot{M}_{\rm Edd} = \frac{4\pi G M_{\rm BH} m_{\rm p}}{\epsilon_{\rm r} \sigma_{\rm T} c} \tag{4.1}$$

where G is the gravitational constant, $M_{\rm BH}$ is the SMBH mass, $m_{\rm p}$ is the proton mass, $\epsilon_{\rm r}$ is the radiative efficiency of a black hole (taken as 0.1 throughout; Shakura & Sunyaev, 1973), $\sigma_{\rm T}$ is the Thomson cross-section for the scattering of free electrons and c is the speed of light. Black holes are allowed to merge in both accretion models when they pass within a smoothing length, $h_{\rm BH}$, of each other and have a relative velocity smaller than the circular velocity at that distance ($v_{\rm rel} = \sqrt{GM_{\rm BH}/h_{\rm BH}}$).

Feedback from the SMBH is implemented thermally (rise in thermal energy), as opposed to kinetically (rise in kinetic energy) for supernova. This is the same as the BS09 feedback model, but different to PNK11. They adopted the model of Nayakshin, Cha & Hobbs (2009) where virtual particles are emitted by the SMBH in a Monte-Carlo fashion that interact directly with the SPH density field and deposit their momentum in a region dictated by the optical depth. The amount of energy released is independent of the environment and no attempt is made to separate the 'quasar mode' and 'radio mode' feedback. For each timestep, Δt, the amount of energy released is:

$$E_{\rm feed} = \epsilon_{\rm f} \epsilon_{\rm r} \dot{M}_{\rm BH} c^2 \Delta t \tag{4.2}$$

where $\epsilon_{\rm f}$ is the efficiency with which a black hole couples the radiated energy into its surroundings. A value of 0.15 is adopted to produce a good match with observations (BS09). To ensure that the feedback energy is not immediately radiated away, a minimum heating temperature is imposed and black holes only release energy when they have obtained enough to raise the temperature of $n_{\rm heat}$ particles by $\Delta T_{\rm min}$. This corresponds to:

$$E_{\rm crit} = \frac{n_{\rm heat} M_{\rm gas} k_{\rm B} \Delta T_{\rm min}}{(\gamma - 1) \mu m_{\rm H}} \tag{4.3}$$

where $k_{\rm B}$ is the Boltzmann constant, $\gamma = 4/3$, μ is the mean molecular weight (0.58 for a fully ionised gas of primordial composition) and $m_{\rm H}$ is the mass of Hydrogen.

BS09 found that adopting $\Delta T_{\rm min} = 10^8\,{\rm K}$ and $n_{\rm heat} = 1$ was sufficient to balance the change in temperature being too small and the timescale between heating being too long. The energy released by the black hole is then equally distributed into a random fraction $n_{\rm heat}/N_{\rm ngb}$ of the black hole's neighbouring gas particles.

An additional change is made to star forming particles receiving feedback energy. Particles undergoing star formation are constrained by an effective equation of state, following the Schaye & Dalla Vecchia (2008) model outlined in Section 4.2.1, but this is not suitable if they undergo strong heating from the black hole. Particles that are heated $0.5\,{\rm dex}$ above the equation of state in a single timestep are removed from the equation of state and are no longer considered star forming. If their temperature drops at a later time to less than $0.5\,{\rm dex}$ above the equation of state, they are returned to the equation of state and are considered star forming once more.

4.2.2.1 Modified Bondi-Hoyle (BS09)

The BS09 model for black hole growth uses a modified Bondi-Hoyle (Bondi & Hoyle, 1944; Bondi, 1952) prescription to describe the accretion onto black holes that builds upon Springel, Di Matteo & Hernquist (2005). Initially black holes are seeded as described in Section 4.2.2. The new black hole particle has a SMBH mass corresponding to the seed mass, but the particle mass used in the gravity calculations remains the same as the total mass of the baryonic particle before conversion. The accretion rate is then calculated as:

$$\dot{M}_{\rm acc} = \alpha \frac{4\pi G^2 M_{\rm BH}^2 \rho}{(c_{\rm s}^2 + v^2)^{3/2}} \tag{4.4}$$

where $c_{\rm s}$ and ρ are the sound speed and gas density of the local medium, v is the velocity of the black hole relative to the ambient medium and α is a dimensionless efficiency parameter given by:

$$\alpha = \begin{cases} 1 & \text{if } n_{\rm H} < n_{\rm H}^* \\ \left(\frac{n_{\rm H}}{n_{\rm H}^*}\right)^{\beta} & \text{otherwise} \end{cases} \tag{4.5}$$

where $\beta = 2$ (see BS09 for reasoning). In Springel, Di Matteo & Hernquist (2005),

and other works using that method, a value of $\alpha = 100$ is adopted. BS09 argue that for low-density gas such a boost is not justified, as Bondi-Hoyle can be accurately modelled, and so introduce a variable α that does not increase the number of free parameters. The accretion rate is Eddington limited meaning that it cannot exceed that given by Equation 4.1. The accretion rate onto the black hole is then given by:

$$\dot{M}_{\rm BH} = \dot{M}_{\rm acc}(1 - \epsilon_{\rm r}) \tag{4.6}$$

To account for the accreted mass onto the SMBH, baryonic particles are stochastically swallowed by the black hole particle with probability:

$$p_i = \begin{cases} (M_{\rm BH} - M_{\rm part})\rho^{-1}W(r_{\rm BH} - r_i, h_{\rm BH}) & \text{if } M_{\rm BH} > M_{\rm part} \\ 0 & \text{otherwise} \end{cases} \tag{4.7}$$

where $W(r_{\rm BH} - r_i, h_{\rm BH})$ is the SPH kernel evaluated between the black hole and gas particle i. The baryonic particle mass is added to the the black hole particle mass, but no change is made to the SMBH mass.

4.2.2.2 Accretion Disc Particle (PNK11)

The Accretion Disc Particle (ADP) model of PNK11 relies on two free parameters to control the accretion onto the black hole. An accretion radius, $R_{\rm acc}$, around the black hole particle is defined and any baryonic particle that crosses within it is swallowed and added to an accretion disc. The SMBH then accretes the disc mass over a viscous timescale, $t_{\rm visc}$, giving an accretion rate of:

$$\dot{M}_{\rm BH} = \min\left(\frac{M_{\rm disc}}{t_{\rm visc}}, \dot{M}_{\rm Edd}\right) \tag{4.8}$$

where $M_{\rm disc}$ is the mass in the accretion disc. The overall black hole particle mass is then given by:

$$M_{\rm part} = M_{\rm BH} + M_{\rm disc} \tag{4.9}$$

Initially, when seeded, the SMBH is assigned the seed mass and the total baryonic mass minus the SMBH seed is assigned to the accretion disc. This leaves the total mass of the black hole particle the same as the baryonic particle it was seeded from.

Although designed to be a subgrid model representing a SMBH and its tightly bound accretion disc, it will be shown in Section 4.3 that for cosmological simulations the accretion discs produced are too massive to be physical. Therefore, from here on in we will avoid referring to this model as ADP.

4.3 Results

The PNK11 model of black hole growth works using two free parameters, the accretion radius, $R_{\rm acc}$, and the viscous timescale, $t_{\rm visc}$. To accurately model the growth, these parameters need to be set within the model to reproduce the $z = 0$ black hole mass density as closely as possible. In PNK11 it is suggested that the accretion radius should be set to the smallest resolvable scale of the simulation, of the order the gravitational softening, and the viscous timescale should satisfy $t_{\rm visc} > t_{\rm dyn}(R_{\rm acc})$ where $t_{\rm dyn}(R_{\rm acc})$ is the dynamical time at the accretion radius. Using these values as an initial starting point, Figure 4.1 shows the $z = 0$ black hole mass function for various values of the accretion radius with a fixed viscous timescale (left panel) and various values of viscous timescale with a fixed accretion radius (right panel). The mass function from BS09 is also shown as an illustration.

It is immediately apparent that an accretion radius of the order the gravitation softening ($2\,h^{-1}{\rm kpc}$) is much too large in low resolution cosmological volumes. This results in a large number of baryonic particles being swallowed, producing overly massive black holes. This also affects the number of black holes at a given mass, with too many being produced at all values. This is caused by strong feedback which is triggered by the amount of energy released being related to the accretion rate (Equation 4.2). For the large number of baryonic particles swallowed, the black hole accretion rate is very high causing large amounts of energy to be released disrupting the structures. Decreasing the accretion radius by factors of ten shows convergence for values of $20\,h^{-1}{\rm pc}$ (10^{-2} of the gravitational softening) or less. Within this distance all baryonic particles are

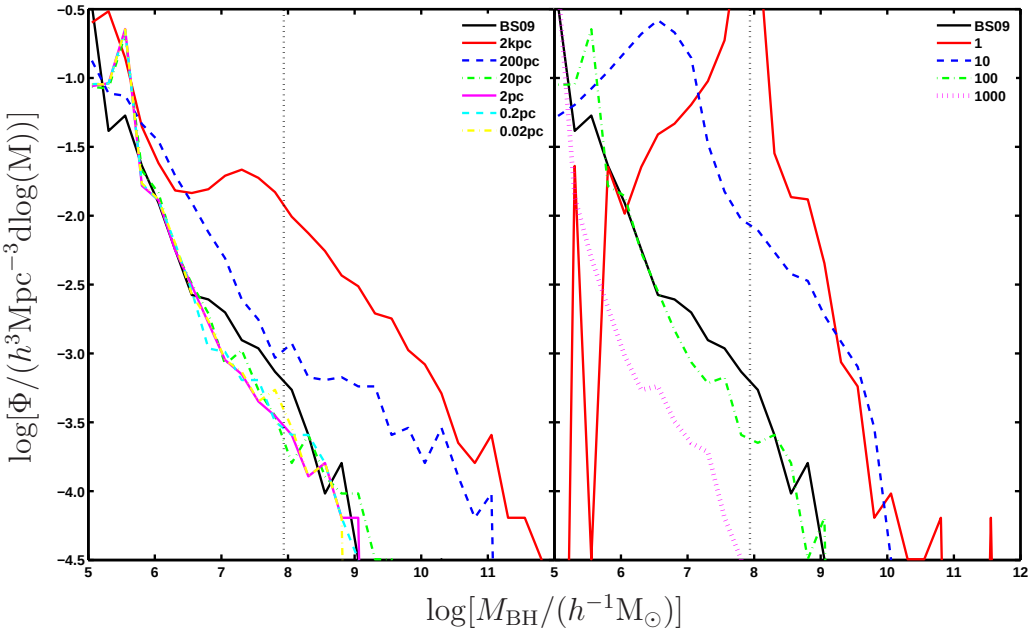

Figure 4.1: A study of the two free parameters in the PNK11 model. Left: Starting with the accretion radius equal to the gravitational softening and then decreasing by factors of ten for a fixed viscous timescale of $100\,t_{\mathrm{dyn}}$. Right: Starting with the viscous timescale equal to the dynamical time and then increasing by factors of ten for a fixed accretion radius of $2\,\mathrm{pc}$. The black solid line in both panels corresponds to the BS09 model, while the vertical black dotted line is the mass of a single gas particle.

accreted by the black hole, regardless of the accretion radius size.

Adopting a value of $2\,h^{-1}\mathrm{pc}$, which is of the order the physical value used in PNK11 and within the converged values, we then vary the viscous timescale. Initially a value equal to the dynamical time at the gravitational softening radius is used. This radius is larger than the accretion radius. Using such a short viscous timescale causes very rapid accretion that not only produces too massive and too many black holes as seen for large accretion radii, but also produces the wrong shape to the distribution. Increasing the viscous timescale to 100 times this value produces a black hole mass function similar to BS09 while continuing to increase it produces black holes that are not massive enough.

From studying the two free parameters of the PNK11 model, values of $R_{\mathrm{acc}} = 2\,h^{-1}\mathrm{pc}$ and $t_{\mathrm{visc}} = 100\,t_{\mathrm{dyn}}(R_{\mathrm{soft}})$ give the closest black hole mass function to the BS09 model at $z = 0$, which was modelled to reproduce the local black hole mass density. These two mass functions are plotted in Figure 4.2 along with the observed uncertainty based on the different methods used to measure it (Shankar, Weinberg & Miralda-Escudé, 2009; Kelly & Merloni, 2012). Attempting to measure the mass function observationally is an indirect process. The mass is inferred through relations with velocity dispersion, stellar mass and spheroid luminosity, and using these different methods leads to the scatter represented by the grey band. In addition to these, the fundamental plane and Sérsic index can also be used to measure black hole mass, but these methods underestimate the low mass end relative to the other methods (Shankar, Weinberg & Miralda-Escudé, 2009). Both models fail to reproduce the observed mass function, underestimating the number of black holes at masses greater than $\log[M_{\mathrm{BH}}/(h^{-1}\mathrm{M}_{\odot})] \sim 6.5$. Below masses of $\log[M_{\mathrm{BH}}/(h^{-1}\mathrm{M}_{\odot})] \sim 6.0$ the simulated mass functions continue to rise down to the seed mass, but observational data from Shankar, Weinberg & Miralda-Escudé (2009) is not available in this range. Assuming that the mass function stays flat, this would suggest an over production of black holes in this mass range. Overall the two simulated mass functions do not follow the expected Schechter function shape and are much more linear. It should be noted that the adopted value of σ_8 is lower in the simulations compared with current observations (Planck Collaboration, 2013). However, this should not effect the shape of the mass function, just the position, and it will be shown in Figure 4.6 that, despite this, there is no disagreement in the position of the

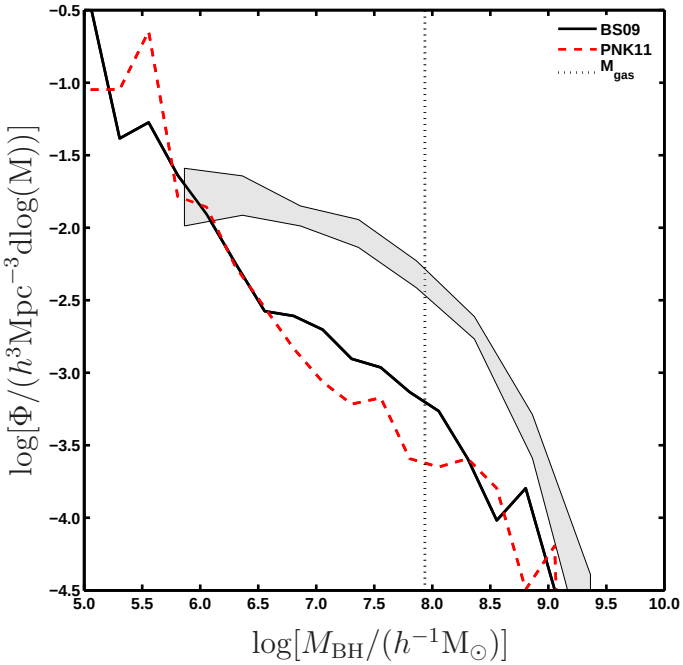

Figure 4.2: $z = 0$ black hole mass function for BS09 (black solid line) and PNK11 (red dashed line) using the best fit parameters from Figure 4.1. The shaded region represents the observed mass function taking into account uncertainty from the different methods used to measure it (Shankar, Weinberg & Miralda-Escudé, 2009; Kelly & Merloni, 2012). The vertical black dotted line is the mass of a single gas particle. Both models produce mass function that are too steep and do not tend to follow the Schechter function shape.

high mass end of the galaxy stellar mass function.

One of the most difficult problems to overcome in modelling black hole growth in simulations of cosmological volumes is that of resolution. In Figures 4.1 and 4.2 the vertical dotted line represents the mass of a single gas particle ($8.64 \times 10^7\, h^{-1}\mathrm{M}_\odot$). This is approximately three orders of magnitude larger than the seed mass of the black hole, while at the same time two orders of magnitude smaller than the observed largest SMBHs. Modelling such a large range of masses is a difficult task when the resolution is roughly in the centre of the mass range, especially for the PNK11 model. PNK11 was designed to relate the accretion rate more directly to the position of the baryonic particles as opposed to the smoothed density. This allows for periods of no accretion that is not possible in BS09. Seeding, let alone accretion, leads to an accretion disc that is massive relative to the SMBH giving a huge fuel supply. Only once the black holes have grown significantly do they become comparable in mass to the gas particles and these two stages are difficult to combine together.

As mentioned, at early times the accretion disc will be much larger than the SMBH and Figure 4.3 shows that this persists to $z = 0$ for all masses of black hole. The solid red line represents the 1:1 line which illustrates how much larger the accretion discs are. Accretion discs of this size would be unstable, as typically they should be significantly less massive than the black hole (Thompson, Quataert & Murray, 2005). Even adopting the two smaller accretion radii from Figure 4.1 does not change this result. Accreting gas particles that are three orders of magnitude larger than the seed black hole on a scale that is three orders of magnitude smaller than the gravitational softening leads to too much material being added and the viscous timescale dictating the growth, as opposed to the mass accretion.

A common test of black hole models is their ability to reproduce local scaling relations. Figure 4.4 shows the black hole mass–stellar velocity dispersion ($M_{\mathrm{BH}} - \sigma$) relation for BS09 (left panel) and PNK11 (right panel). The red line in each panel represents the best fit to the observational data from Tremaine *et al.* (2002), with the shaded region representing the uncertainty on this fit. The actual scatter in this relation is larger than the shaded region which just represents the range of lines that could be fitted. Black hole masses correspond to the total black hole mass of the halo as determined

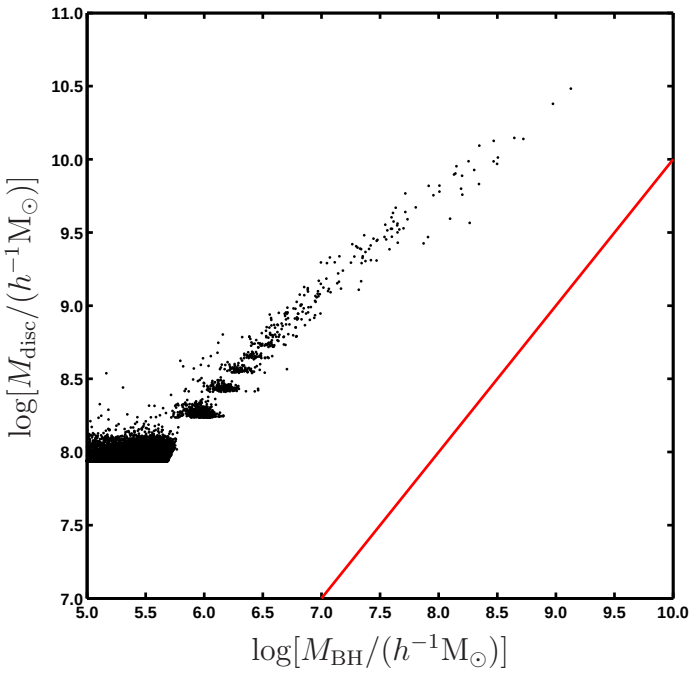

Figure 4.3: The accretion disc mass ($M_{\rm disc}$) against the black hole mass ($M_{\rm BH}$) for the PNK11 model. The red line denotes the 1:1 relation. Black holes in the PNK11 model have accretion discs that are significantly more massive than the black hole, which would lead to instabilities (Thompson, Quataert & Murray, 2005).

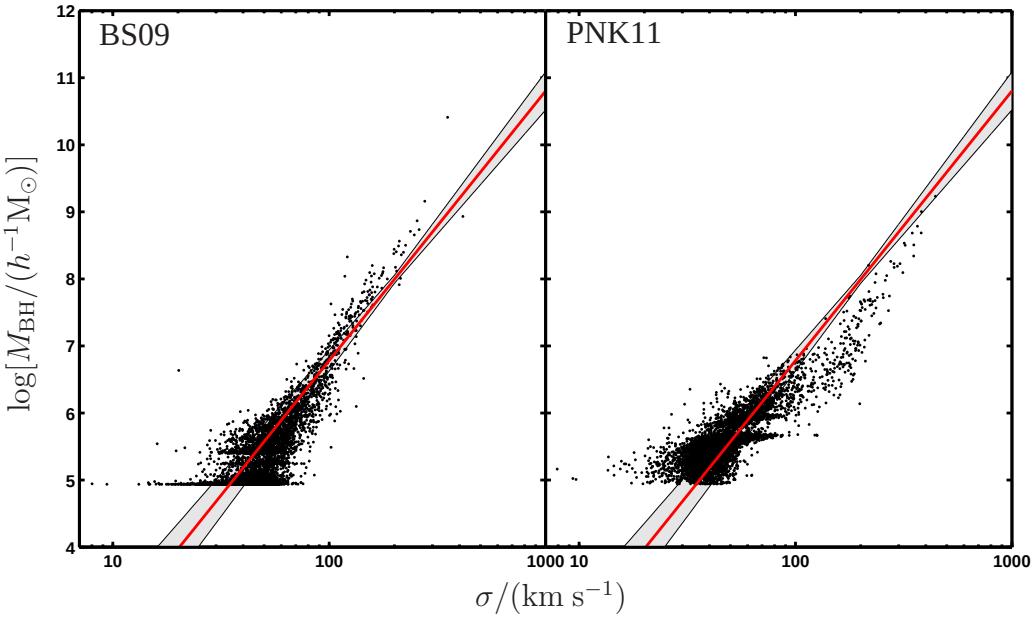

Figure 4.4: The $M_{\rm BH} - \sigma$ relation for BS09 (left) and PNK11 (right). The red line and shading represents the observed best fit and the uncertainty on this fit from Tremaine *et al.* (2002). This is different to the scatter on the data which is larger. BS09 is well fit by the observations, but PNK11 tends to produce larger velocity dispersions for high mass black holes.

by SUBFIND. BS09 reproduces the $M_{\rm BH} - \sigma$ relation well, although is marginally steeper than the observed relation. PNK11 fits the relation well for low mass black holes, but for higher masses follows a relation that is offset to higher values of σ.

Another well known scaling relation is that of black hole mass–stellar bulge mass. Marleau *et al.* (2012) argue that this relation is actually independent of morphology and is really a relation with total stellar mass ($M_{\rm BH} - M_*$). In Figure 4.5 we plot the $M_{\rm BH} - M_*$ relation for BS09 (left panel) and PNK11 (right panel). This is more accurate than comparisons with bulge mass, as the resolution of our simulations is too low to define bulges or morphology. The red line in each panel is the best fit to the observational data from Marleau *et al.* (2012) and, again, the shaded region is the uncertainty on this fit, with the scatter of the data being larger. In general BS09, while close to the relation, is slightly steeper than the observed data. At higher masses BS09 lies on the observed line, but for low mass black holes the stellar masses tend to be larger than expected. PNK11 better fits the data for low mass black holes, but still produces galaxies with a slightly higher stellar mass. For high mass black holes there is again an offset similar to Figure 4.4 with the galaxies having a higher stellar mass and following a linear relation.

To better understand the cause of these deviations in the $M_{\rm BH} - \sigma$ and $M_{\rm BH} - M_*$ relations, we plot the stellar mass function for the galaxies in Figure 4.6 and compare it to the observed stellar mass function from the Sloan Digital Sky Survey (SDSS; Yang, Mo & van den Bosch, 2009). For low mass galaxies the two stellar mass functions are the same, and this is expected as supernova feedback plays a dominant role in shaping the function in this range. At the high mass end, the PNK11 model produces much more massive galaxies than that of BS09 or that observed. This is in agreement with Figures 4.4 and 4.5 which show that galaxies with high mass black holes have higher than observed stellar masses and velocity dispersions. This is down to the feedback proving ineffective from these black holes. The amount of energy released by the black hole is related to the accretion rate (Equation 4.2) and demonstrates that the accretion rates in PNK11 are lower than those of BS09. A secondary effect that might weaken the feedback is that the energy released is placed into the neighbours of the black hole particle, which are the closest particles to the black hole and are at risk of accretion.

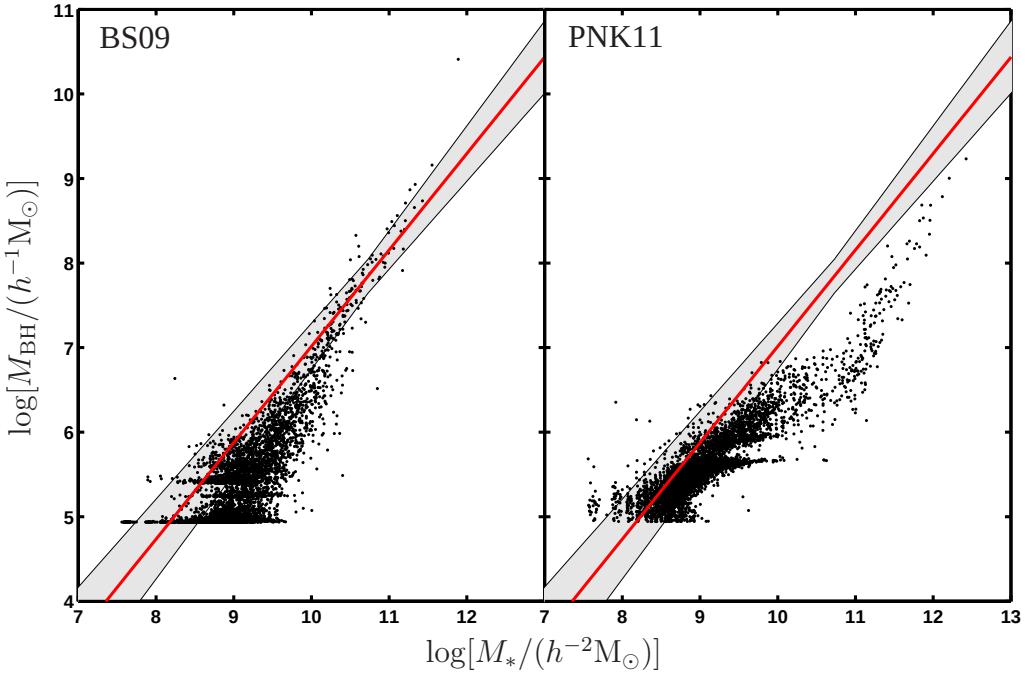

Figure 4.5: The $M_{\rm BH} - M_*$ relation for BS09 (left) and PNK11 (right). The red line and shading represents the observed best fit and the uncertainty on this fit from Marleau *et al.* (2012). This is different to the scatter on the data which is larger. BS09 is well fit by the observations, but tends to produce higher stellar mass galaxies for low mass black holes. PNK11 tends to produce larger stellar mass galaxies for high mass black holes.

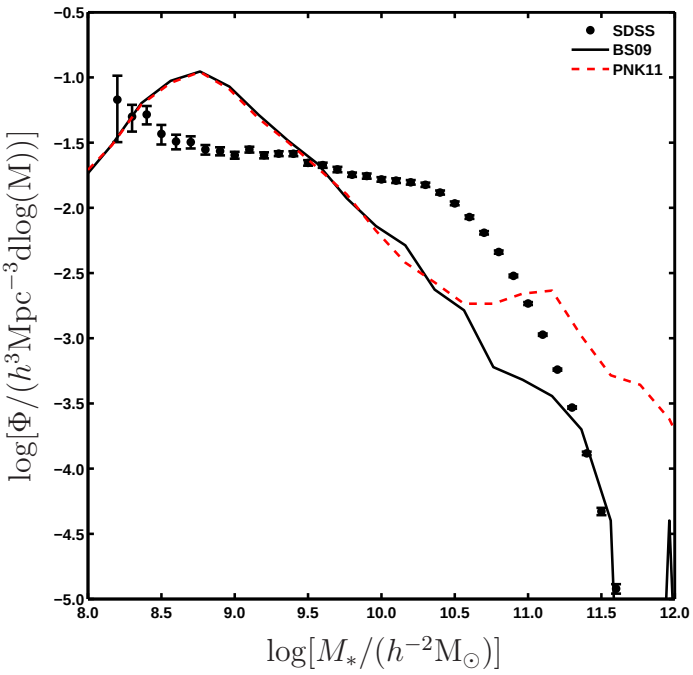

Figure 4.6: $z = 0$ stellar mass function for BS09 (black solid line) and PNK11 (red dashed line). Points correspond to the SDSS mass function from Yang, Mo & van den Bosch (2009). PNK11 has a lower black hole accretion rate to BS09, which weakens the feedback leading to high mass galaxies becoming too massive.

Finally we consider the evolution of the black hole mass density in Figure 4.7. The grey band represents the observed $z = 0$ density from Shankar, Weinberg & Miralda-Escudé (2009) and BS09 slightly overestimates this value. The model of PNK11 produces a density that is a factor of three smaller than BS09 at $z = 0$ and also outside the observed value. Overall, PNK11 has a smooth evolution of the density with redshift. BS09 has a less smooth distribution and grows in three stages. Firstly there is a smooth growth that is steeper than PNK11, before a sudden rapid phase that then flattens out. This period of small change in the density at low redshift is consistent with downsizing. Although the mass functions looked similar in Figure 4.2, the density appears very different. This is down to the growth of one very massive black hole ($2.47 \times 10^{10}\, h^{-1}\mathrm{M}_{\odot}$ at $z = 0$) that is not present for the PNK11 model, and is disconnected by over an order of magnitude from the second largest and so is not shown in Figure 4.2. Subtracting this black hole from the volume and recalculating the density yields a smoother evolution that agrees with PNK11 at $z = 0$. The steeper growth in BS09 before flattening means that the accretion rates will be higher at high redshift making feedback more effective in this regime compared with PNK11, preventing the over production of massive galaxies (Figure 4.6).

4.4 Summary and Conclusions

SMBHs are known to play an important role in galaxy evolution and a number of properties are strongly correlated with their mass. To produce the most realistic models of galaxies, the black hole growth also needs to be modelled accurately. We have implemented the PNK11 accretion disc model of black hole growth into a large-scale, cosmological simulation including star formation and feedback, and compared it with a modified Bondi-Hoyle model of BS09. Whereas BS09 relates the accretion rate to the local density and sound speed of the gas, $\dot{M}_{\mathrm{BH}} \propto \dot{M}_{\mathrm{Bondi}} \propto M_{\mathrm{BH}}^2 \rho / c_{\mathrm{s}}^3$, PNK11 uses two free parameters to govern accretion. Baryonic particles that pass within a given radius are swallowed by the black hole and added to a subgrid accretion disc. The black hole then accretes this material over a given timescale.

Setting these parameters is an important and non-trivial task to make sure that the $z = 0$

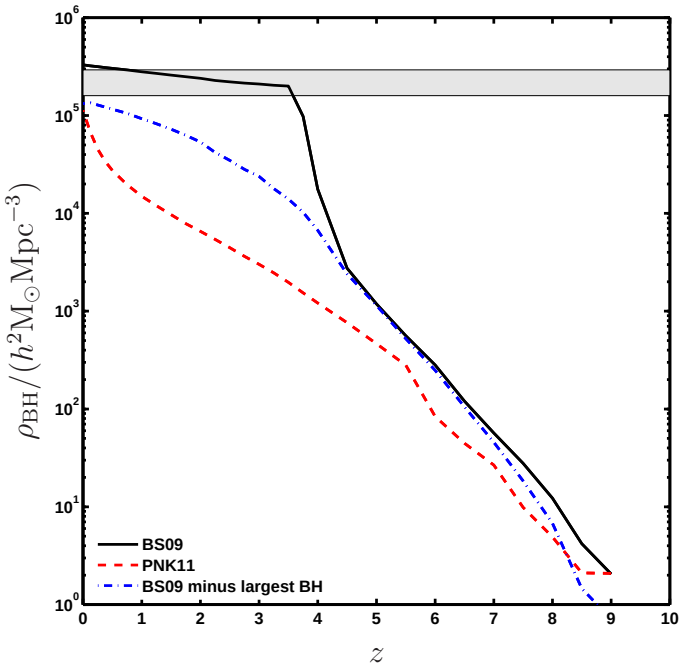

Figure 4.7: The evolution of the black hole mass density with redshift for BS09 (black solid line), PNK11 (red dashed line) and BS09 less the mass of the largest black hole in the volume (blue dot-dashed line). The shaded region corresponds to the observed black hole mass density at $z = 0$ from Shankar, Weinberg & Miralda-Escudé (2009). The PNK11 model predicts a smooth growth in the black hole mass density, while BS09 undergoes three different regimes dominated by the growth of the largest black hole in the volume. Subtracting this yields a smoother growth distribution steeper than PNK11.

black hole masses reflect those observed. Taking the accretion radius to be equal to the gravitational softening, the smallest resolvable scale, produces black holes that are too massive by the present day. This is down to the low resolution large-scale, cosmological simulations are currently run at, due to the limitations of computing power. Below 0.01 times the gravitational softening, the mass functions converge on the same value. This result is unexpected, as decreasing the radius further would naïvely suggest less material would be accreted. Beneath the gravitational softening there is a radius at which all particles will be accreted by the black hole particle. The conclusions from this is that the accretion radius must be set to a physical size as opposed to relating it to properties of the simulation. A value of a few parsec is consistent with PNK11, Wurster & Thacker (2013) and this work.

The viscous timescale is a harder parameter to set, as every change in its value produces a different result. Here we have modified it from previous studies by introducing a black hole mass dependence through the dynamical time. Other works have stuck to a fixed value. While the viscous timescale is designed to delay accretion onto the black hole, in this work it has principally been used to buffer the excessive accretion. One of the advantages of the PNK11 model is that it includes a subgrid accretion disc, but these are too massive to be realistic even for the smallest accretion radii. The excessive accretion observed has been prevented from reaching the black hole by using very long viscous timescales.

Within this Chapter we have implemented the model of PNK11 in its simplest form, but further extensions are required for the current resolution of cosmological simulations. Accretion discs of the scale produced here would fragment leading to star formation, which in turn would lead to further feedback. This would affect the amount of material available to the black hole, lowering the accretion rate. Efforts have been made by Newton & Kay (2013) to improve the subgrid modelling of PNK11 by adding a two stage process. They accrete gas on the scale of the gravitational softening, but then delay its addition to the accretion disc representing the subgrid behaviour between the gravitational softening and the black hole accretion radius. The primary advantage of using the PNK11 model is that accretion is measured directly as opposed to being approximated as in the Bondi-Hoyle model. One possible route to improving the PNK11

model in cosmological simulations is to study the model using high resolution zooms where it has been shown to be effective. By measuring the accretion at high resolution, using a physically motivated model, an improved subgrid model for low resolution runs can be developed.

Common tests to check the effectiveness of black hole models include comparing with the local mass density and local scaling relations, such as black hole mass–stellar velocity dispersion, $M_{\rm BH} - \sigma$, and black hole mass–total stellar mass, $M_{\rm BH} - M_*$. Both models came close to reproducing these, with only small deviations at the high mass end related to ineffective feedback in the case of PNK11. For the local black hole density, PNK11 produces a value that is three times smaller than BS09, although for BS09 the total mass is dominated by one very massive black hole ($> 10^{10}\,h^{-1}\mathrm{M}_{\odot}$). Removing this produces a density similar to PNK11. Testing black hole models against these relations can be misleading, as deviations from these can be small compared with observational scatter and reproducing these relations does not guarantee that the right mass distribution of black holes is being produced.

An additional test of black hole mass models is to compare with the black hole mass function. This has been measured in a number of different ways observationally and the uncertainty on it is now well constrained. Although both models produce mass functions that are similar to each other, and reproduce scaling relations, neither agree with the observed values. The modelled mass functions do not follow the Schechter function shape, producing steep lines that overestimate the number of black holes at the low mass end, while underestimating the intermediate and high mass end. Booth & Schaye (2010) demonstrate that $M_{\rm BH} \propto \epsilon_{\rm f}^{-1}$, which means decreasing $\epsilon_{\rm f}$ will increase the masses of the black holes. However, making this change also affects the $M_{\rm BH} - \sigma$ relation, altering the normalisation, and so no longer agrees with observations. Changing the value of $\epsilon_{\rm f}$ also does not improve the shape of the black hole mass function. The continued rise at low masses may be the result of seeding model, leading to black holes tracing the dark matter halo mass function closer than the galaxy stellar mass function. Meanwhile the deficit shown at intermediate masses may correspond to the same deficit shown in the galaxy stellar mass function (Figure 4.6). Further work is needed on black hole modelling to address this discrepancy to make sure that the dis-

tribution is correct, which in turn will help improve the galaxy stellar mass function.

The most important function of black holes in galaxy formation simulations is the feedback they provide to prevent the formation of overly massive galaxies. Using the same thermal feedback model of BS09 on PNK11 proves ineffective and the black holes cannot prevent this happening. Combining this with the large amount of material that is swallowed into the accretion disc suggests that a stronger feedback mechanism is need. A kinetic regime has the advantage of being able to drive gas particles away from the black hole, preventing this over accretion and may reduce the risk of a particle that receives feedback energy being accreted. In future work we will look to implement this, as it is apparent that the growth of the black hole and the feedback are strongly coupled and should be treated as one process. Ideally, a better physical understanding of how the feedback energy from the black hole couples with the surrounding gas needs to be determined in order to improve the implementation within models.

The ability to reproduce local scaling relations has been used to show the success of black hole modelling, but recently van den Bosch *et al.* (2012) have presented a number of galaxies that do not obey these, containing very massive black holes. One such example is NGC1277, which has a stellar mass of $1.2 \times 10^{11}\,\mathrm{M}_{\odot}$ and a black hole mass of $1.7 \times 10^{10}\,\mathrm{M}_{\odot}$. These galaxies are not constrained by environment and can be found in and out of clusters. Possible formation channels include some run away process that allows the black hole to accrete gas heavily at high redshift or the possible accretion of star clusters might accelerate growth. For the BS09 model, we have one case of a very massive black hole and another that is large for its stellar mass. Until the space density of these objects is better understood, it is unclear at the present time whether these objects fit in with our current models of black hole growth or whether further consideration is needed.

Chapter 5

Summary and Conclusions

In this Thesis I have presented three projects focused on investigating galaxy formation and evolution. In Chapter 2 I compared two halo finders, AHF and SUBFIND, by applying them to a set of mock idealised haloes. Using mock haloes guarantees a known result in what should be recovered, making it possible to constrain the limitations of each finder. This will have important consequences for the results of simulations. In Chapter 3 I coordinated the application of twenty galaxy environment measures to a well constrained mock galaxy catalogue. This allowed for the investigation of what environment measures actually recover with the aim of understanding why galaxy properties correlate with environment. Finally in Chapter 4 I implemented the Accretion Disc Particle (ADP) model of black hole growth in a large-scale hydrodynamic simulation including cooling, star formation and feedback. Feedback from the black hole is related to its accretion rate and has an important effect on galaxy properties and star formation rate. Implementing a different growth model changes the accretion rate resulting in a different feedback effect on the galaxy.

5.1 Discussion

From analysing mock subhaloes placed within a larger halo, it is clear that mass recovery has a strong radial dependence within the halo for SUBFIND, and to a lesser extent AHF. The origin of this relates to the subhalo being truncated by the background density of the halo. To some extent the validity of this result depends on the definition of a

subhalo being used. If one defines subhaloes as being merged versions of haloes, then the outer regions of the subhalo will have lower density than the halo and so the structures should not be truncated. However, if one defines subhaloes as being overdensities within a halo, then the low density outer regions of the subhalo are not overdense and so it is right to truncate. It is very important when comparing subhalo properties that are sensitive to edges that the definition is taken into account. SUBFIND subhaloes are defined as overdensities and so are on average the size of the tidal radius ($r_{\rm t}$; Springel *et al.*, 2008). This is the radius at which the differential tidal force of the background halo is equal to the gravitational attraction of the satellite (Tormen, Diaferio & Syer, 1998):

$$r_{\rm t} = \left(\frac{M_{\rm sub}}{[2 - {\rm dln}M/{\rm dln}r]M(<r)} \right)^{1/3} r \tag{5.1}$$

where $M_{\rm sub}$ is the subhalo mass and $M(<r)$ the mass of the main halo internal to the radial position of the subhalo, r. While subhaloes will be stripped to this radius, it is not an instantaneous process as shown through the dynamic subhalo examples in Chapter 2. Therefore this truncation can have an effect when investigating the amount of stripping that has occurred. This is shown in Figure 15 of Gao *et al.* (2004) where the recovered fraction of particles for a subhalo is shown with radius as evidence of stripping, but the results are the same as those presented here for the same sized subhalo at different radii. Any stripping beyond the tidal radius is not described by SUBFIND. For hydrodynamic simulations this truncation will not have a major impact as galaxies are embedded deep inside the subhalo and so are unlikely to be truncated. Alternative properties that characterise subhaloes more stably are the mass at infall and peak circular velocity. The mass at infall is still a quantity that needs some consideration, as truncation can start with SUBFIND at $1.5\,r_{\rm vir}$ which means the position that 'infall' happens needs to be careful chosen. The peak circular velocity is a very stable quantity as it occurs close to the centre of the subhalo and so is not affected by the truncation. This may prove a more reliable property to define the subhalo by. For Subhalo Abundance Matching (SHAM; see Section 1.2.5), matching subhaloes by circular velocity as opposed to mass offers the potential of yielding better matches by avoiding the effects of truncation as well as retaining the history of the subhaloes former mass.

The most commonly used method of determining galaxy environment is to estimate the local galaxy density. This is principally done either using n-th nearest neighbour, where the number of galaxies is fixed and the distance varies, or fixed aperture, where the distance is fixed and the number of galaxies varies. Using these two methods does not yield the same result. Both methods have a resolution limit, at small scales they can no longer describe the local environment. For n-th nearest neighbour this occurs when n or more neighbouring galaxies are outside the halo containing the galaxy in question. For fixed aperture this occurs when the halo is small enough to fit entirely in the aperture. Fixed apertures also exhibit a dependence on halo mass that is not seen using nearest neighbour-based methods. Galaxies in the densest environments tend to be the galaxies occupying the largest halo for fixed apertures, while they are the central galaxies for a range of halo masses using nearest neighbour. This leads to the conclusion that there is no universal environment measure, and the most suitable method depends on the scale being probed. 'Local environment', internal to a halo, is best measured using nearest neighbour as it is adaptable to the small scales, while 'large-scale environment', external to a halo, is best measured using fixed apertures as it is mass dependent and gives proximity to larger structures. Combining both measures offers the possibility of determining relations with halo mass, as galaxy properties that correlate stronger to fixed aperture environment than nearest neighbour environment are likely to be correlated with halo mass. Meanwhile environment measures may also be used to detect clusters, as the densest nearest neighbour measures give potential centres, while fixed aperture measures give a relative indication of mass.

Implementing the Accretion Disc Particle model (ADP) of Power, Nayakshin & King (2011, PNK11) for black hole growth in a large volume cosmological simulation is a difficult task. The primary difficulty is that the resolution of the simulation is too low to be implemented in the form described in PNK11. The baryonic particle mass is many times larger than the seed black hole mass, causing a huge amount of accretion to occur if only one particle is swallowed. In addition, the minimum resolvable scale, the gravitational softening, is much larger than a physically sensible accretion scale resulting in too much material being accreted. In order to produce realistic black hole masses, the accretion radius needs to be a sensible physical size of a few parsecs and the viscous timescale needs to be large enough to prevent the accreted material making

the black hole too massive. This is not a desirable criteria, as the accretion discs end up being too massive and the high viscous timescale just smooths out the accretion process over time. Overall the model of PNK11, in its existing form, offers no improvement over the current modified Bondi-Hoyle model of Booth & Schaye (2009) for large volume cosmological simulations. An outstanding issue with both models is that they fail to reproduce the observed black hole mass functions, despite matching the local scaling relations. The mass functions tend to underestimate the black hole masses and produce profiles that are too steep. This steepness may be a result of the seeding model, with the black hole mass function tracing the dark matter halo mass function.

5.2 Future Work

The most natural progression from the subhalo recovery work is to apply more halo finders to the mock haloes to test their ability to detect the subhaloes. This was done in Knebe *et al.* (2011) and it was found that SUBFIND and AHF span the range of results, with SUBFIND being one of the most conservative halo finders in mass assignment. This was further tested in Onions *et al.* (2012) using a 'live' halo as opposed to mocks. All the finders were applied to the Aquarius simulation (Springel *et al.*, 2008), a dark matter zoomed Milky Way-like halo, which confirmed the variation between finders in radial recovery. All these initial tests were focused on halo finding in dark matter only simulations, and so this naturally led onto hydrodynamic simulations including gas and stars. Knebe *et al.* (2013a) applied a range of finders to the SPH 'Constrained Local UniversE Simulation' (CLUES; Libeskind *et al.*, 2010) and found that the recovered gas content of haloes is much more varied than that of the dark matter or stars. With the added property of temperature, future work is needed to address how gas should be treated. In addition, current work on finding structure in hydrodynamic simulations has focused on SPH and so further investigation is needed for grid codes.

Following on from the galaxy environment project described in this Thesis, Skibba *et al.* (2013) constructed rank-ordered marked correlation functions to investigate environment clustering. Galaxies were weighted by their environment for different measures and this further confirmed that nearest neighbour methods tend to probe 'local

environment', while fixed apertures probe 'large-scale environment'. Further work using the environment measures described here was also carried out in Shattow *et al.* (submitted), but this time applied to a semi-analytic catalogue to investigate how proto-clusters evolve. They found that the densest environments at $z = 2$ do not correspond to the densest environments at $z = 0$. One area of observational uncertainty not taken into account in this work was that of holes and edges. Galaxy surveys will have a defined edge and not contain periodic boundaries like simulations. In addition there will be various masked regions where foreground stars have been removed creating holes. Some treatment is need to account for these regions when the environment is calculated. This can easily be studied using the HOD catalogue by adding masks and edges with the knowledge of what is underneath them. The environment measures, with their corrections, can then be reapplied and any bias investigated.

Two areas of future work on black hole modelling is modifying the PNK11 model and improving the black hole mass function. Instead of decreasing the accretion radius below the gravitational softening, as is done here and in Wurster & Thacker (2013), Newton & Kay (2013) propose having an additional stage in the model. They accrete particles at the gravitational softening and add them to their subgrid model. They then accrete these particles onto the accretion disc based on the free-fall time and then accrete onto the black hole from the accretion disc as described in PNK11. Adding this extra stage allows for the viscous timescale to remain low and not become a buffer to prevent over accretion. Implementing this model may solve some of the resolution issues, but as discussed in Newton & Kay (2013), a stronger feedback prescription will also be needed. Improving the black hole mass function comes down to two discrepancies, the alignment and shape. Booth & Schaye (2010) demonstrate that $M_{\rm BH} \propto \epsilon_{\rm f}^{-1}$ and so adopting a smaller value of $\epsilon_{\rm f}$ will increase the black hole mass. This may have other effects though on the normalisation of the scaling relations and so needs to be investigated. The steepness of the mass function may be a result of the tight relationship between black hole mass and dark matter halo mass, also discussed in Booth & Schaye (2010). This relation is implicitly built into the model as black holes are always seeded with the same mass in the same size halo. Varying the seeding mechanism may result in a mass function that traces the galaxy mass function better.

5.3 Conclusions

The principle conclusion of this Thesis is that definitions need to be carefully considered when comparing correlations in astronomy. Often terms, such as environment and mass, are simply plotted without consideration for how they are actually measured. As shown in this Thesis, different measures of galaxy environment yield different results, and so it is not sufficient enough to merely state a property correlates with environment. Depending how the environment is defined can conceal the true correlation. A similar issue arises in the definition of subhalo mass. Halo finders such as SUBFIND are very clear that they define subhaloes as overdensites, and so users should consider the truncation in their work. Careful consideration of definitions will allow for clearer comparisons and differentiate between numerical and physical effects.

With the many advances in numerical simulations within astronomy, the forefront of modelling today is the implementation of physical processes. Dark matter, at least for a cold dark matter Universe, is now well understood from an astronomical prospective, and simulations exist for microhaloes up to the super-large-scale structure. How the baryons behave within these structures remains uncertain, especially due to the number of physical processes, such as supernovae and Active Galactic Nuclei (AGN), that influence them. Within this Thesis I have investigated AGN by implementing a different growth mechanism for black holes. Traditionally N-body/SPH simulations have been refered to as 'direct' simulation, but with the increasing amount of subgrid physics the boundary with semi-analytics has been blurred. Ideally one would like to create subgrid models that are resolution independent, but as shown through the ADP model this is increasingly difficult. As resolution increases, limitations of models are exposed and increasing complexity is added. Our best hope of understanding the Universe is to increase our understanding of the physical processes that shape the baryons in galaxies, especially as it is the baryons that we observe.

Appendices

Appendix A

All Environment Measures

In Chapter 3 the trends with different galaxy environment measures are discussed and are grouped by n-th nearest neighbour and fixed aperture. Examples are given that illustrate the effect of increasing size for each measure. In this Appendix, for completeness, we repeat those figures including all the environment measures listed in Table 3.1. This further illustrates the results discussed there.

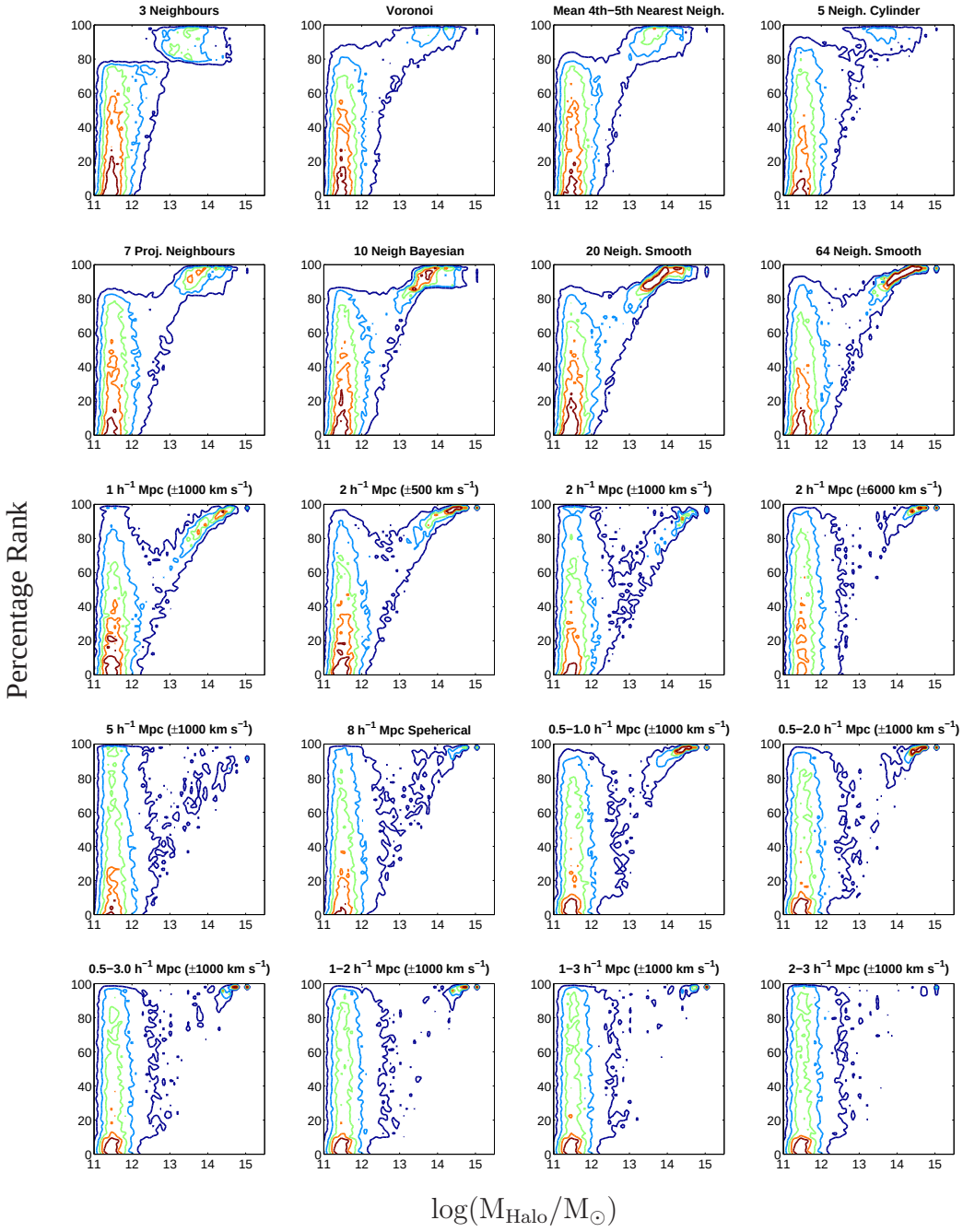

Figure A.1: The percentage rank of galaxy environment against dark matter halo mass, as in Figures 3.4 and 3.6, for all environment measures in Table 3.1. Contours are linearly spaced showing regions of constant galaxy number.

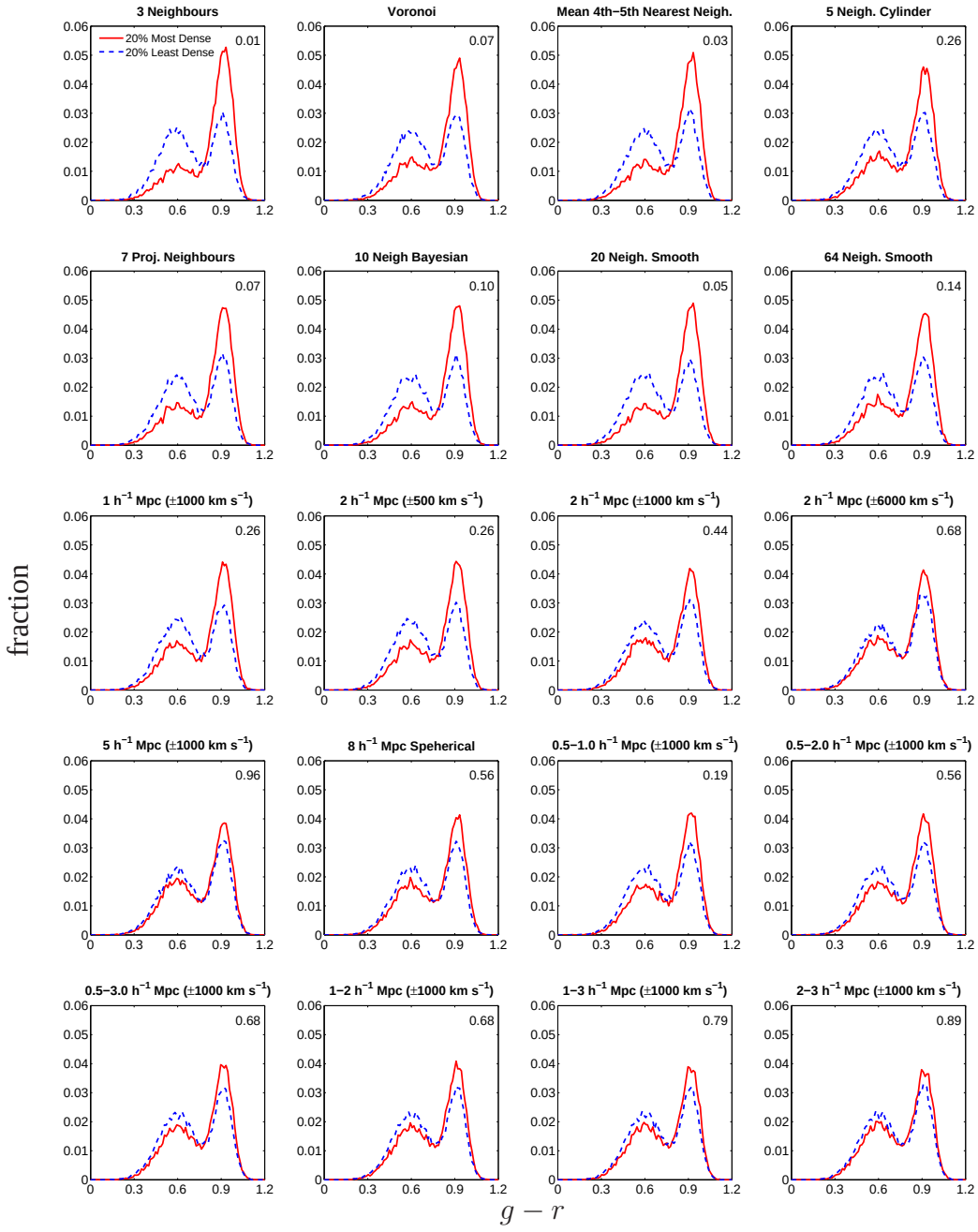

Figure A.2: Histograms of galaxy colour for the 20 percent most dense (red solid) and 20 percent least dense (blue dashed) galaxies, as in Figures 3.7 and 3.8, for all environment measures in Table 3.1. The number in the upper right of each panel is the Kolmogorov-Smirnov probability that both samples are drawn from the same distribution.

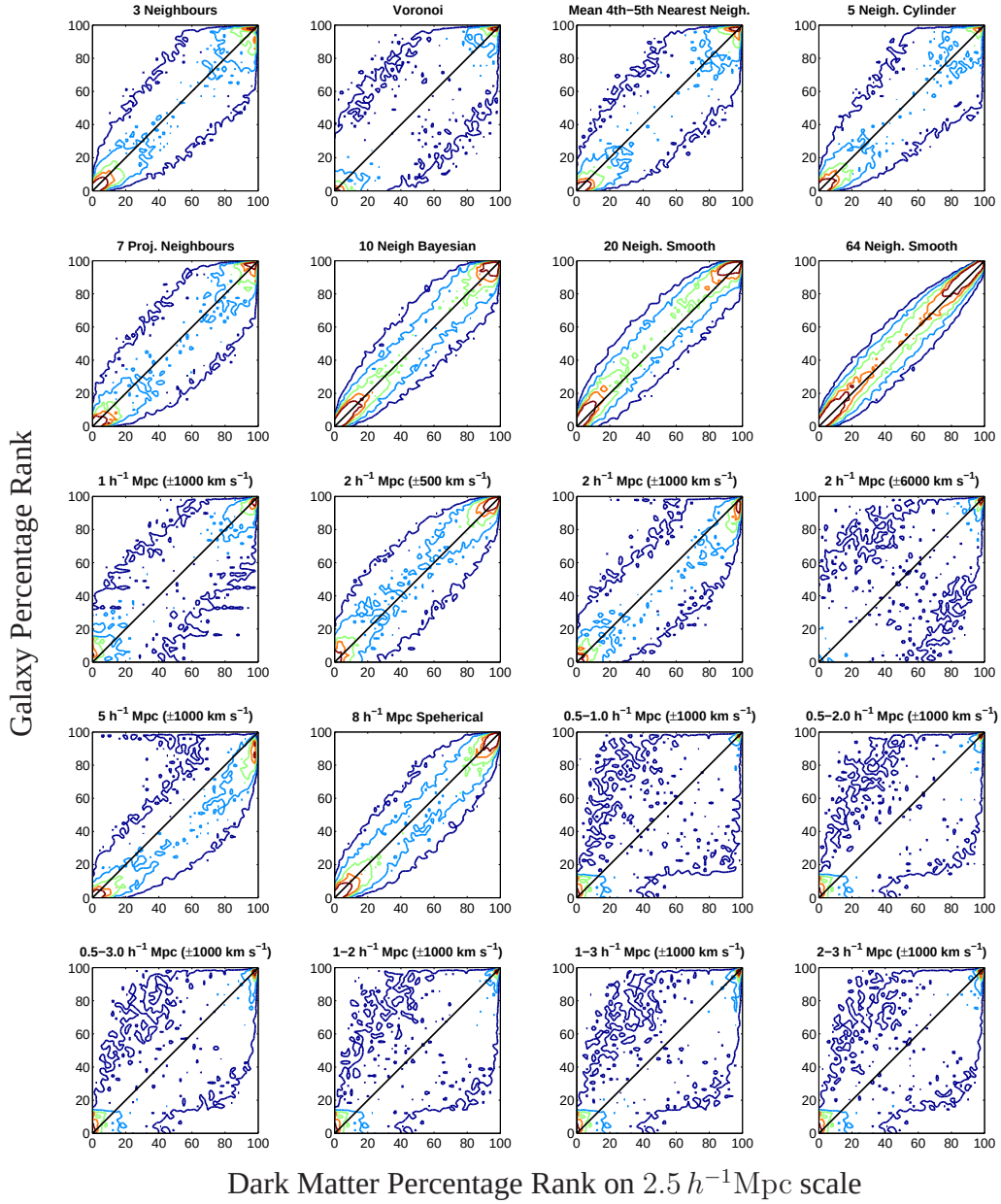

Figure A.3: The percentage rank of central galaxy environment using all environment measures in Table 3.1 plotted against the percentage rank of background dark matter environment measured using a smooth Gaussian filter of radius $2.5\,h^{-1}\mathrm{Mpc}$, as in the left panel of Figure 3.9. Contours are linearly spaced showing regions of constant galaxy number.

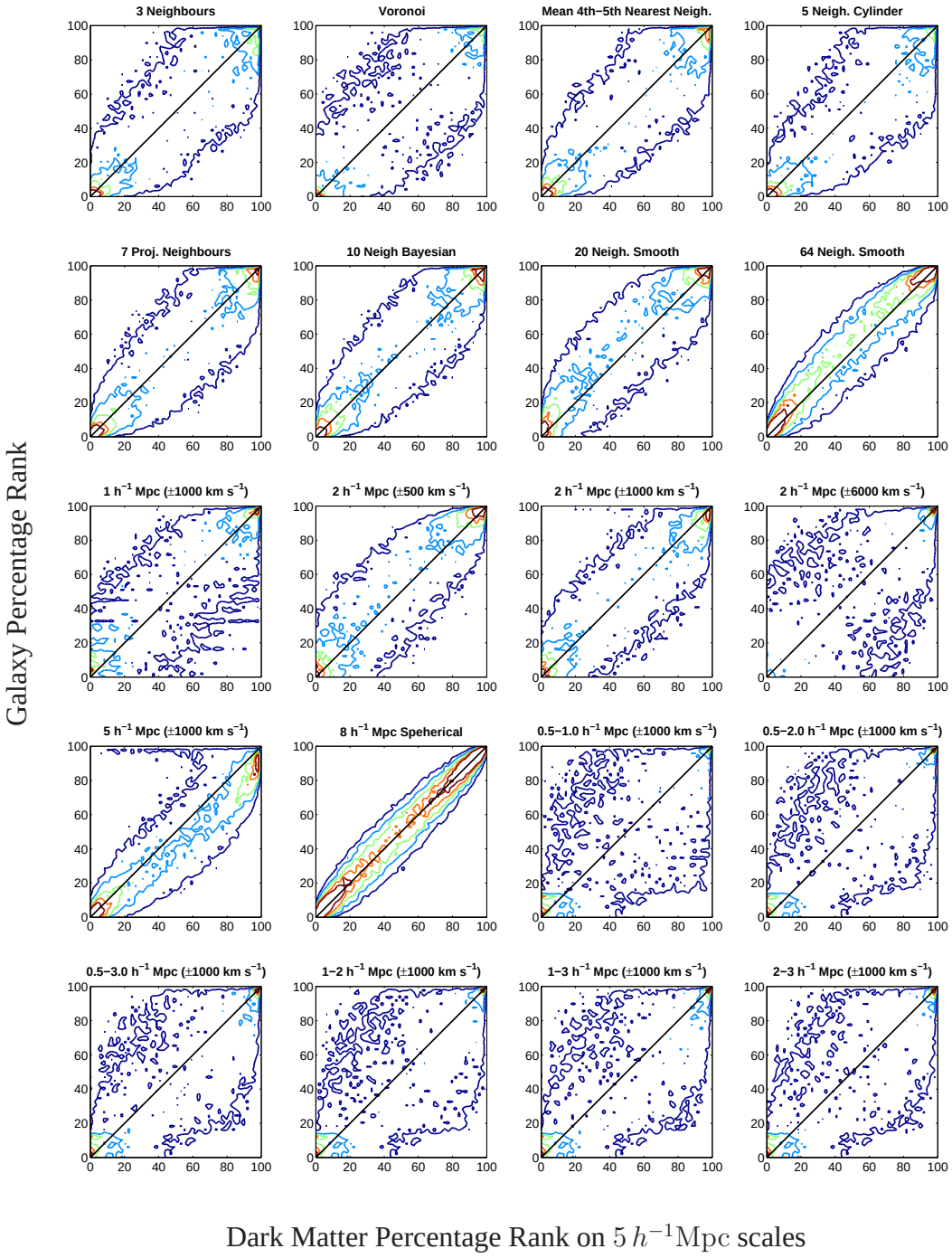

Figure A.4: The percentage rank of central galaxy environment using all environment measures in Table 3.1 plotted against the percentage rank of background dark matter environment measured using a smooth Gaussian filter of radius $5\,h^{-1}\mathrm{Mpc}$, as in the central panel of Figure 3.9. Contours are linearly spaced showing regions of constant galaxy number.

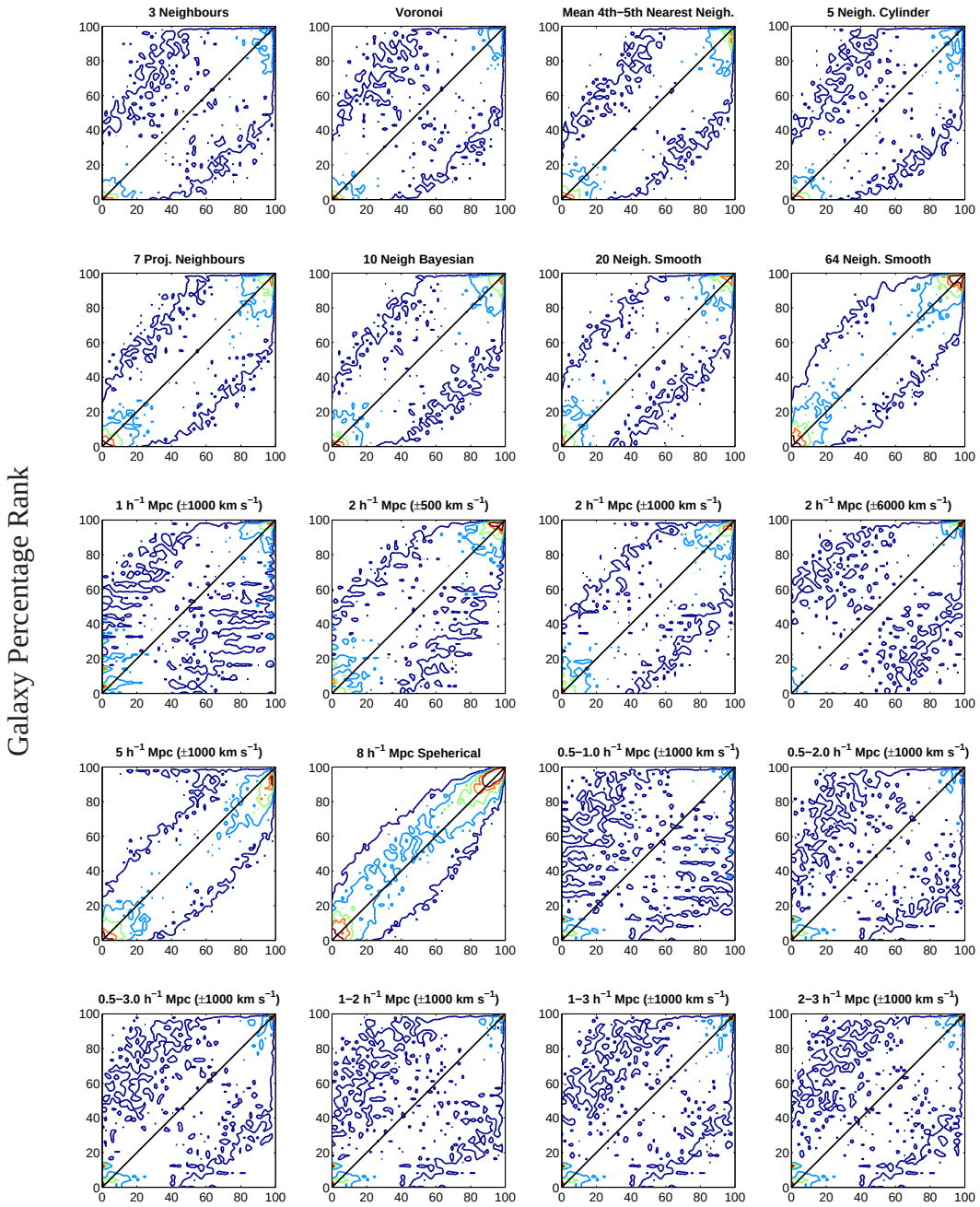

Figure A.5: The percentage rank of central galaxy environment using all environment measures in Table 3.1 plotted against the percentage rank of background dark matter environment measured using a smooth Gaussian filter of radius $10\,h^{-1}\mathrm{Mpc}$, as in the right panel of Figure 3.9. Contours are linearly spaced showing regions of constant galaxy number.

Bibliography

Aarseth S. J., 1963. MNRAS, **126**, 223. *Dynamical evolution of clusters of galaxies, I.*

Abbas U., Sheth R. K., 2006. MNRAS, **372**, 1749. *The environmental dependence of galaxy clustering in the Sloan Digital Sky Survey*.

Alimi J.-M., Bouillot V., Rasera Y., Reverdy V., Corasaniti P.-S., Balmes I., Requena S., Delaruelle X., Richet J.-N., 2012. *ArXiv e-prints, astro-ph/1206.2838. DEUS Full Observable ΛCDM Universe Simulation: the numerical challenge*.

Baldry I. K., Balogh M. L., Bower R. G., Glazebrook K., Nichol R. C., Bamford S. P., Budavari T., 2006. MNRAS, **373**, 469. *Galaxy bimodality versus stellar mass and environment*.

Ball N. M., Loveday J., Brunner R. J., 2008. MNRAS, **383**, 907. *Galaxy colour, morphology and environment in the Sloan Digital Sky Survey*.

Balogh M. L., McGee S. L., Wilman D., Bower R. G., Hau G., Morris S. L., Mulchaey J. S., Oemler, Jr. A., Parker L., Gwyn S., 2009. MNRAS, **398**, 754. *The colour of galaxies in distant groups*.

Bamford S. P., Nichol R. C., Baldry I. K., Land K., Lintott C. J., Schawinski K., Slosar A., Szalay A. S., Thomas D., Torki M., Andreescu D., Edmondson E. M., Miller C. J., Murray P., Raddick M. J., Vandenberg J., 2009. MNRAS, **393**, 1324. *Galaxy Zoo: the dependence of morphology and colour on environment*.

Barnes J., Hut P., 1986. Nature, **324**, 446. *A hierarchical O(N log N) force-calculation algorithm*.

Baugh C. M., 2006. *Reports on Progress in Physics*, **69**, 3101. *A primer on hierarchical galaxy formation: the semi-analytical approach*.

Benson A. J., Cole S., Frenk C. S., Baugh C. M., Lacey C. G., 2000. MNRAS, **311**, 793. *The nature of galaxy bias and clustering*.

Berlind A. A., Weinberg D. H., 2002. ApJ, **575**, 587. *The Halo Occupation Distribution: Toward an Empirical Determination of the Relation between Galaxies and Mass*.

Berlind A. A., Frieman J., Weinberg D. H., Blanton M. R., Warren M. S., Abazajian K., Scranton R., Hogg D. W., Scoccimarro R., Bahcall N. A., Brinkmann J., Gott,

III J. R., Kleinman S. J., Krzesinski J., Lee B. C., Miller C. J., Nitta A., Schneider D. P., Tucker D. L., Zehavi I., SDSS Collaboration, 2006. ApJS, **167**, 1. *Percolation Galaxy Groups and Clusters in the SDSS Redshift Survey: Identification, Catalogs, and the Multiplicity Function*.

Blanton M. R., Berlind A. A., 2007. ApJ, **664**, 791. *What Aspects of Galaxy Environment Matter?*

Blanton M. R., Hogg D. W., Bahcall N. A., Brinkmann J., Britton M., Connolly A. J., Csabai I., Fukugita M., Loveday J., Meiksin A., Munn J. A., Nichol R. C., Okamura S., Quinn T., Schneider D. P., Shimasaku K., Strauss M. A., Tegmark M., Vogeley M. S., Weinberg D. H., 2003. ApJ, **592**, 819. *The Galaxy Luminosity Function and Luminosity Density at Redshift z = 0.1*.

Blanton M. R., Eisenstein D., Hogg D. W., Schlegel D. J., Brinkmann J., 2005. ApJ, **629**, 143. *Relationship between Environment and the Broadband Optical Properties of Galaxies in the Sloan Digital Sky Survey*.

Bolzonella M., Kovač K., Pozzetti L., Zucca E., Cucciati O., Lilly S. J., Peng Y., Iovino A., Zamorani G., Vergani D., Tasca L. A. M., Lamareille F., Oesch P., Caputi K., Kampczyk P., Bardelli S., Maier C., Abbas U., Knobel C., Scodeggio M., Carollo C. M., Contini T., Kneib J.-P., Le Fèvre O., Mainieri V., Renzini A., Bongiorno A., Coppa G., de la Torre S., de Ravel L., Franzetti P., Garilli B., Le Borgne J.-F., Le Brun V., Mignoli M., Pelló R., Perez-Montero E., Ricciardelli E., Silverman J. D., Tanaka M., Tresse L., Bottini D., Cappi A., Cassata P., Cimatti A., Guzzo L., Koekemoer A. M., Leauthaud A., Maccagni D., Marinoni C., McCracken H. J., Memeo P., Meneux B., Porciani C., Scaramella R., Aussel H., Capak P., Halliday C., Ilbert O., Kartaltepe J., Salvato M., Sanders D., Scarlata C., Scoville N., Taniguchi Y., Thompson D., 2010. A&A, **524**, A76. *Tracking the impact of environment on the galaxy stellar mass function up to z ˜ 1 in the 10 k zCOSMOS sample*.

Bondi H., Hoyle F., 1944. MNRAS, **104**, 273. *On the mechanism of accretion by stars*.

Bondi H., 1952. MNRAS, **112**, 195. *On spherically symmetrical accretion*.

Booth C. M., Schaye J., 2009. MNRAS, **398**, 53. *Cosmological simulations of the growth of supermassive black holes and feedback from active galactic nuclei: method and tests **(BS09)***.

Booth C. M., Schaye J., 2010. MNRAS, **405**, L1. *Dark matter haloes determine the masses of supermassive black holes*.

Bower R. G., Benson A. J., Malbon R., Helly J. C., Frenk C. S., Baugh C. M., Cole S., Lacey C. G., 2006. MNRAS, **370**, 645. *Breaking the hierarchy of galaxy formation*.

Bower R. G., Vernon I., Goldstein M., Benson A. J., Lacey C. G., Baugh C. M., Cole S., Frenk C. S., 2010. MNRAS, **407**, 2017. *The parameter space of galaxy formation*.

Bromm V., Loeb A., 2003. ApJ, **596**, 34. *Formation of the First Supermassive Black Holes*.

Brough S., Hopkins A. M., Sharp R. G., Gunawardhana M., Wijesinghe D., Robotham A. S. G., Driver S. P., Baldry I. K., Bamford S. P., Liske J., Loveday J., Norberg P., Peacock J. A., Bland-Hawthorn J., Brown M. J. I., Cameron E., Croom S. M., Frenk C. S., Foster C., Hill D. T., Jones D. H., Kelvin L. S., Kuijken K., Nichol R. C., Parkinson H. R., Pimbblet K., Popescu C. C., Prescott M., Sutherland W. J., Taylor E., Thomas D., Tuffs R. J., van Kampen E., 2011. MNRAS, **413**, 1236. *Galaxy and Mass Assembly (GAMA): galaxies at the faint end of the Hα luminosity function*.

Bryan G. L., Norman M. L., 1998. ApJ, **495**, 80. *Statistical Properties of X-Ray Clusters: Analytic and Numerical Comparisons*.

Bullock J. S., Kolatt T. S., Sigad Y., Somerville R. S., Kravtsov A. V., Klypin A. A., Primack J. R., Dekel A., 2001. MNRAS, **321**, 559. *Profiles of dark haloes: evolution, scatter and environment*.

Cassata P., Guzzo L., Franceschini A., Scoville N., Capak P., Ellis R. S., Koekemoer A., McCracken H. J., Mobasher B., Renzini A., Ricciardelli E., Scodeggio M., Taniguchi Y., Thompson D., 2007. ApJS, **172**, 270. *The Cosmic Evolution Survey (COSMOS): The Morphological Content and Environmental Dependence of the Galaxy Color-Magnitude Relation at z ˜ 0.7*.

Chabrier G., 2003. PASP, **115**, 763. *Galactic Stellar and Substellar Initial Mass Function*.

Coil A. L., Newman J. A., Kaiser N., Davis M., Ma C.-P., Kocevski D. D., Koo D. C., 2004. ApJ, **617**, 765. *Evolution and Color Dependence of the Galaxy Angular Correlation Function: 350,000 Galaxies in 5 Square Degrees*.

Cole S., Lacey C. G., Baugh C. M., Frenk C. S., 2000. MNRAS, **319**, 168. *Hierarchical galaxy formation*.

Colless M., Dalton G., Maddox S., Sutherland W., Norberg P., Cole S., Bland-Hawthorn J., Bridges T., Cannon R., Collins C., Couch W., Cross N., Deeley K., De Propris R., Driver S. P., Efstathiou G., Ellis R. S., Frenk C. S., Glazebrook K., Jackson C., Lahav O., Lewis I., Lumsden S., Madgwick D., Peacock J. A., Peterson B. A., Price I., Seaborne M., Taylor K., 2001. MNRAS, **328**, 1039. *The 2dF Galaxy Redshift Survey: spectra and redshifts*.

Colless M., Peterson B. A., Jackson C., Peacock J. A., Cole S., Norberg P., Baldry I. K., Baugh C. M., Bland-Hawthorn J., Bridges T., Cannon R., Collins C., Couch W., Cross N., Dalton G., De Propris R., Driver S. P., Efstathiou G., Ellis R. S., Frenk C. S., Glazebrook K., Lahav O., Lewis I., Lumsden S., Maddox S., Madgwick D., Sutherland W., Taylor K., 2003. *ArXiv e-prints, astro-ph/0306581*. *The 2dF Galaxy Redshift Survey: Final Data Release*.

Conroy C., Wechsler R. H., Kravtsov A. V., 2006. ApJ, **647**, 201. *Modeling Luminosity-dependent Galaxy Clustering through Cosmic Time*.

Cooper M. C., Newman J. A., Madgwick D. S., Gerke B. F., Yan R., Davis M., 2005. ApJ, **634**, 833. *Measuring Galaxy Environments with Deep Redshift Surveys*.

Cooper M. C., Newman J. A., Croton D. J., Weiner B. J., Willmer C. N. A., Gerke B. F., Madgwick D. S., Faber S. M., Davis M., Coil A. L., Finkbeiner D. P., Guhathakurta P., Koo D. C., 2006. MNRAS, **370**, 198. *The DEEP2 Galaxy Redshift Survey: the relationship between galaxy properties and environment at z ˜ 1*.

Couchman H. M. P., Thomas P. A., Pearce F. R., 1995. ApJ, **452**, 797. *Hydra: an Adaptive-Mesh Implementation of P 3M-SPH*.

Cowan N. B., Ivezić Ž., 2008. ApJ, **674**, L13. *The Environment of Galaxies at Low Redshift*.

Croton D. J., Farrar G. R., Norberg P., Colless M., Peacock J. A., Baldry I. K., Baugh C. M., Bland-Hawthorn J., Bridges T., Cannon R., Cole S., Collins C., Couch W., Dalton G., De Propris R., Driver S. P., Efstathiou G., Ellis R. S., Frenk C. S., Glazebrook K., Jackson C., Lahav O., Lewis I., Lumsden S., Maddox S., Madgwick D., Peterson B. A., Sutherland W., Taylor K., 2005. MNRAS, **356**, 1155. *The 2dF Galaxy Redshift Survey: luminosity functions by density environment and galaxy type*.

Croton D. J., Springel V., White S. D. M., De Lucia G., Frenk C. S., Gao L., Jenkins A., Kauffmann G., Navarro J. F., Yoshida N., 2006. MNRAS, **365**, 11. *The many lives of active galactic nuclei: cooling flows, black holes and the luminosities and colours of galaxies*.

Dalla Vecchia C., Schaye J., 2008. MNRAS, **387**, 1431. *Simulating galactic outflows with kinetic supernova feedback*.

Davis M., Efstathiou G., Frenk C. S., White S. D. M., 1985. ApJ, **292**, 371. *The evolution of large-scale structure in a universe dominated by cold dark matter*.

de la Torre S., Le Fèvre O., Porciani C., Guzzo L., Meneux B., Abbas U., Tasca L., Carollo C. M., Contini T., Kneib J.-P., Lilly S. J., Mainieri V., Renzini A., Scodeggio M., Zamorani G., Bardelli S., Bolzonella M., Bongiorno A., Caputi K., Coppa G., Cucciati O., de Ravel L., Franzetti P., Garilli B., Halliday C., Iovino A., Kampczyk P., Knobel C., Koekemoer A. M., Kovač K., Lamareille F., Le Borgne J.-F., Le Brun V., Maier C., Mignoli M., Pelló R., Peng Y., Perez-Montero E., Ricciardelli E., Silverman J., Tanaka M., Tresse L., Vergani D., Zucca E., Bottini D., Cappi A., Cassata P., Cimatti A., Leauthaud A., Maccagni D., Marinoni C., McCracken H. J., Memeo P., Oesch P., Pozzetti L., Scaramella R., 2011. MNRAS, **412**, 825. *The zCOSMOS-Bright survey: the clustering of early and late galaxy morphological types since z ≃ 1*.

De Lucia G., Blaizot J., 2007. MNRAS, **375**, 2. *The hierarchical formation of the brightest cluster galaxies*.

Debuhr J., Quataert E., Ma C.-P., 2011. MNRAS, **412**, 1341. *The growth of massive black holes in galaxy merger simulations with feedback by radiation pressure*.

Dehnen W., Read J. I., 2011. *European Physical Journal Plus*, **126**, 55. *N-body simulations of gravitational dynamics*.

Devecchi B., Volonteri M., 2009. ApJ, **694**, 302. *Formation of the First Nuclear Clusters and Massive Black Holes at High Redshift*.

Di Matteo T., Colberg J., Springel V., Hernquist L., Sijacki D., 2008. ApJ, **676**, 33. *Direct Cosmological Simulations of the Growth of Black Holes and Galaxies*.

Di Matteo T., Khandai N., DeGraf C., Feng Y., Croft R. A. C., Lopez J., Springel V., 2012. ApJ, **745**, L29. *Cold Flows and the First Quasars*.

Di Matteo T., Springel V., Hernquist L., 2005. Nature, **433**, 604. *Energy input from quasars regulates the growth and activity of black holes and their host galaxies*.

Diemand J., Kuhlen M., Madau P., Zemp M., Moore B., Potter D., Stadel J., 2008. Nature, **454**, 735. *Clumps and streams in the local dark matter distribution*.

Diemand J., Kuhlen M., Madau P., 2007. ApJ, **657**, 262. *Dark Matter Substructure and Gamma-Ray Annihilation in the Milky Way Halo*.

Dressler A., 1980. ApJ, **236**, 351. *Galaxy morphology in rich clusters - Implications for the formation and evolution of galaxies*.

Driver S. P., Hill D. T., Kelvin L. S., Robotham A. S. G., Liske J., Norberg P., Baldry I. K., Bamford S. P., Hopkins A. M., Loveday J., Peacock J. A., Andrae E., Bland-Hawthorn J., Brough S., Brown M. J. I., Cameron E., Ching J. H. Y., Colless M., Conselice C. J., Croom S. M., Cross N. J. G., de Propris R., Dye S., Drinkwater M. J., Ellis S., Graham A. W., Grootes M. W., Gunawardhana M., Jones D. H., van Kampen E., Maraston C., Nichol R. C., Parkinson H. R., Phillipps S., Pimbblet K., Popescu C. C., Prescott M., Roseboom I. G., Sadler E. M., Sansom A. E., Sharp R. G., Smith D. J. B., Taylor E., Thomas D., Tuffs R. J., Wijesinghe D., Dunne L., Frenk C. S., Jarvis M. J., Madore B. F., Meyer M. J., Seibert M., Staveley-Smith L., Sutherland W. J., Warren S. J., 2011. MNRAS, **413**, 971. *Galaxy and Mass Assembly (GAMA): survey diagnostics and core data release*.

Efstathiou G., Eastwood J. W., 1981. MNRAS, **194**, 503. *On the clustering of particles in an expanding universe*.

Eke V. R., Cole S., Frenk C. S., 1996. MNRAS, **282**, 263. *Cluster evolution as a diagnostic for Omega*.

Eke V. R., Navarro J. F., Steinmetz M., 2001. ApJ, **554**, 114. *The Power Spectrum Dependence of Dark Matter Halo Concentrations*.

Elahi P. J., Han J., Lux H., Ascasibar Y., Behroozi P., Knebe A., Muldrew S. I., Onions J., Pearce F., 2013. *ArXiv e-prints, astro-ph/1305.2448. Streams Going Notts: The tidal debris finder comparison project*.

Elbaz D., Daddi E., Le Borgne D., Dickinson M., Alexander D. M., Chary R.-R., Starck J.-L., Brandt W. N., Kitzbichler M., MacDonald E., Nonino M., Popesso P., Stern D., Vanzella E., 2007. A&A, **468**, 33. *The reversal of the star formation-density relation in the distant universe*.

Ellison S. L., Simard L., Cowan N. B., Baldry I. K., Patton D. R., McConnachie A. W., 2009. MNRAS, **396**, 1257. *The mass-metallicity relation in galaxy clusters: the relative importance of cluster membership versus local environment*.

Ferland G. J., Korista K. T., Verner D. A., Ferguson J. W., Kingdon J. B., Verner E. M., 1998. PASP, **110**, 761. *CLOUDY 90: Numerical Simulation of Plasmas and Their Spectra*.

Ferrarese L., Merritt D., 2000. ApJ, **539**, L9. *A Fundamental Relation between Supermassive Black Holes and Their Host Galaxies*.

Font A. S., Bower R. G., McCarthy I. G., Benson A. J., Frenk C. S., Helly J. C., Lacey C. G., Baugh C. M., Cole S., 2008. MNRAS, **389**, 1619. *The colours of satellite galaxies in groups and clusters*.

Frenk C. S., White S. D. M., Bode P., Bond J. R., Bryan G. L., Cen R., Couchman H. M. P., Evrard A. E., Gnedin N., Jenkins A., Khokhlov A. M., Klypin A., Navarro J. F., Norman M. L., Ostriker J. P., Owen J. M., Pearce F. R., Pen U.-L., Steinmetz M., Thomas P. A., Villumsen J. V., Wadsley J. W., Warren M. S., Xu G., Yepes G., 1999. ApJ, **525**, 554. *The Santa Barbara Cluster Comparison Project: A Comparison of Cosmological Hydrodynamics Solutions*.

Fryxell B., Olson K., Ricker P., Timmes F. X., Zingale M., Lamb D. Q., MacNeice P., Rosner R., Truran J. W., Tufo H., 2000. ApJS, **131**, 273. *FLASH: An Adaptive Mesh Hydrodynamics Code for Modeling Astrophysical Thermonuclear Flashes*.

Gallazzi A., Bell E. F., Wolf C., Gray M. E., Papovich C., Barden M., Peng C. Y., Meisenheimer K., Heymans C., van Kampen E., Gilmour R., Balogh M., McIntosh D. H., Bacon D., Barazza F. D., Böhm A., Caldwell J. A. R., Häußler B., Jahnke K., Jogee S., Lane K., Robaina A. R., Sanchez S. F., Taylor A., Wisotzki L., Zheng X., 2009. ApJ, **690**, 1883. *Obscured Star Formation in Intermediate-Density Environments: A Spitzer Study of the Abell 901/902 Supercluster*.

Gao L., White S. D. M., Jenkins A., Stoehr F., Springel V., 2004. MNRAS, **355**, 819. *The subhalo populations of ΛCDM dark haloes*.

Gebhardt K., Bender R., Bower G., Dressler A., Faber S. M., Filippenko A. V., Green R., Grillmair C., Ho L. C., Kormendy J., Lauer T. R., Magorrian J., Pinkney J., Richstone D., Tremaine S., 2000. ApJ, **539**, L13. *A Relationship between Nuclear Black Hole Mass and Galaxy Velocity Dispersion*.

Ghigna S., Moore B., Governato F., Lake G., Quinn T., Stadel J., 1998. MNRAS, **300**, 146. *Dark matter haloes within clusters*.

Ghigna S., Moore B., Governato F., Lake G., Quinn T., Stadel J., 2000. ApJ, **544**, 616. *Density Profiles and Substructure of Dark Matter Halos: Converging Results at Ultra-High Numerical Resolution*.

Gilbank D. G., Balogh M. L., Glazebrook K., Bower R. G., Baldry I. K., Davies G. T., Hau G. K. T., Li I. H., McCarthy P., 2010. MNRAS, **405**, 2419. *The Redshift One LDSS-3 Emission line Survey (ROLES): survey method and z ˜ 1 mass-dependent star formation rate density*.

Gill S. P. D., Knebe A., Gibson B. K., 2004. MNRAS, **351**, 399. *The evolution of substructure - I. A new identification method*.

Gingold R. A., Monaghan J. J., 1977. MNRAS, **181**, 375. *Smoothed particle hydrodynamics - Theory and application to non-spherical stars*.

Giocoli C., Tormen G., Sheth R. K., van den Bosch F. C., 2010. MNRAS, **404**, 502. *The substructure hierarchy in dark matter haloes*.

Grützbauch R., Conselice C. J., Varela J., Bundy K., Cooper M. C., Skibba R., Willmer C. N. A., 2011. MNRAS, **411**, 929. *How does galaxy environment matter? The relationship between galaxy environments, colour and stellar mass at $0.4 < z < 1$ in the Palomar/DEEP2 survey*.

Guo Q., White S., 2013. *ArXiv e-prints, astro-ph/1303.3586. The limits of subhalo abundance matching*.

Guo Q., White S., Li C., Boylan-Kolchin M., 2010. MNRAS, **404**, 1111. *How do galaxies populate dark matter haloes?*

Guo Q., White S., Boylan-Kolchin M., De Lucia G., Kauffmann G., Lemson G., Li C., Springel V., Weinmann S., 2011. MNRAS, **413**, 101. *From dwarf spheroidals to cD galaxies: simulating the galaxy population in a ΛCDM cosmology*.

Guth A. H., 1981. Phys. Rev. D, **23**, 347. *Inflationary universe: A possible solution to the horizon and flatness problems*.

Haardt F., Madau P., 2001. *Modelling the UV/X-ray cosmic background with CUBA*, In: *Clusters of Galaxies and the High Redshift Universe Observed in X-rays*, eds Neumann D. M., Tran J. T. V.

Haas M. R., Schaye J., Jeeson-Daniel A., 2012. MNRAS, **419**, 2133. *Disentangling galaxy environment and host halo mass*.

Hansen S. M., Sheldon E. S., Wechsler R. H., Koester B. P., 2009. ApJ, **699**, 1333. *The Galaxy Content of SDSS Clusters and Groups*.

Hayashi E., Navarro J. F., Taylor J. E., Stadel J., Quinn T., 2003. ApJ, **584**, 541. *The Structural Evolution of Substructure*.

Hénon M., 1964. *Annales d'Astrophysique*, **27**, 83. *L'évolution initiale d'un amas sphérique*.

Hernquist L., 1990. ApJ, **356**, 359. *An analytical model for spherical galaxies and bulges*.

Hernquist L., 1993. ApJS, **86**, 389. *N-body realizations of compound galaxies*.

Hobbs A., Nayakshin S., Power C., King A., 2011. MNRAS, **413**, 2633. *Feeding supermassive black holes through supersonic turbulence and ballistic accretion*.

Hobbs A., Power C., Nayakshin S., King A. R., 2012. MNRAS, **421**, 3443. *Modelling supermassive black hole growth: towards an improved sub-grid prescription*.

Hockney R. W., Eastwood J. W., 1981. *Computer Simulation Using Particles*.

Holmberg E., 1941. ApJ, **94**, 385. *On the Clustering Tendencies among the Nebulae. II. a Study of Encounters Between Laboratory Models of Stellar Systems by a New Integration Procedure.*

Hopkins P. F., Quataert E., 2010. MNRAS, **407**, 1529. *How do massive black holes get their gas?*

Hubble E., 1929. *Proceedings of the National Academy of Science*, **15**, 168. *A Relation between Distance and Radial Velocity among Extra-Galactic Nebulae*.

Jenkins A., Frenk C. S., White S. D. M., Colberg J. M., Cole S., Evrard A. E., Couchman H. M. P., Yoshida N., 2001. MNRAS, **321**, 372. *The mass function of dark matter haloes*.

Jernigan J. G., Porter D. H., 1989. ApJS, **71**, 871. *A tree code with logarithmic reduction of force terms, hierarchical regularization of all variables, and explicit accuracy controls*.

Jing Y. P., Mo H. J., Boerner G., 1998. ApJ, **494**, 1. *Spatial Correlation Function and Pairwise Velocity Dispersion of Galaxies: Cold Dark Matter Models versus the Las Campanas Survey*.

Johnson J. L., Whalen D. J., Li H., Holz D. E., 2012. *ArXiv e-prints, astro-ph/1211.0548. Supermassive Seeds for Supermassive Black Holes*.

Kauffmann G., White S. D. M., Heckman T. M., Ménard B., Brinchmann J., Charlot S., Tremonti C., Brinkmann J., 2004. MNRAS, **353**, 713. *The environmental dependence of the relations between stellar mass, structure, star formation and nuclear activity in galaxies*.

Kazantzidis S., Magorrian J., Moore B., 2004. ApJ, **601**, 37. *Generating Equilibrium Dark Matter Halos: Inadequacies of the Local Maxwellian Approximation*.

Kelly B. C., Merloni A., 2012. *Advances in Astronomy*, **2012**, 970858. *Mass Functions of Supermassive Black Holes across Cosmic Time*.

Kennicutt, Jr. R. C., 1998. ApJ, **498**, 541. *The Global Schmidt Law in Star-forming Galaxies*.

King A. R., 2010. MNRAS, **402**, 1516. *Black hole outflows*.

Klypin A. A., Shandarin S. F., 1983. MNRAS, **204**, 891. *Three-dimensional numerical model of the formation of large-scale structure in the Universe*.

Klypin A., Gottlöber S., Kravtsov A. V., Khokhlov A. M., 1999. ApJ, **516**, 530. *Galaxies in N-Body Simulations: Overcoming the Overmerging Problem*.

Knebe A., Knollmann S. R., Muldrew S. I., Pearce F. R., Aragon-Calvo M. A., Ascasibar Y., Behroozi P. S., Ceverino D., Colombi S., Diemand J., Dolag K., Falck B. L., Fasel P., Gardner J., Gottlöber S., Hsu C.-H., Iannuzzi F., Klypin A., Lukić Z., Maciejewski M., McBride C., Neyrinck M. C., Planelles S., Potter D., Quilis V., Rasera Y., Read J. I., Ricker P. M., Roy F., Springel V., Stadel J., Stinson G., Sutter P. M., Turchaninov V., Tweed D., Yepes G., Zemp M., 2011. MNRAS, **415**, 2293. *Haloes gone MAD: The Halo-Finder Comparison Project*.

Knebe A., Libeskind N. I., Pearce F., Behroozi P., Casado J., Dolag K., Dominguez-Tenreiro R., Elahi P., Lux H., Muldrew S. I., Onions J., 2013a. MNRAS, **428**, 2039. *Galaxies going MAD: the Galaxy-Finder Comparison Project*.

Knebe A., Pearce F. R., Lux H., Ascasibar Y., Behroozi P., Casado J., Corbett Moran C., Diemand J., Dolag K., Dominguez-Tenreiro R., Elahi P., Falck B., Gottloeber S., Han J., Klypin A., Lukic Z., Maciejewski M., McBride C. K., Merchan M. E., Muldrew S. I., Neyrinck M., Onions J., Planelles S., Potter D., Quilis V., Rasera Y., Ricker P. M., Roy F., Ruiz A. N., Sgro M. A., Springel V., Stadel J., Sutter P. M., Tweed D., Zemp M., 2013b. *ArXiv e-prints, astro-ph/1304.0585*. *Structure Finding in Cosmological Simulations: The State of Affairs*.

Knollmann S. R., Knebe A., 2009. ApJS, **182**, 608. *AHF: Amiga's Halo Finder*.

Kolmogorov A., 1933. *G. Inst. Ital. Attuari*, **4**, 83. *Sulla determinazione empirica di una legge di distribuzione*.

Kormendy J., Richstone D., 1995. ARA&A, **33**, 581. *Inward Bound—The Search For Supermassive Black Holes In Galactic Nuclei*.

Kovač K., Lilly S. J., Cucciati O., Porciani C., Iovino A., Zamorani G., Oesch P., Bolzonella M., Knobel C., Finoguenov A., Peng Y., Carollo C. M., Pozzetti L., Caputi K., Silverman J. D., Tasca L. A. M., Scodeggio M., Vergani D., Scoville N. Z., Capak P., Contini T., Kneib J.-P., Le Fèvre O., Mainieri V., Renzini A., Bardelli S., Bongiorno A., Coppa G., de la Torre S., de Ravel L., Franzetti P., Garilli B., Guzzo L., Kampczyk P., Lamareille F., Le Borgne J.-F., Le Brun V., Maier C., Mignoli M., Pello R., Perez Montero E., Ricciardelli E., Tanaka M., Tresse L., Zucca E., Abbas U., Bottini D., Cappi A., Cassata P., Cimatti A., Fumana M., Koekemoer A. M., Maccagni D., Marinoni C., McCracken H. J., Memeo P., Meneux B., Scaramella R., 2010. ApJ, **708**, 505. *The Density Field of the 10k zCOSMOS Galaxies*.

Kravtsov A. V., Berlind A. A., Wechsler R. H., Klypin A. A., Gottlöber S., Allgood B., Primack J. R., 2004. ApJ, **609**, 35. *The Dark Side of the Halo Occupation Distribution*.

Lacey C., Cole S., 1993. MNRAS, **262**, 627. *Merger rates in hierarchical models of galaxy formation*.

Larson R. B., 1974. MNRAS, **169**, 229. *Effects of supernovae on the early evolution of galaxies*.

Lewis I., Balogh M., De Propris R., Couch W., Bower R., Offer A., Bland-Hawthorn J., Baldry I. K., Baugh C., Bridges T., Cannon R., Cole S., Colless M., Collins C., Cross N., Dalton G., Driver S. P., Efstathiou G., Ellis R. S., Frenk C. S., Glazebrook K., Hawkins E., Jackson C., Lahav O., Lumsden S., Maddox S., Madgwick D., Norberg P., Peacock J. A., Percival W., Peterson B. A., Sutherland W., Taylor K., 2002. MNRAS, **334**, 673. *The 2dF Galaxy Redshift Survey: the environmental dependence of galaxy star formation rates near clusters*.

Li C., Kauffmann G., Jing Y. P., White S. D. M., Börner G., Cheng F. Z., 2006. MNRAS, **368**, 21. *The dependence of clustering on galaxy properties*.

Li I. H., Glazebrook K., Gilbank D., Balogh M., Bower R., Baldry I., Davies G., Hau G., McCarthy P., 2011. MNRAS, **411**, 1869. *Dependence of star formation activity on stellar mass and environment from the Redshift One LDSS-3 Emission line Survey*.

Libeskind N. I., Yepes G., Knebe A., Gottlöber S., Hoffman Y., Knollmann S. R., 2010. MNRAS, **401**, 1889. *Constrained simulations of the Local Group: on the radial distribution of substructures*.

Łokas E. L., Mamon G. A., 2001. MNRAS, **321**, 155. *Properties of spherical galaxies and clusters with an NFW density profile*.

Lovell M. R., Eke V., Frenk C. S., Gao L., Jenkins A., Theuns T., Wang J., White S. D. M., Boyarsky A., Ruchayskiy O., 2012. MNRAS, **420**, 2318. *The haloes of bright satellite galaxies in a warm dark matter universe*.

Macciò A. V., Dutton A. A., van den Bosch F. C., 2008. MNRAS, **391**, 1940. *Concentration, spin and shape of dark matter haloes as a function of the cosmological model: WMAP1, WMAP3 and WMAP5 results*.

Macciò A. V., Dutton A. A., van den Bosch F. C., Moore B., Potter D., Stadel J., 2007. MNRAS, **378**, 55. *Concentration, spin and shape of dark matter haloes: scatter and the dependence on mass and environment*.

Maciejewski M., Colombi S., Springel V., Alard C., Bouchet F. R., 2009. MNRAS, **396**, 1329. *Phase-space structures - II. Hierarchical Structure Finder*.

Madau P., Rees M. J., 2001. ApJ, **551**, L27. *Massive Black Holes as Population III Remnants*.

Magorrian J., Tremaine S., Richstone D., Bender R., Bower G., Dressler A., Faber S. M., Gebhardt K., Green R., Grillmair C., Kormendy J., Lauer T., 1998. *AJ*, **115**, 2285. *The Demography of Massive Dark Objects in Galaxy Centers*.

Marinoni C., Davis M., Newman J. A., Coil A. L., 2002. ApJ, **580**, 122. *Three-dimensional Identification and Reconstruction of Galaxy Systems within Flux-limited Redshift Surveys*.

Marleau F. R., Simard L., Clancy D., Bianconi M., 2012. *ArXiv e-prints, astro-ph/1212.0980*. *The Ubiquity of Supermassive Black Holes in the Hubble Sequence*.

Martínez H. J., Muriel H., 2006. MNRAS, **370**, 1003. *Groups of galaxies: relationship between environment and galaxy properties*.

McLure R. J., Dunlop J. S., 2002. MNRAS, **331**, 795. *On the black hole-bulge mass relation in active and inactive galaxies*.

Mo H., van den Bosch F. C., White S., 2010. *Galaxy Formation and Evolution*.

Monaghan J. J., Lattanzio J. C., 1985. A&A, **149**, 135. *A refined particle method for astrophysical problems*.

Mortlock D. J., Warren S. J., Venemans B. P., Patel M., Hewett P. C., McMahon R. G., Simpson C., Theuns T., Gonzáles-Solares E. A., Adamson A., Dye S., Hambly N. C., Hirst P., Irwin M. J., Kuiper E., Lawrence A., Röttgering H. J. A., 2011. Nature, **474**, 616. *A luminous quasar at a redshift of z = 7.085*.

Muldrew S. I., Croton D. J., Skibba R. A., Pearce F. R., Ann H. B., Baldry I. K., Brough S., Choi Y.-Y., Conselice C. J., Cowan N. B., Gallazzi A., Gray M. E., Grützbauch R., Li I.-H., Park C., Pilipenko S. V., Podgorzec B. J., Robotham A. S. G., Wilman D. J., Yang X., Zhang Y., Zibetti S., 2012. MNRAS, **419**, 2670. *Measures of galaxy environment - I. What is 'environment'?*

Muldrew S. I., Pearce F. R., Power C., 2011. MNRAS, **410**, 2617. *The accuracy of subhalo detection*.

Navarro J. F., Frenk C. S., White S. D. M., 1996. ApJ, **462**, 563. *The Structure of Cold Dark Matter Halos*.

Navarro J. F., Frenk C. S., White S. D. M., 1997. ApJ, **490**, 493. *A Universal Density Profile from Hierarchical Clustering*.

Nayakshin S., Cha S.-H., Hobbs A., 2009. MNRAS, **397**, 1314. *Dynamic Monte Carlo radiation transfer in SPH: radiation pressure force implementation*.

Neto A. F., Gao L., Bett P., Cole S., Navarro J. F., Frenk C. S., White S. D. M., Springel V., Jenkins A., 2007. MNRAS, **381**, 1450. *The statistics of Λ CDM halo concentrations*.

Newton R. D. A., Kay S. T., 2013. *ArXiv e-prints, astro-ph/1304.0443. A study of AGN and supernova feedback in simulations of isolated and merging disc galaxies*.

Neyrinck M. C., Gnedin N. Y., Hamilton A. J. S., 2005. MNRAS, **356**, 1222. *VOBOZ: an almost-parameter-free halo-finding algorithm*.

Norberg P., Baugh C. M., Hawkins E., Maddox S., Madgwick D., Lahav O., Cole S., Frenk C. S., Baldry I., Bland-Hawthorn J., Bridges T., Cannon R., Colless M., Collins C., Couch W., Dalton G., De Propris R., Driver S. P., Efstathiou G., Ellis R. S., Glazebrook K., Jackson C., Lewis I., Lumsden S., Peacock J. A., Peterson B. A., Sutherland W., Taylor K., 2002. MNRAS, **332**, 827. *The 2dF Galaxy Redshift Survey: the dependence of galaxy clustering on luminosity and spectral type*.

Oemler, Jr. A., 1974. ApJ, **194**, 1. *The Systematic Properties of Clusters of Galaxies. Photometry of 15 Clusters*.

O'Mill A. L., Padilla N., García Lambas D., 2008. MNRAS, **389**, 1763. *Evolution of environment-dependent galaxy properties in the Sloan Digital Sky Survey*.

Onions J., Knebe A., Pearce F. R., Muldrew S. I., Lux H., Knollmann S. R., Ascasibar Y., Behroozi P., Elahi P., Han J., Maciejewski M., Merchán M. E., Neyrinck M., Ruiz A. N., Sgró M. A., Springel V., Tweed D., 2012. MNRAS, **423**, 1200. *Subhaloes going Notts: the subhalo-finder comparison project*.

Onions J., Ascasibar Y., Behroozi P., Casado J., Elahi P., Han J., Knebe A., Lux H., Merchán M. E., Muldrew S. I., Neyrinck M., Old L., Pearce F. R., Potter D., Ruiz A. N., Sgró M. A., Tweed D., Yue T., 2013. MNRAS, **429**, 2739. *Subhaloes gone Notts: spin across subhaloes and finders*.

O'Shea B. W., Bryan G., Bordner J., Norman M. L., Abel T., Harkness R., Kritsuk A., 2004. *ArXiv e-prints, astro-ph/0403044. Introducing Enzo, an AMR Cosmology Application*.

Ostriker J. P., Peebles P. J. E., Yahil A., 1974. ApJ, **193**, L1. *The size and mass of galaxies, and the mass of the universe*.

Park C., Choi Y.-Y., Vogeley M. S., Gott, III J. R., Blanton M. R., SDSS Collaboration, 2007. ApJ, **658**, 898. *Environmental Dependence of Properties of Galaxies in the Sloan Digital Sky Survey*.

Penzias A. A., Wilson R. W., 1965. ApJ, **142**, 419. *A Measurement of Excess Antenna Temperature at 4080 Mc/s.*

Perlmutter S., Aldering G., Goldhaber G., Knop R. A., Nugent P., Castro P. G., Deustua S., Fabbro S., Goobar A., Groom D. E., Hook I. M., Kim A. G., Kim M. Y., Lee J. C., Nunes N. J., Pain R., Pennypacker C. R., Quimby R., Lidman C., Ellis R. S., Irwin M., McMahon R. G., Ruiz-Lapuente P., Walton N., Schaefer B., Boyle B. J., Filippenko A. V., Matheson T., Fruchter A. S., Panagia N., Newberg H. J. M., Couch W. J., Supernova Cosmology Project, 1999. ApJ, **517**, 565. *Measurements of Omega and Lambda from 42 High-Redshift Supernovae*.

Planck Collaboration, 2013. *ArXiv e-prints, astro-ph/1303.5062. Planck 2013 results. I. Overview of products and scientific results*.

Planelles S., Quilis V., 2010. A&A, **519**, A94. *ASOHF: a new adaptive spherical overdensity halo finder*.

Plummer H. C., 1911. MNRAS, **71**, 460. *On the problem of distribution in globular star clusters*.

Poggianti B. M., Desai V., Finn R., Bamford S., De Lucia G., Varela J., Aragón-Salamanca A., Halliday C., Noll S., Saglia R., Zaritsky D., Best P., Clowe D., Milvang-Jensen B., Jablonka P., Pelló R., Rudnick G., Simard L., von der Linden A., White S., 2008. ApJ, **684**, 888. *The Relation between Star Formation, Morphology, and Local Density in High-Redshift Clusters and Groups*.

Poggianti B. M., De Lucia G., Varela J., Aragon-Salamanca A., Finn R., Desai V., von der Linden A., White S. D. M., 2010. MNRAS, **405**, 995. *The evolution of the density of galaxy clusters and groups: denser environments at higher redshifts*.

Power C., Navarro J. F., Jenkins A., Frenk C. S., White S. D. M., Springel V., Stadel J., Quinn T., 2003. MNRAS, **338**, 14. *The inner structure of ΛCDM haloes - I. A numerical convergence study*.

Power C., Nayakshin S., King A., 2011. MNRAS, **412**, 269. *The accretion disc particle method for simulations of black hole feeding and feedback **(PNK11)***.

Quadri R. F., Williams R. J., Lee K.-S., Franx M., van Dokkum P., Brammer G. B., 2008. ApJ, **685**, L1. *A Confirmation of the Strong Clustering of Distant Red Galaxies at $2 < z < 3$.*

Read J. I., Wilkinson M. I., Evans N. W., Gilmore G., Kleyna J. T., 2006. MNRAS, **367**, 387. *The importance of tides for the Local Group dwarf spheroidals.*

Reed D. S., Smith R. E., Potter D., Schneider A., Stadel J., Moore B., 2013. MNRAS. *Towards an accurate mass function for precision cosmology.*

Riess A. G., Filippenko A. V., Challis P., Clocchiatti A., Diercks A., Garnavich P. M., Gilliland R. L., Hogan C. J., Jha S., Kirshner R. P., Leibundgut B., Phillips M. M., Reiss D., Schmidt B. P., Schommer R. A., Smith R. C., Spyromilio J., Stubbs C., Suntzeff N. B., Tonry J., 1998. AJ, **116**, 1009. *Observational Evidence from Supernovae for an Accelerating Universe and a Cosmological Constant.*

Rubin V. C., Ford, Jr. W. K., 1970. ApJ, **159**, 379. *Rotation of the Andromeda Nebula from a Spectroscopic Survey of Emission Regions.*

Rudnick G., von der Linden A., Pelló R., Aragón-Salamanca A., Marchesini D., Clowe D., De Lucia G., Halliday C., Jablonka P., Milvang-Jensen B., Poggianti B., Saglia R., Simard L., White S., Zaritsky D., 2009. ApJ, **700**, 1559. *The Rest-frame Optical Luminosity Function of Cluster Galaxies at $z < 0.8$ and the Assembly of the Cluster Red Sequence.*

Scannapieco C., Wadepuhl M., Parry O. H., Navarro J. F., Jenkins A., Springel V., Teyssier R., Carlson E., Couchman H. M. P., Crain R. A., Dalla Vecchia C., Frenk C. S., Kobayashi C., Monaco P., Murante G., Okamoto T., Quinn T., Schaye J., Stinson G. S., Theuns T., Wadsley J., White S. D. M., Woods R., 2012. MNRAS, **423**, 1726. *The Aquila comparison project: the effects of feedback and numerical methods on simulations of galaxy formation.*

Schaye J., Dalla Vecchia C., 2008. MNRAS, **383**, 1210. *On the relation between the Schmidt and Kennicutt-Schmidt star formation laws and its implications for numerical simulations.*

Schaye J., Dalla Vecchia C., Booth C. M., Wiersma R. P. C., Theuns T., Haas M. R., Bertone S., Duffy A. R., McCarthy I. G., van de Voort F., 2010. MNRAS, **402**, 1536. *The physics driving the cosmic star formation history.*

Schmidt B. P., Suntzeff N. B., Phillips M. M., Schommer R. A., Clocchiatti A., Kirshner R. P., Garnavich P., Challis P., Leibundgut B., Spyromilio J., Riess A. G., Filippenko A. V., Hamuy M., Smith R. C., Hogan C., Stubbs C., Diercks A., Reiss D., Gilliland R., Tonry J., Maza J., Dressler A., Walsh J., Ciardullo R., 1998. ApJ, **507**, 46. *The High-Z Supernova Search: Measuring Cosmic Deceleration and Global Curvature of the Universe Using Type IA Supernovae.*

Scodeggio M., Vergani D., Cucciati O., Iovino A., Franzetti P., Garilli B., Lamareille F., Bolzonella M., Pozzetti L., Abbas U., Marinoni C., Contini T., Bottini D., Le Brun V., Le Fèvre O., Maccagni D., Scaramella R., Tresse L., Vettolani G., Zanichelli A., Adami C., Arnouts S., Bardelli S., Cappi A., Charlot S., Ciliegi P., Foucaud S.,

Gavignaud I., Guzzo L., Ilbert O., McCracken H. J., Marano B., Mazure A., Meneux B., Merighi R., Paltani S., Pellò R., Pollo A., Radovich M., Zamorani G., Zucca E., Bondi M., Bongiorno A., Brinchmann J., de La Torre S., de Ravel L., Gregorini L., Memeo P., Perez-Montero E., Mellier Y., Temporin S., Walcher C. J., 2009. A&A, **501**, 21. *The Vimos VLT Deep Survey. Stellar mass segregation and large-scale galaxy environment in the redshift range 0.2 $< z <$ 1.4.*

Shakura N. I., Sunyaev R. A., 1973. A&A, **24**, 337. *Black holes in binary systems. Observational appearance.*

Shankar F., Weinberg D. H., Miralda-Escudé J., 2009. ApJ, **690**, 20. *Self-Consistent Models of the AGN and Black Hole Populations: Duty Cycles, Accretion Rates, and the Mean Radiative Efficiency*.

Sheth R. K., Jimenez R., Panter B., Heavens A. F., 2006. ApJ, **650**, L25. *Environment and the Cosmic Evolution of Star Formation*.

Sijacki D., Springel V., Di Matteo T., Hernquist L., 2007. MNRAS, **380**, 877. *A unified model for AGN feedback in cosmological simulations of structure formation*.

Skibba R. A., Sheth R. K., 2009. MNRAS, **392**, 1080. *A halo model of galaxy colours and clustering in the Sloan Digital Sky Survey **(SS09)***.

Skibba R., Sheth R. K., Connolly A. J., Scranton R., 2006. MNRAS, **369**, 68. *The luminosity-weighted or 'marked' correlation function **(S06)***.

Skibba R. A., Bamford S. P., Nichol R. C., Lintott C. J., Andreescu D., Edmondson E. M., Murray P., Raddick M. J., Schawinski K., Slosar A., Szalay A. S., Thomas D., Vandenberg J., 2009. MNRAS, **399**, 966. *Galaxy Zoo: disentangling the environmental dependence of morphology and colour*.

Skibba R. A., van den Bosch F. C., Yang X., More S., Mo H., Fontanot F., 2011. MNRAS, **410**, 417. *Are brightest halo galaxies central galaxies?*

Skibba R. A., Sheth R. K., Croton D. J., Muldrew S. I., Abbas U., Pearce F. R., Shattow G. M., 2013. MNRAS, **429**, 458. *Measures of galaxy environment - II. Rank-ordered mark correlations*.

Skibba R. A., 2009. MNRAS, **392**, 1467. *Central and satellite colours in galaxy groups: a comparison of the halo model and SDSS group catalogues*.

Smirnov N. V., 1948. *Annals of Mathematical Statistics*, **19**, 279. *Tables for estimating the goodness of fit of empirical distributions*.

Spergel D. N., Verde L., Peiris H. V., Komatsu E., Nolta M. R., Bennett C. L., Halpern M., Hinshaw G., Jarosik N., Kogut A., Limon M., Meyer S. S., Page L., Tucker G. S., Weiland J. L., Wollack E., Wright E. L., 2003. ApJS, **148**, 175. *First-Year Wilkinson Microwave Anisotropy Probe (WMAP) Observations: Determination of Cosmological Parameters*.

Spergel D. N., Bean R., Doré O., Nolta M. R., Bennett C. L., Dunkley J., Hinshaw G., Jarosik N., Komatsu E., Page L., Peiris H. V., Verde L., Halpern M., Hill R. S., Kogut A., Limon M., Meyer S. S., Odegard N., Tucker G. S., Weiland J. L., Wollack E., Wright E. L., 2007. ApJS, **170**, 377. *Three-Year Wilkinson Microwave Anisotropy Probe (WMAP) Observations: Implications for Cosmology*.

Springel V., Hernquist L., 2003. MNRAS, **339**, 289. *Cosmological smoothed particle hydrodynamics simulations: a hybrid multiphase model for star formation*.

Springel V., Di Matteo T., Hernquist L., 2005. MNRAS, **361**, 776. *Modelling feedback from stars and black holes in galaxy mergers*.

Springel V., White S. D. M., Tormen G., Kauffmann G., 2001. MNRAS, **328**, 726. *Populating a cluster of galaxies - I. Results at z=0*.

Springel V., White S. D. M., Jenkins A., Frenk C. S., Yoshida N., Gao L., Navarro J., Thacker R., Croton D., Helly J., Peacock J. A., Cole S., Thomas P., Couchman H., Evrard A., Colberg J., Pearce F., 2005. Nature, **435**, 629. *Simulations of the formation, evolution and clustering of galaxies and quasars*.

Springel V., Wang J., Vogelsberger M., Ludlow A., Jenkins A., Helmi A., Navarro J. F., Frenk C. S., White S. D. M., 2008. MNRAS, **391**, 1685. *The Aquarius Project: the subhaloes of galactic haloes*.

Springel V., 2005. MNRAS, **364**, 1105. *The cosmological simulation code GADGET-2*.

Springel V., 2010a. MNRAS, **401**, 791. *E pur si muove: Galilean-invariant cosmological hydrodynamical simulations on a moving mesh*.

Springel V., 2010b. ARA&A, **48**, 391. *Smoothed Particle Hydrodynamics in Astrophysics*.

Stadel J., Potter D., Moore B., Diemand J., Madau P., Zemp M., Kuhlen M., Quilis V., 2009. MNRAS, **398**, L21. *Quantifying the heart of darkness with GHALO - a multibillion particle simulation of a galactic halo*.

Tasca L. A. M., Kneib J.-P., Iovino A., Le Fèvre O., Kovač K., Bolzonella M., Lilly S. J., Abraham R. G., Cassata P., Cucciati O., Guzzo L., Tresse L., Zamorani G., Capak P., Garilli B., Scodeggio M., Sheth K., Zucca E., Carollo C. M., Contini T., Mainieri V., Renzini A., Bardelli S., Bongiorno A., Caputi K., Coppa G., de La Torre S., de Ravel L., Franzetti P., Kampczyk P., Knobel C., Koekemoer A. M., Lamareille F., Le Borgne J.-F., Le Brun V., Maier C., Mignoli M., Pello R., Peng Y., Perez Montero E., Ricciardelli E., Silverman J. D., Vergani D., Tanaka M., Abbas U., Bottini D., Cappi A., Cimatti A., Ilbert O., Leauthaud A., Maccagni D., Marinoni C., McCracken H. J., Memeo P., Meneux B., Oesch P., Porciani C., Pozzetti L., Scaramella R., Scarlata C., 2009. A&A, **503**, 379. *The zCOSMOS redshift survey: the role of environment and stellar mass in shaping the rise of the morphology-density relation from z ˜ 1*.

Teyssier R., 2002. A&A, **385**, 337. *Cosmological hydrodynamics with adaptive mesh refinement. A new high resolution code called RAMSES*.

Thompson T. A., Quataert E., Murray N., 2005. ApJ, **630**, 167. *Radiation Pressure-supported Starburst Disks and Active Galactic Nucleus Fueling*.

Tinker J. L., Conroy C., Norberg P., Patiri S. G., Weinberg D. H., Warren M. S., 2008. ApJ, **686**, 53. *Void Statistics in Large Galaxy Redshift Surveys: Does Halo Occupation of Field Galaxies Depend on Environment?*

Tormen G., Diaferio A., Syer D., 1998. MNRAS, **299**, 728. *Survival of substructure within dark matter haloes*.

Tormen G., Moscardini L., Yoshida N., 2004. MNRAS, **350**, 1397. *Properties of cluster satellites in hydrodynamical simulations*.

Tremaine S., Gebhardt K., Bender R., Bower G., Dressler A., Faber S. M., Filippenko A. V., Green R., Grillmair C., Ho L. C., Kormendy J., Lauer T. R., Magorrian J., Pinkney J., Richstone D., 2002. ApJ, **574**, 740. *The Slope of the Black Hole Mass versus Velocity Dispersion Correlation*.

Vale A., Ostriker J. P., 2004. MNRAS, **353**, 189. *Linking halo mass to galaxy luminosity*.

van den Bosch F. C., Aquino D., Yang X., Mo H. J., Pasquali A., McIntosh D. H., Weinmann S. M., Kang X., 2008a. MNRAS, **387**, 79. *The importance of satellite quenching for the build-up of the red sequence of present-day galaxies*.

van den Bosch F. C., Pasquali A., Yang X., Mo H. J., Weinmann S., McIntosh D. H., Aquino D., 2008b. *ArXiv e-prints, astro-ph/0805.0002. Satellite Ecology: The Dearth of Environment Dependence*.

van den Bosch R. C. E., Gebhardt K., Gültekin K., van de Ven G., van der Wel A., Walsh J. L., 2012. Nature, **491**, 729. *An over-massive black hole in the compact lenticular galaxy NGC1277*.

Vogelsberger M., Genel S., Sijacki D., Torrey P., Springel V., Hernquist L., 2013. *ArXiv e-prints, astro-ph/1305.2913. A physical model for cosmological simulations of galaxy formation*.

Vulcani B., Poggianti B. M., Aragón-Salamanca A., Fasano G., Rudnick G., Valentinuzzi T., Dressler A., Bettoni D., Cava A., D'Onofrio M., Fritz J., Moretti A., Omizzolo A., Varela J., 2011. MNRAS, **412**, 246. *Galaxy stellar mass functions of different morphological types in clusters, and their evolution between z= 0.8 and 0*.

Wadsley J. W., Stadel J., Quinn T., 2004. *New Astronomy*, **9**, 137. *Gasoline: a flexible, parallel implementation of TreeSPH*.

Weinmann S. M., van den Bosch F. C., Yang X., Mo H. J., 2006. MNRAS, **366**, 2. *Properties of galaxy groups in the Sloan Digital Sky Survey - I. The dependence of colour, star formation and morphology on halo mass*.

White S. D. M., Frenk C. S., 1991. ApJ, **379**, 52. *Galaxy formation through hierarchical clustering*.

White S. D. M., Rees M. J., 1978. MNRAS, **183**, 341. *Core condensation in heavy halos - A two-stage theory for galaxy formation and clustering*.

White S. D. M., Frenk C. S., Davis M., 1983. ApJ, **274**, L1. *Clustering in a neutrino-dominated universe*.

Wiersma R. P. C., Schaye J., Theuns T., Dalla Vecchia C., Tornatore L., 2009. MNRAS, **399**, 574. *Chemical enrichment in cosmological, smoothed particle hydrodynamics simulations*.

Wiersma R. P. C., Schaye J., Smith B. D., 2009. MNRAS, **393**, 99. *The effect of photoionization on the cooling rates of enriched, astrophysical plasmas*.

Wilman D. J., Zibetti S., Budavári T., 2010. MNRAS, **406**, 1701. *A multiscale approach to environment and its influence on the colour distribution of galaxies*.

Wolf C., Aragón-Salamanca A., Balogh M., Barden M., Bell E. F., Gray M. E., Peng C. Y., Bacon D., Barazza F. D., Böhm A., Caldwell J. A. R., Gallazzi A., Häußler B., Heymans C., Jahnke K., Jogee S., van Kampen E., Lane K., McIntosh D. H., Meisenheimer K., Papovich C., Sánchez S. F., Taylor A., Wisotzki L., Zheng X., 2009. MNRAS, **393**, 1302. *The STAGES view of red spirals and dusty red galaxies: mass-dependent quenching of star formation in cluster infall*.

Wurster J., Thacker R. J., 2013. MNRAS, **431**, 539. *Accretion disc particle accretion in major merger simulations*.

Yang X., Mo H. J., van den Bosch F. C., Weinmann S. M., Li C., Jing Y. P., 2005. MNRAS, **362**, 711. *The cross-correlation between galaxies and groups: probing the galaxy distribution in and around dark matter haloes*.

Yang X., Mo H. J., van den Bosch F. C., Pasquali A., Li C., Barden M., 2007. ApJ, **671**, 153. *Galaxy Groups in the SDSS DR4. I. The Catalog and Basic Properties*.

Yang X., Mo H. J., van den Bosch F. C., 2003. MNRAS, **339**, 1057. *Constraining galaxy formation and cosmology with the conditional luminosity function of galaxies*.

Yang X., Mo H. J., van den Bosch F. C., 2009. ApJ, **695**, 900. *Galaxy Groups in the SDSS DR4. III. The Luminosity and Stellar Mass Functions*.

York D. G., Adelman J., Anderson, Jr. J. E., Anderson S. F., Annis J., Bahcall N. A., Bakken J. A., Barkhouser R., Bastian S., Berman E., Boroski W. N., Bracker S., Briegel C., Briggs J. W., Brinkmann J., Brunner R., Burles S., Carey L., Carr M. A., Castander F. J., Chen B., Colestock P. L., Connolly A. J., Crocker J. H., Csabai I., Czarapata P. C., Davis J. E., Doi M., Dombeck T., Eisenstein D., Ellman N., Elms B. R., Evans M. L., Fan X., Federwitz G. R., Fiscelli L., Friedman S., Frieman J. A., Fukugita M., Gillespie B., Gunn J. E., Gurbani V. K., de Haas E., Haldeman M., Harris F. H., Hayes J., Heckman T. M., Hennessy G. S., Hindsley R. B., Holm S., Holmgren D. J., Huang C.-h., Hull C., Husby D., Ichikawa S.-I., Ichikawa T., Ivezić Ž., Kent S., Kim R. S. J., Kinney E., Klaene M., Kleinman A. N., Kleinman S., Knapp G. R., Korienek J., Kron R. G., Kunszt P. Z., Lamb D. Q., Lee B., Leger R. F., Limmongkol S., Lindenmeyer C., Long D. C., Loomis C., Loveday J., Lucinio R., Lupton R. H., MacKinnon B., Mannery E. J., Mantsch P. M., Margon B., McGehee

P., McKay T. A., Meiksin A., Merelli A., Monet D. G., Munn J. A., Narayanan V. K., Nash T., Neilsen E., Neswold R., Newberg H. J., Nichol R. C., Nicinski T., Nonino M., Okada N., Okamura S., Ostriker J. P., Owen R., Pauls A. G., Peoples J., Peterson R. L., Petravick D., Pier J. R., Pope A., Pordes R., Prosapio A., Rechenmacher R., Quinn T. R., Richards G. T., Richmond M. W., Rivetta C. H., Rockosi C. M., Ruthmansdorfer K., Sandford D., Schlegel D. J., Schneider D. P., Sekiguchi M., Sergey G., Shimasaku K., Siegmund W. A., Smee S., Smith J. A., Snedden S., Stone R., Stoughton C., Strauss M. A., Stubbs C., SubbaRao M., Szalay A. S., Szapudi I., Szokoly G. P., Thakar A. R., Tremonti C., Tucker D. L., Uomoto A., Vanden Berk D., Vogeley M. S., Waddell P., Wang S.-i., Watanabe M., Weinberg D. H., Yanny B., Yasuda N., SDSS Collaboration, 2000. AJ, **120**, 1579. *The Sloan Digital Sky Survey: Technical Summary*.

Zehavi I., Zheng Z., Weinberg D. H., Frieman J. A., Berlind A. A., Blanton M. R., Scoccimarro R., Sheth R. K., Strauss M. A., Kayo I., Suto Y., Fukugita M., Nakamura O., Bahcall N. A., Brinkmann J., Gunn J. E., Hennessy G. S., Ivezić Ž., Knapp G. R., Loveday J., Meiksin A., Schlegel D. J., Schneider D. P., Szapudi I., Tegmark M., Vogeley M. S., York D. G., SDSS Collaboration, 2005. ApJ, **630**, 1. *The Luminosity and Color Dependence of the Galaxy Correlation Function.*

Zehavi I., Zheng Z., Weinberg D. H., Blanton M. R., Bahcall N. A., Berlind A. A., Brinkmann J., Frieman J. A., Gunn J. E., Lupton R. H., Nichol R. C., Percival W. J., Schneider D. P., Skibba R. A., Strauss M. A., Tegmark M., York D. G., 2011. ApJ, **736**, 59. *Galaxy Clustering in the Completed SDSS Redshift Survey: The Dependence on Color and Luminosity*.

Zheng Z., Coil A. L., Zehavi I., 2007. ApJ, **667**, 760. *Galaxy Evolution from Halo Occupation Distribution Modeling of DEEP2 and SDSS Galaxy Clustering*.

Zwicky F., 1933. *Helvetica Physica Acta*, **6**, 110. *Die Rotverschiebung von extragalaktischen Nebeln*.

Zwicky F., 1937. ApJ, **86**, 217. *On the Masses of Nebulae and of Clusters of Nebulae*.